This is to certify that the

dissertation entitled

A Semi-Active Helmholtz Resonator

presented by

Charles Birdsong

has been accepted towards fulfillment
of the requirements for

Ph.D. degree in Mechanical Engineering

Clark Radcliffe
Major professor

Date November 22, 1999

DATE DUE	DATE DUE	DATE DUE
SEP 2 1 2002		

A Semi-Active Helmholtz Resonator

By

Charles Birdsong

A DISSERTATION

Submitted to
Michigan State University
in partial fulfillment of the requirements
for the degree of

DOCTOR OF PHILOSOPHY

Mechanical Engineering

1999

ABSTRACT

A Semi-Active Helmholtz Resonator

By

Charles Birdsong

Helmholtz resonators are commonly used to reduce the sound transmitted through acoustic systems such as industrial processes, vehicle exhaust, industrial ducting systems and more. They function by reflecting sound in a narrow, tuned frequency band back to the source, where the tuned frequency is a function of the dimensions of the resonator cavity. If the frequency of the unwanted noise changes from the tuned value, the noise reduction is diminished. Past efforts at active tuning of Helmholtz resonators resulted in limited tuning capability and significant mechanical complexity. This work considers a system that actively modifies the acoustic response of a Helmholtz resonator continuously, on-line, allowing optimum performance over a range of operating conditions. The system consists of a static Helmholtz resonator designed to enforce a nominal resonance and a feedback control system that provides a variable acoustic impedance. The combination of the nominal impedance of the resonator and the differential impedance of the controller results in a semi-active controlled, variable frequency Helmholtz resonator.

A model is presented and analysis, numerical simulations, and experimental results are used to demonstrate the effectiveness of the device. An analysis of the power flow in an acoustic duct with the device is presented to answer the question, "Where does the sound go?" A comparison of actuator implementation techniques is presented that concludes that the actuator dynamics must be included in the controller design, and that different configurations produce results with competing advantages and disadvantages. Finally, a closed-loop adaptive control strategy is presented that uses a gain-scheduled controller to tune the device on-line and track a disturbance signal with slow time-varying frequency.

This work is dedicated to my beautiful wife, Bernadette, and son, Indigo

A special thanks to all my friends and family who supported me during this time:

Lenny Monterrosa
Mark Minor
Brooks Byam
Joga Setiawan
Joe Derose
Gary Gosciak
Tuhin Das
Brennan Sicks
Nancy Albright
Carol Bishop
Aida Rodriguez
Roy Bailiff
Dave and Sara Hunter
Martha Quant
Lisa Saltman
Augie Hernandez
Pete Jewett
Mike Jewett
The MSU Karate Club
Sally Star and the whole Subway crew

ACKNOWLEDGMENTS

I would like to thank

Lakhi Goenka of Visteon Automotive

and the members of the

Manufacturing Research Consortium at Michigan State University

for funding this work

TABLE OF CONTENTS

Chapter 5

Chapter 6

LIST OF TABLES

LIST OF FIGURES

LIST OF ABBREVIATIONS

Uppercase

A_D	duct cross sectional area (m^2)
C_a	acoustic compliance (m^5/N)
D	disturbance signal
G_c	controller transfer function
H_{bs}	velocity sensor transfer function for secondary coil
H_p	velocity sensor transfer function for primary coil
I_a	acoustic inertia (ms^2/m^5)
I_c	coil inductance (H)
Im	imaginary part
K_{amp}	amplifier gain
K_I	integral gain
K_P	proportional gain
L	length of duct (m)
M_c	mutual inductance (H)
P_1	pressure on opening to resonator neck (N/m^2)
P_2	pressure in resonator cavity (N/m^2)
$\mathbf{P}_A$	absorbed power
$\mathbf{P}_I$	incident power
$\mathbf{P}_R$	reflected power
$\mathbf{P}_T$	transmitted power
Q_1	volume velocity in resonator neck (m^3/s)
Q_2	volume velocity in resonator cavity (m^3/s)
Q_A	volume velocity in resonator neck (m^3/s)
Q_I	volume velocity in duct upstream of resonator (m^3/s)
Q_T	volume velocity in duct downstream of resonator (m^3/s)
R	acoustic radiation loss (Ns/m^5)
R_c	speaker coil resistance (ohms)
Re	real part
R_m	current sensing resistor resistance ohms
S	area (m^2)
S_d	speaker face area (m^2)
SHR	semi-active Helmholtz resonator
S_{mic}	microphone sensitivity (volts/Pa)
TL	transmission loss
V	volume (m^3)
Z_1	acoustic impedance of resonator (Ns/m^5)
Z_2	acoustic impedance of cavity surface (Ns/m^5)
Z_A	acoustic impedance in resonator neck (Ns/m^5)

Z_I ....acoustic impedance of duct cross section upstream of resonator(Ns/m^5)
Z_T ....acoustic impedance of duct cross section downstream of resonator (Ns/m^5)

Lowercase
bl..................electromechanical coupling factor (N/amp)
c_o..................speed of sound in air (m/s)
e_{bs} ....secondary coil voltage (volts)
e_p ....primary coil voltage (volts)
$\hat{f}$ ....incident pressure wave amplitude (Pa)
i_{bs} ....secondary coil current (amps)
i_p ....primary coil current (amps)
k....................wave number (rad/m)
l ....length (m)
q_1 ....volume displacement in resonator neck (m)
q_2 ....volume displacement of actuator
s ....Laplace variable
v_a ....speaker face velocity (m/s)
x....................spatial variable (m)
x_o ....scalar that controls amplitude of Z_2

Greek
Δf ....half power band--width
λ ....electromagnetic flux
ρ_o ....density of air (Kg/m^3)
ω_c.................command frequency (rad/s)
ω ....circular frequency (rad/s)
ζ ....damping ratio

Chapter 1

INTRODUCTION

Many engineering systems create unwanted noise that can be reduced by the careful application of engineering controls. These can be divided into two classes; applications where controls are added to reduce unwanted noise from the environment outside of the system, improving the comfort and safety of human beings, and second, applications where controls are added to change the acoustic response inside of the system, improving performance. The first deals with the attenuation of unwanted environmental noise. The classical example is automobile exhaust noise. The automobile engine creates a pressure pulsation in the engine that transmits down the exhaust system where it is injected into the environment through the tail pipe. Humans perceive this pressure pulsation as undesirable noise (SAE Handbook, 1995). The traditional engineering control consists of adding a muffler to the exhaust system, which damps the dynamic pressure variation resulting in reduced environmental noise (Beranek, 1971; Hosomi, et al., 1993; Morel et al., 1991). Other examples of this class of problem and their traditional noise controls include treating jet engine noise with acoustic liners (Tang and Sirignano, 1973; Kraft et al. 1994), applying Helmholtz resonators to wind tunnels (Heidelberg and Gordon, 1989; Parrott et al. 1988; Anwar 1991), and applying mufflers to pneumatic exhaust nozzles (ASTM E1265-90). A second class of noise control problem deals with removing acoustic resonances in pressurized systems to improve performance, product quality, or safety. An example of this type of problem is an industrial furnace (Tang, and Sirignano, 1973). Oscillations in pressure in a furnace can grow without bound as increases in pressure magnify the combustion rate. Uncontrolled, this scenario can result in catastrophic failure.

In cases where a narrow frequency band of noise exists in an enclosed space (referred to here as the primary acoustic system), a traditional engineering control consists of adding a Helmholtz resonator (Figure 1.1), which is tuned to reduce the unwanted noise by sending it back to the source (Temkin, 1981). The Helmholtz resonator, named in honor of Herman L. F. Helmholtz (1821 – 1894) is a passive acoustic device, which consists of an enclosed hard-walled cavity that communicates with the primary acoustic system via a narrow short neck. It has a tuning frequency determined by the physical dimensions of the neck and cavity. As long as the frequency of the unwanted noise falls within the tuned resonator frequency range, the device is effective. However, if the frequency of the unwanted sound changes to a frequency that does not match the tuned resonator frequency, the device is no longer effective. Some efforts have been made to vary the resonator dimensions with time, to achieve a variable tuned device (Graham, Graves et. Al., 1992; Garret, 1992; and Bedout, Franchek, et. Al., 1997). Nonetheless, these designs require complex mechanisms and have limited tuning capability.

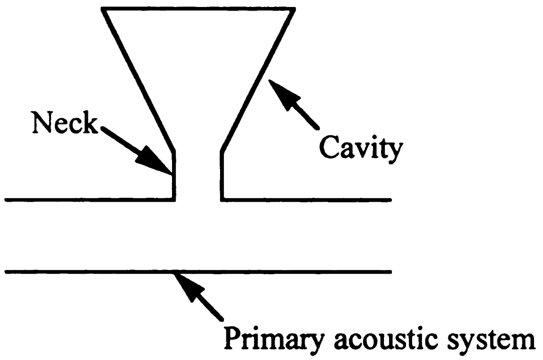

Figure 1.1. Helmholtz resonator connected to a primary acoustic system

This dissertation presents the invention of an electronically tuned semi-active Helmholtz resonator (SHR). This device can be attached to a primary acoustic system, such as a duct, to reduce the transmission of narrow frequency band noise. It can be adaptively tuned on-line to track a disturbance signal with slowly time-varying frequency. It has several advantages over similar inventions. There are no complex moving parts or mechanisms so it is cheaper and easier to implement. The sensitive components are removed from the primary acoustic system and placed in the resonator cavity, so they are less susceptible to damage from harsh environments. The device is fault tolerant: in the event that the controller is turned off, it continues to provide nominal noise reduction. Also, it requires only one connection to the primary acoustic system. No sensors are required external to the device, so that its operation is not dependent on the structure of the primary acoustic system.

The device consists of a classic Helmholtz resonator with a surface of the cavity interior replaced by an acoustic actuator. The actuator is driven by a microphone that senses the pressure in the cavity and a controller that provides the appropriate magnitude and phase between cavity pressure and actuator velocity. This magnitude and phase relationship can be related to an acoustic impedance. The overall SHR impedance is defined by the ratio of the pressure at the resonator inlet to the volume velocity through the inlet. It can be changed by modifying the actuator impedance. With this configuration, the overall acoustic impedance of the device is a function of the resonator's dimensions, which are fixed, and the controller gains, which can be changed electronically on-line.

Each chapter in this dissertation is written to address a separate issue in the performance of the SHR. The chapters are intentionally written to stand alone as separate articles. For this reason, the reader may notice repeated text, equations and figures in separate chapters.

This work presents four major issues. Chapter 2 presents a physical analytical model of the SHR, based on first principles of physics and a control strategy. Chapter 3 presents a model of the power flow and answers the question "where does the sound go?" Chapter 4 compares methods of implementing the SHR. And Chapter 5 presents an adaptive control strategy for tuning the device on-line and tracking a disturbance noise with a slowly time-varying frequency. Concluding remarks and suggestions for future work are presented in Chapter 6. Each article includes experimental results which demonstrate the capability of the device and are compared with the modeled results.

Chapter 2

A Semi-Active Helmholtz Resonator

This chapter presents a new invention; the semi-active Helmholtz resonator (SHR). The SHR consists of a Helmholtz resonator (Ingard, 1953; Selamet and Dickey, 1995) with the addition of a microphone and controller driven, compensated acoustic actuator on one surface of the cavity. An analytical model is presented and used to show that an acoustic impedance on the resonator cavity interior can be controlled to modify the overall acoustic response of the system. This changes the apparent resonant frequency and peak amplitude of the SHR. It demonstrates that a simple proportional-integral controller can be used in the feedback control of the device. It presents an analytical controller design based on an ideal actuator model. A compensated actuator is included in the model to illustrate that the analytical controller design is sensitive to actuator dynamics. This motivates a model-based, empirical controller design which is shown to successfully re-tune the resonator. Experimental lab measurements are presented which demonstrated the tuning ability of the controller and its ability to quiet noise in a duct.

ANALYTICAL RESONATOR MODEL

The Helmholtz resonator is a classic acoustic device which consists of a rigid-wall acoustic cavity with at least one short and narrow orifice, or "neck" through which the fluid filling it communicates with the external medium (Figure 2.1). Temkin, (1936) developed a model to obtain the impedance of an acoustic resonator. He studied the action of a monochromatic wave on the device, under the assumption the lateral dimensions of the cavity were small compared with the wavelength of the incident wave. The cavity creates an acoustic compliance which can be computed from the physical dimensions of the resonator as

$$C_a = \frac{V}{\rho_o c_o^2} \text{ (m}^5\text{/N)} \tag{2.1}$$

where V is the cavity volume, ρ_o is the density of the medium, and c_o is the speed of sound in the medium.

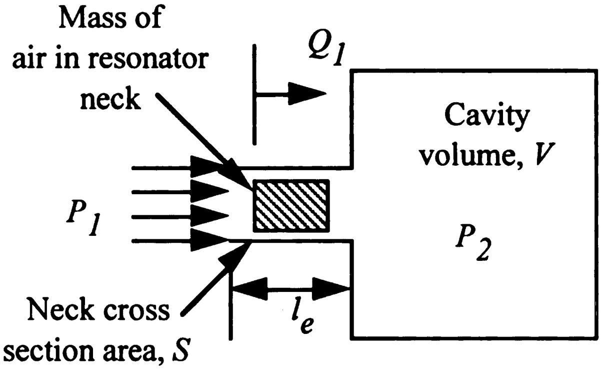

Figure 2.1: Ideal Helmholtz resonator

The mass of air in the neck will oscillate in response to the wave as a solid body with effective inertia

$$I_a = \frac{\rho_o l_e}{S} \text{ (Ns}^2\text{/m}^5\text{)} \tag{2.2}$$

where l_e and S are the effective length and cross sectional area of the neck. When dissipation is small, resonance occurs at a frequency

$$\omega_n = \sqrt{1/C_a I_a} \text{ (rad/s)} \tag{2.3}$$

Summing the forces on the inertia produces a second order differential equation relating the pressure, P_1 (N/m^2), at the entrance of the neck to the volumetric flow rate, or "volume velocity," Q_l (m^3/s). Temkin's model is extended here by converting the differential equation into the transfer function model

$$\frac{Q_1}{P_1} = \frac{1}{I_a}\left[\frac{s}{s^2 + \frac{R_a}{I_a}s + \frac{1}{C_a I_a}}\right] \tag{2.4}$$

where R_a is the resistance due to radiation losses and viscous damping of the medium. Figure 2.2 shows a frequency response of (2.4) with typical values for the acoustic parameters. The magnitude attains a peak at 194 Hz and the phase crosses zero degrees at the same frequency. The peak in magnitude and zero phase are the key characteristics that produce the pressure release boundary that makes the device reflect sound back to the source. This is discussed in detail in Chapter 3.

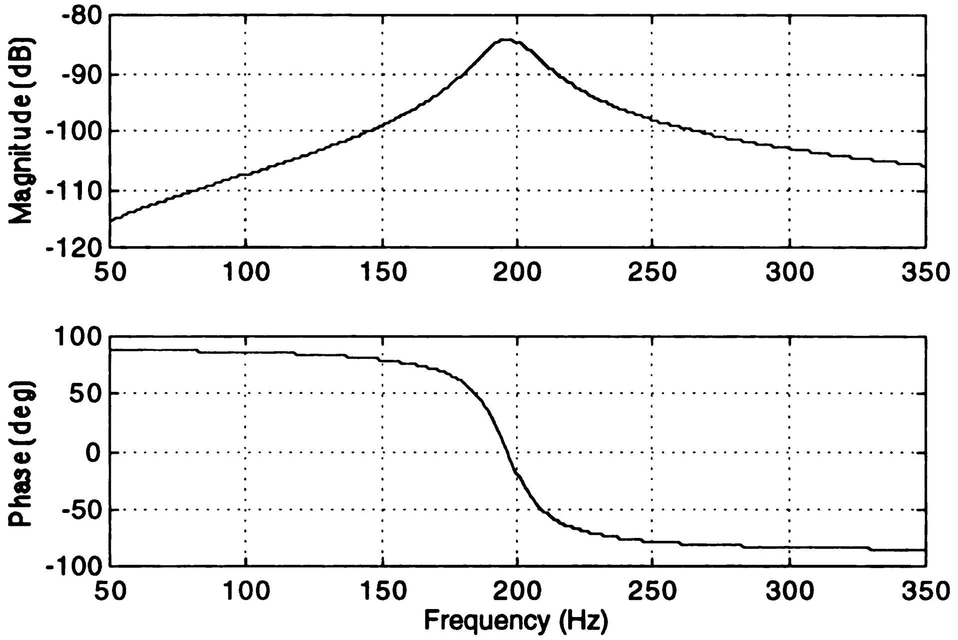

Figure 2.2. Frequency response of a Helmholtz resonator

The complex acoustic impedance of the Helmholtz resonator, Z_1, relates P_1 and Q_1 as

$$P_1 = Z_1 Q_1 \tag{2.5}$$

The ideal Helmholtz resonator model can be modified by adding a boundary condition to the cavity interior surface, relating the surface volume velocity, Q_2, to the pressure acting on the surface, P_2 (Radcliffe and Gogate, 1994) as

$$\frac{P_2}{Q_2} = Z_2(s) \tag{2.6}$$

where Z_2 is an arbitrary acoustic impedance. Figure 2.3 shows a Helmholtz resonator with this boundary condition added.

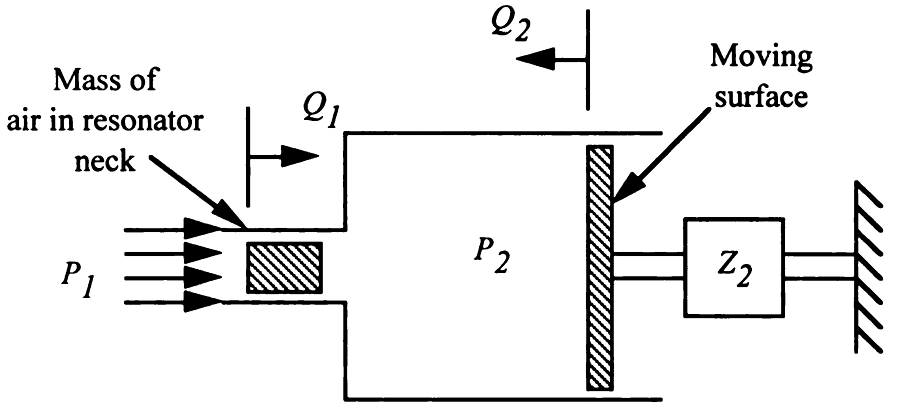

Figure 2.3. Helmholtz resonator with complex impedance boundary condition

State equations can be written for the system by summing the forces on the mass and summing the volume velocities into the cavity. Taking Q_1 and the volume displacement, q_1, as the states gives

$$\begin{bmatrix} \dot{Q}_1 \\ \dot{q}_1 \end{bmatrix} = \begin{bmatrix} \dfrac{-R_a}{I_a} & \dfrac{-1}{C_a I_a} \\ 1 & \dfrac{1}{Z_2 C_a} \end{bmatrix} \begin{bmatrix} Q_1 \\ q_1 \end{bmatrix} + \begin{bmatrix} \dfrac{1}{I_a} \\ 0 \end{bmatrix} P_1 \tag{2.7}$$

The transfer function that relates P_1 to Q_1 can then be found as

$$\frac{Q_1}{P_1} = \frac{1}{I_a} \left[\frac{s - \dfrac{1}{Z_2 C_a}}{s^2 + \left(\dfrac{R_a}{I_a} - \dfrac{1}{Z_2 C_a} \right) s + \dfrac{1}{C_a I_a} \left(1 - \dfrac{R_a}{Z_2} \right)} \right] \tag{2.8}$$

The dynamic response of the system can be modified by specifying Z_2. In particular, a specific value of Z_2 can be found which produces a resonance in the Q_1/P_1 transfer function at an arbitrary frequency and with arbitrary peak magnitude. Solving (2.8) for Z_2 and replacing Q_1/P_1 with a constant, x_o, which specifies the height of the resonant peak, and letting $s = j\omega_c$ gives

$$Z_2 = \frac{\frac{1}{I_a C_a}\left(1 - x_o R_a\right) - j\frac{x_o \omega_c}{C_a}}{\left(x_o \omega_c^2 - \frac{x_o}{C_a I_a}\right) + j\frac{\omega_c}{I_a}\left(1 - x_o R_a\right)} \tag{2.9}$$

where ω_C is a scalar value that represents the frequency of the desired resonant peak. This impedance can be separated into real and imaginary parts by multiplying the complex conjugate of the denominator of (2.9) and collecting real and imaginary parts.

This acoustic impedance control technique can be demonstrated by examining the frequency response of (2.8). For simplicity, the acoustic parameters, I_a and C_a, are set equal to 1, while an arbitrarily small value, $R_a = 0.1$, was chosen. This creates a system with a nominal resonant peak at $\omega = 1$ with the maximum gain $= 1/R_a = 10$ (20 dB). Next, x_o was set to a sufficiently large value and Z_2 was computed for values of ω_C between 0.5 and 1.5. Three graphs were computed with $x_0 = 12, 31$, and 100 (Figure 2.4). These values for x_0 were chosen to correspond to resonant peak magnitudes of 22, 30, and 40 dB. These graphs give the value of Z_2 required to produce a resonant peak at a frequency ω_c with amplitude x_0. The circles represent nine specific values of Z_2 for ω_C = 0.8, 1.0, and 1.2 that are used to generate Figure 2.5. Note the three circles nearly overlap on the Re(Z_2) graph for $\omega_C = 0.8$, and 1.2, and for all values of ω_C on the Im(Z_2) graph. This indicates less variation in Z_2 for these values of x_0 . Note that a smaller impedance requires a larger Q_2 for a given P_2 from the definition of Z_2 (2.6). Therefore, the maximum Re(Z_2) decreases as x_o increases. Also, note the sign of Im(Z_2) changes from positive below the nominal resonant frequency, ω=1, to negative above $\omega = 1$.

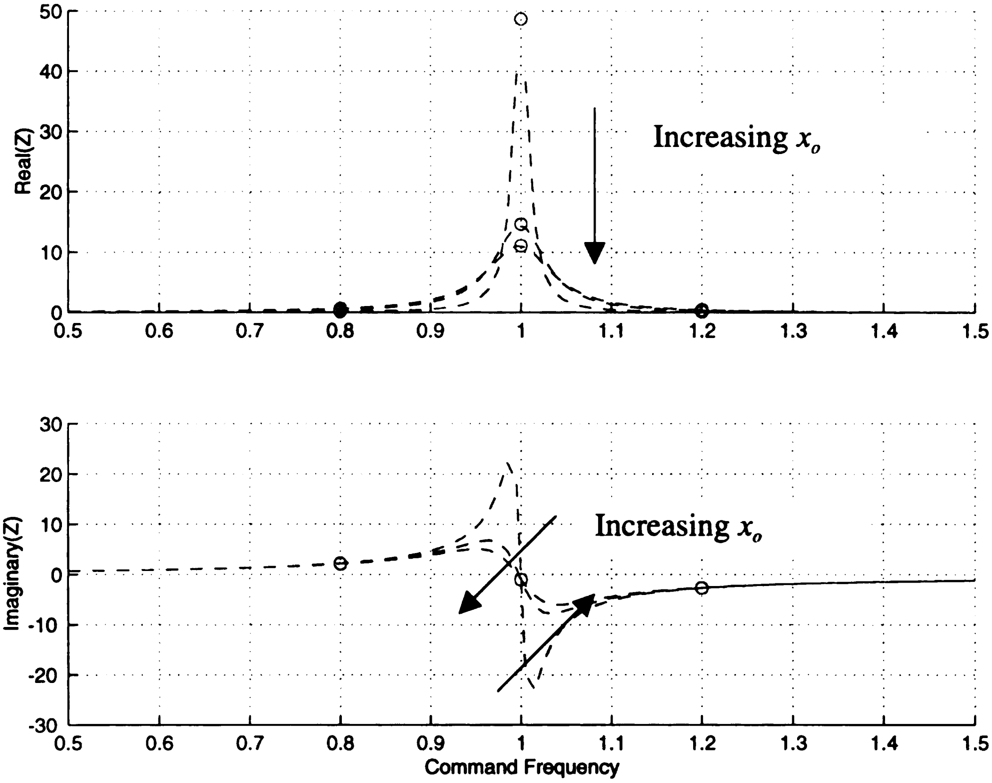

Figure 2.4. Plot of the real and imaginary parts of the controllable acoustic impedance for $x_0 = 21, 31$, and 100 vs. normalized command frequency

Next, the controllable acoustic impedance was applied to the SHR to show how the various values of Z_2 affect the frequency response of the system. The impedance Z_2 was computed from ω_C and x_o, substituted into (2.8) and its frequency response was plotted. Values of ω_C used were 0.8, 1.0 and 1.2. Values of x_0 used were 12, 31, and 100. The nine combinations are shown in Figure 2.5. The resonant peaks are located at $\omega = 0.8$, 1.0, and 1.2, and the arrows indicate the direction of increasing x_0. As x_0 is increased, the height of the resonant peaks is also increased. The maximum magnitudes correspond to the dB values of 12, 31, and 100 (22, 30, and 40 dB). Note that increasing the value of x_0 has the affect of reducing the damping of the system as noted by the increased Q factor and the increased slope of the phase at the zero degree crossing. The Q factor is a measure of the damping in a resonant system that is computed by measuring the band-width, *Δf*, corresponding to the half power points, -3 dB, from the peak. *Q* is computed by $f_n/\Delta f$, where f_n is the frequency at the peak (resonant frequency) (Hartmann, 1997). The percentage damping, ζ of a second order system can be computed from the *Q* factor as $\zeta = 1/2Q$.

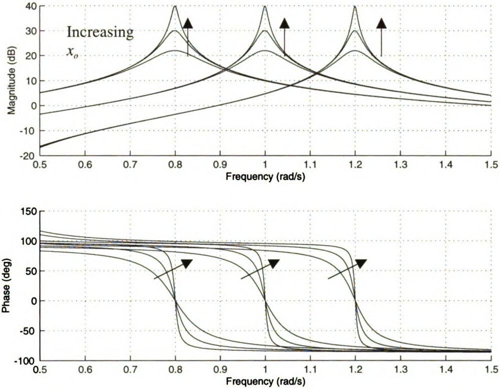

Figure 2.5. Frequency response of SHR system with variable controllable cavity impedance for Z_2 defined by $\omega_C = 0.8$, 1.0, and 1.2, and $x_0 = 12$, 31, and 100 with arrows indicating direction of increasing x_0

Assuming that the disturbance is a narrow frequency band tone at a relatively low frequency, Z_2 can be implemented with a positive feedback, proportional-integral (PI) controller. A positive feedback arrangement is used to keep the sign conventions consistent with Figure 2.3. A PI controller is ideal because it is insensitive to noise, it is generally stable, and it has characteristics that are well understood. The PI controller is not suitable for higher frequencies because the magnitude of the integral signal falls off with increasing frequency. Under this assumption, (2.9) need not be implemented for all frequencies and the controller need not generate a control law corresponding to Figure 2.4. Instead, the controller can implement a single valued complex impedance associated with a single point on the curve in Figure 2.4 which corresponds to the disturbance frequency. Each point on this curve represents an impedance with a real part which can be implemented with a proportional controller, and an imaginary part which can be implemented with an integral controller. The gain, K_I, must be increased with frequency to compensate for the attenuation that occurs with frequency in an integral controller. Note the controller outputs a Q_2 for an input P_2, therefore the controller transfer function is the inverse of Z_2. The control law is given by

$$G(s) = \frac{Q_2}{P_2} = K_P + \frac{K_I}{s} \tag{2.10}$$

where the gains K_P and K_I are given by

$$K_P = \mathrm{Re}\left(\frac{1}{Z_2}\right) \tag{2.11}$$

$$K_I = \omega * \mathrm{Im}\left(\frac{1}{Z_2}\right) \tag{2.12}$$

This produces an analytical controller design based on computing the controller gains K_P and K_I from the relation for Z_2 (2.9) for desired values of ω_C and x_0. Figure 2.6 shows plots of K_P and K_I vs. ω_C computed for all valúes between 0.5 and 1.5 and x_0 = 22, 31, and 100. The circles represent the values for ω_C = 0.8, 1.0, and 1.2 as these controller gains correspond with the response curves in Figure 2.5. The arrow indicates the direction of increasing x_0. Note larger values of K_P are required for larger values of x_o. A negative K_I is required when $\omega_c < 1$, and K_I changes sign when ω_C increases above 1. It should also be noted that the shape of the graphs in both Figures 2.5 and 2.6 will vary depending on the values of the acoustic parameters I_a, R_a, and C_a.

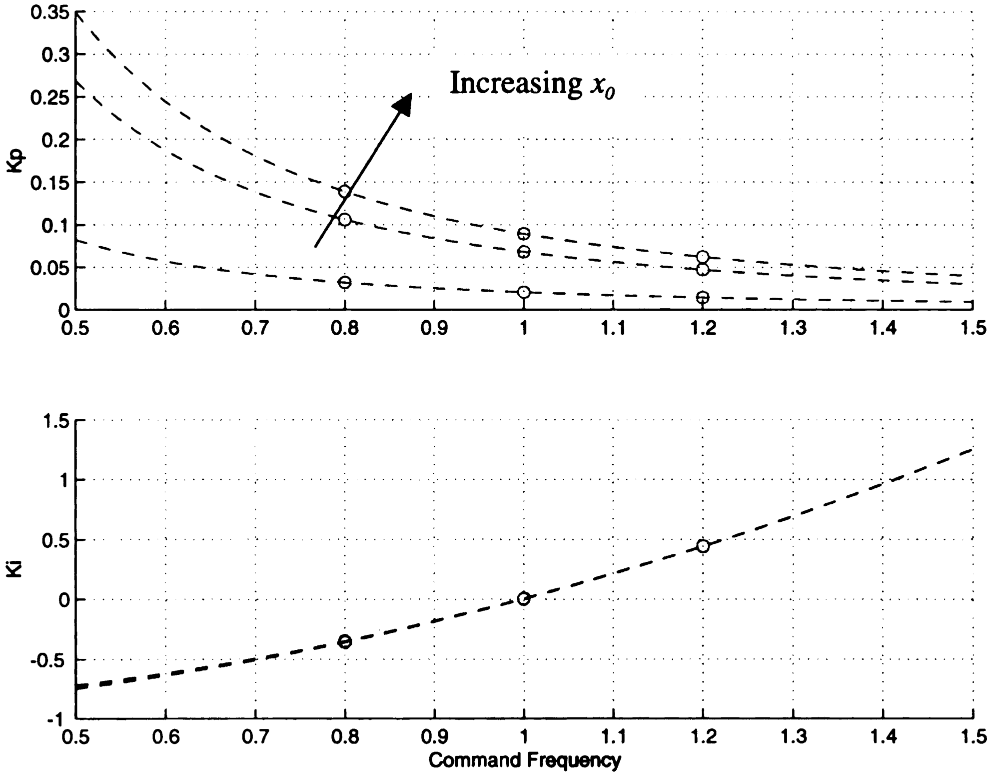

Figure 2.6. Plot of controller gains K_P and K_I vs. command frequency for $x_0 = 22$, 31, and 100 with arrow indicating direction of increasing x_0

The closed loop transfer function in terms of controller gains K_P and K_I can be computed by replacing Z_2 with the inverse of G_c in (2.8) and simplifying which gives

$$\frac{Q_1}{P_1}=\frac{1}{I_a}\left[\frac{s^2-\frac{1}{C_a}\left(K_P+\frac{K_I}{s}\right)s}{s^3+\left(\frac{R_a}{I_a}-\frac{K_P}{C_a}\right)s^2+\left(\frac{1}{I_aC_a}-\frac{K_I}{C_a}-\frac{R_aK_P}{I_aC_a}\right)s-\frac{R_aK_I}{I_aC_a}}\right] \tag{2.13}$$

This form of the transfer function shows how the controller gains affect the system response. The system is obviously not a simple second-order resonator. The denominator of the transfer function is third order polynomial in ‘s’ and the numerator is second order. However, Figure 2.5 shows that it exhibits resonator characteristics. More insight can be drawn from (2.13) by making some simplifying assumptions. For example, letting $R_a = K_P = 0$ and rearranging yields

$$\frac{Q_1}{P_1} = \frac{1}{sI_a}\left[\frac{s^2 - K_I}{s^2 + \left(\dfrac{1 - K_I I_a}{C_a I_a}\right)}\right] \tag{2.14}$$

This equation shows how K_I affects the poles of the transfer function. The term in brackets in the denominator of (2.14) represents the effective resonant frequency (squared) of the system. A positive K_I decreases the effective resonant frequency, and a negative K_I increases the effective resonant frequency. Recall that the control system uses positive feedback. This trend is the reverse of negative feedback systems where positive gain increases the effective stiffness of the system. Also, note the system response is volume velocity relative to pressure. In mechanical resonator systems, the displacement relative to force impedance becomes stiffer as the proportional gain is increased. Displacement is the integral of velocity, explaining why an integral controller gain changes the apparent stiffness in this system. Equation (2.14) also identifies a limit on K_I. If the product of K_I and I_a is made larger than 1 then the system will become unstable as noted by a change in the sign of the s^0 coefficient in the characteristic polynomial (denominator) of (2.14). This occurs when $K_I = 1/I_a$ which makes the resonant frequency equal to zero. However, K_I can be made more negative without bound. This suggests that the resonant frequency can be decreased to zero and increased without bound.

Similarly, by setting $K_I = 0$ gives

$$\frac{Q_1}{P_1} = \frac{1}{I_a}\left[\frac{s - \frac{K_P}{C_a}}{s^2 + \left(\frac{R_a}{I_a} - \frac{K_P}{C_a}\right)s + \frac{1}{I_a C_a}\left(1 - R_a K_P\right)}\right] \tag{2.15}$$

This equations shows that K_P appears as a term that is subtracted from the acoustic loss term R_a. Increasing K_P reduces the apparent acoustic loss and hence reduces the system damping. The apparent acoustic loss can be either increased by a negative K_P, adding additional damping to the system, or decreased with a positive K_P. Reducing system damping increases the peak magnitude at resonance. Equation (2.15) identifies limits on K_P. If the value of K_P/C_a becomes less then R_a/I_a then the system will become unstable, as can be noted from the change in the sign of the s^1 coefficient. Therefore, the largest $K_P = R_a * C_a / I_a$, which produces zero damping and marginal stability.

This analysis illustrates the ability of the SHR to change the dynamic response of the system. Each gain K_P and K_I gives an input to change the apparent resonant frequency and peak amplitude of the Helmholtz resonator. The advantage of this affect is that the response of the Helmholtz resonator is modified without changing the physical dimensions, i.e., cavity volume, neck length or cross section area. The change in response is caused only by the interaction of the controllable cavity acoustic impedance, Z_2, with the Helmholtz resonator.

This design has two important implementation benefits. First, it has the benefit that when the boundary condition is removed, i.e., the controller is turned off, the system reverts to the nominal resonance defined by the physical dimensions of the Helmholtz resonator. Since these dimensions can be designed to meet nominal performance requirements, turning off the controller will only remove the variable tuning leaving the nominal tuning intact. Second, it has the benefit that the sensitive moving parts- microphone and actuator- are not directly in the path of the fluid flow. Instead, they are located inside of the Helmholtz resonator. This provides the advantage that debris carried by the fluid in the system will not come in direct contact with the microphone and actuator.

RESONATOR MODEL WITH ACTUATOR DYNAMICS

An actuator model with finite dynamics can be introduced to study the effects on the system performance and the controller design. The previous analysis assumed that the actuator transfer function was a pure gain. Unfortunately, most commercially available acoustic actuators do not have such ideal response characteristics. Birdsong and Radcliffe (1999) presented an actuator which uses feedback compensation to improve the response of a dual voice coil speaker by compensating for the internal dynamics and the pressure interaction with the acoustic system. While this actuator does not have a transfer function that is a pure gain, its response is a significant improvement over uncompensated speakers. This actuator will be used here. Figure 2.7 shows a block diagram that illustrates how the resonator model is coupled with the speaker model (without the compensator). The speaker has two identical intertwined coils that produce the electromechanical force that drives the speaker. It can be modeled as a three port device with a voltage input, e_p, and current output, i_p, on the primary coil; a current input, i_{bs}, and voltage output, e_{bs}, on the secondary coil; and a pressure input, P_2, and the volume velocity, Q_2 output on the speaker face. The speaker is driven by e_p, and i_{bs} is modeled as an open circuit. The other speaker outputs, i_p and e_{bs}, are used as the inputs to the compensator, which is not included in Figure 2.7. The pressure in the resonator cavity impinges on the speaker face producing the input to the speaker model, resulting in a tightly coupled dynamic system. This combined model will be considered a single block in subsequent models.

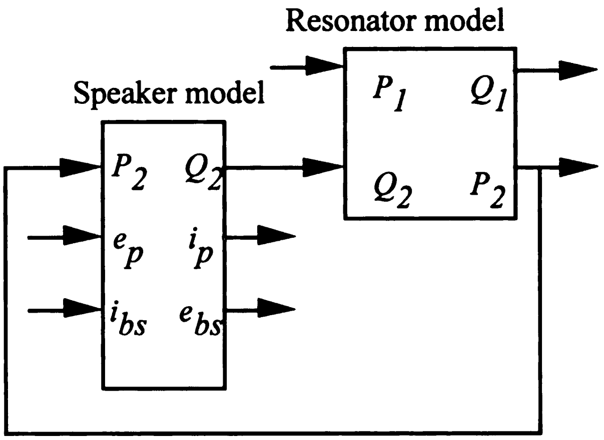

Figure 2.7. Block diagram of speaker model coupled with resonator model through the P_1 and Q_2 signals

The state equations of the Helmholtz resonator and the uncompensated dual voice coil speaker can be assembled by coupling the SHR state equations (2.7) with the model from Birdsong and Radcliffe (1999) through the P_2 and Q_2 signals. These coupled system state equations are given by

$$\frac{d}{dt}\begin{bmatrix} Q_1 \\ q_1 \\ Q_2 \\ q_2 \\ \lambda \end{bmatrix} = \begin{bmatrix} \frac{-R_a}{I_a} & \frac{-1}{C_a I_a} & 0 & 0 & 0 \\ 1 & 0 & 1 & 0 & 0 \\ 0 & \frac{-S_d{}^2}{I_s C_a} & \frac{-R_s}{I_s} & \frac{-1}{C_s I_s} & \frac{blS_d}{I_c I_s} \\ 0 & 0 & 1 & 0 & 0 \\ 0 & 0 & \frac{-bl}{S_d} & 0 & \frac{-R_m - R_c}{I_c} \end{bmatrix} \begin{bmatrix} Q_1 \\ q_1 \\ Q_2 \\ q_2 \\ \lambda \end{bmatrix} + \begin{bmatrix} 0 & 0 & \frac{1}{I_a} \\ 0 & 0 & 0 \\ \frac{S_d bl}{I_s}\left(1 - \frac{M_c}{I_c}\right) & 0 & 0 \\ 0 & 0 & 0 \\ M_c\left(\frac{R_c + R_m}{I_c}\right) & 1 & 0 \end{bmatrix} \begin{bmatrix} i_{bl} \\ e_p \\ P_1 \end{bmatrix} \qquad (2.16)$$

The output equation is given by

$$\begin{bmatrix} Q_1 \\ e_{bs} \\ i_p \\ P_2 \end{bmatrix} = \begin{bmatrix} 1 & 0 & 0 & 0 & 0 \\ 0 & 0 & \frac{bl}{S_d}\left(1 - \frac{M_c}{I_c}\right) & 0 & \frac{-M_c}{I_c{}^2}(R_c + R_m) \\ 0 & 0 & 0 & 0 & \frac{1}{I_c} \\ 0 & \frac{1}{C_a} & 0 & 0 & 0 \end{bmatrix} \begin{bmatrix} Q_1 \\ q_1 \\ Q_2 \\ q_2 \\ \lambda \end{bmatrix} + \begin{bmatrix} 0 & 0 & 0 \\ R_m + \frac{M_c(R_c + R_m)}{I_c} & \frac{M_c}{I_c} & 0 \\ \frac{-M_c}{I_c} & 0 & 0 \\ 0 & 0 & 0 \end{bmatrix} \begin{bmatrix} i_{bl} \\ e_p \\ P_2 \end{bmatrix} \qquad (2.17)$$

where the states are: the acoustic volume velocity and displacement from the neck Q_1 and q_1, the volume velocity and displacement from the speaker Q_2 and q_2, and the electromagnetic flux in the speaker coil λ. The inputs are the primary coil current, i_p, the secondary coil voltage, e_{bs}, and the input pressure to the Helmholtz resonator neck, P_1. The outputs are Q_1, the voltage in the secondary coil, e_{bs}, the current in the primary coil, i_p, and the pressure in the cavity, P_2. Radcliffe and Gogate (1996) discuss the derivation of the parameters of the speaker model which include: the speaker face area, S_d, speaker inertia, I_s, speaker compliance, C_s, speaker friction, R_s, speaker coil resistance, R_c, speaker coil inductance, I_c, speaker coil mutual inductance, M_c, speaker electromechanical coupling factor, bl, and the primary coil current sensing resistance, R_m.

The closed-loop response of the system can be computed by adding the compensator, PI controller, a microphone, and the amplifier models to the speaker and resonator model. Figure 2.8 shows the interconnection of these components with the resonator and speaker models combined into a single block. The pressure in the resonator cavity, P_2, is measured by the microphone with sensitivity, S_{mic}. This signal is fed to the controller which generates a control signal, e_c. The speaker outputs, i_p and e_{bs}, are combined in the compensator and produce the speaker velocity estimate, v_{est}. This signal is subtracted from e_c and a disturbance signal D_I is added. The resulting signal is amplified by K_{amp} and the amplified signal becomes the input to the actuator, e_p.

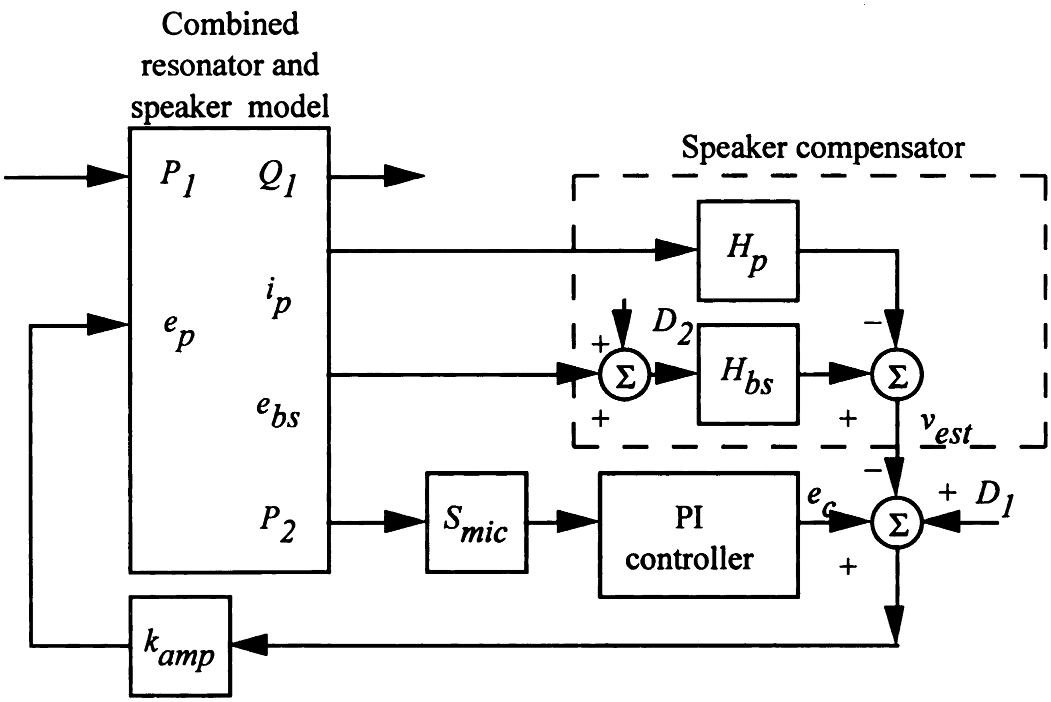

Figure 2.8. Block diagram of resonator and speaker model with compensator and PI controller

Table 2.1. SHR Model Parameter Values

bl	2.45 N/A		R_c	4.875 ohm
c_o	343 m/s		R_m	50 ohm
C_s	0.000868 m/N		R_s	3.745 N sec/m
I_c	0.002 H		S	0.000254 m^2
I_s	0.0076 Kg		S_d	0.0133 m^2
le	1 cm		V	0.0102 m^3
M_c	0.001 H		ρ_o	1.18 Kg/m^3
S_{mic}	4 mv/ P_A		I_a	160 Ns$_2$/m$_5$
R_a	7.5e4 Ns/m$_5$		C_a	7.20e-9m$_5$/N

These results show that the analytical controller design is not effective in the presence of unmodeled actuator dynamics. The feedback controller, resonator, and compensated speaker model did not exhibit the desired resonant frequencies and amplitudes when the controller gains, predicted by the analytical controller design, (2.9) – (2.12), were used. The analytical mapping of the gains to the resonant frequency and peak amplitude was no longer effective. Even with the compensator, the speaker response exhibited excessive deviation from the ideal actuator model response. This leads to the conclusion the analytical controller design was useful in motivating the use of a PI controller, but is too sensitive to actuator dynamics and is not effective in choosing the controller gains. It should be noted that this does not mean the SHR can not be implemented. It only means the relatively simple mapping between controller gains and system response is not sufficient. The mapping must include more factors, in particular, the actuator model must be included in the controller design. Unfortunately, the actuator model adds considerable complexity to the mapping, making a closed-form solution intractable. This motivates the use of a model-based empirical controller design.

An empirical technique, motivated by the above formulation was applied to the model to produce the controller design. The model response was simulated for various gains to determine the mapping between the controller gains and the system response. The strategy was to find gains, K_P and K_I, that placed the resonance at various frequencies, while maintaining the same peak amplitude. It was found that K_P modified the amplitude and K_I modified the resonant frequency as predicted by the analytical controller design, but the functional relationship was different than predicted. Figure 2.9 shows the frequency response of the Q_1/P_1 transfer function for three sets of controller gains. Figure 2.10 shows the frequency response for the P_2/D_l transfer function with the same gains. Figure 2.10 will be compared to laboratory measurements. The controller places the resonant frequency between 110 and 150 Hz while maintaining a maximum peak of equal magnitude for all cases. Table 2.2 shows the gains K_P and K_I vs. ω_n used to generate Figures 2.9 and 2.10. Chapter 4 examines the relationship between the PI controller gains and system response in more detail.

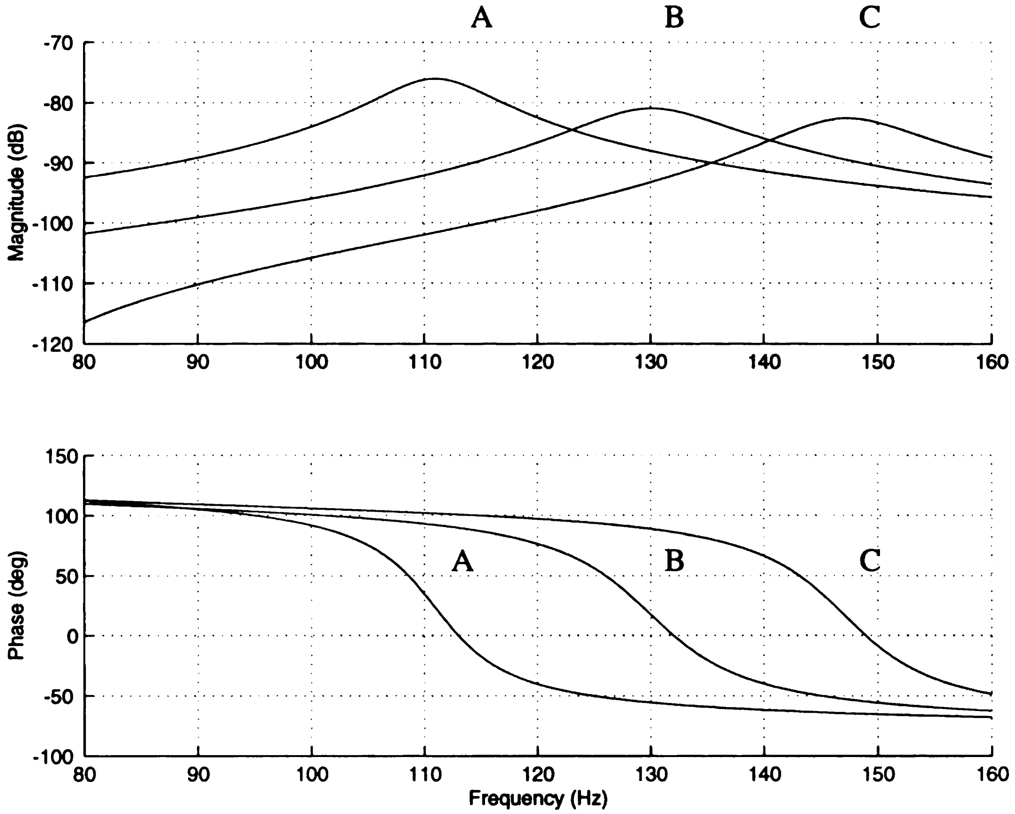

Figure 2.9. Closed-loop frequency response of the Q_1/P_1 transfer function for model including actuator dynamics

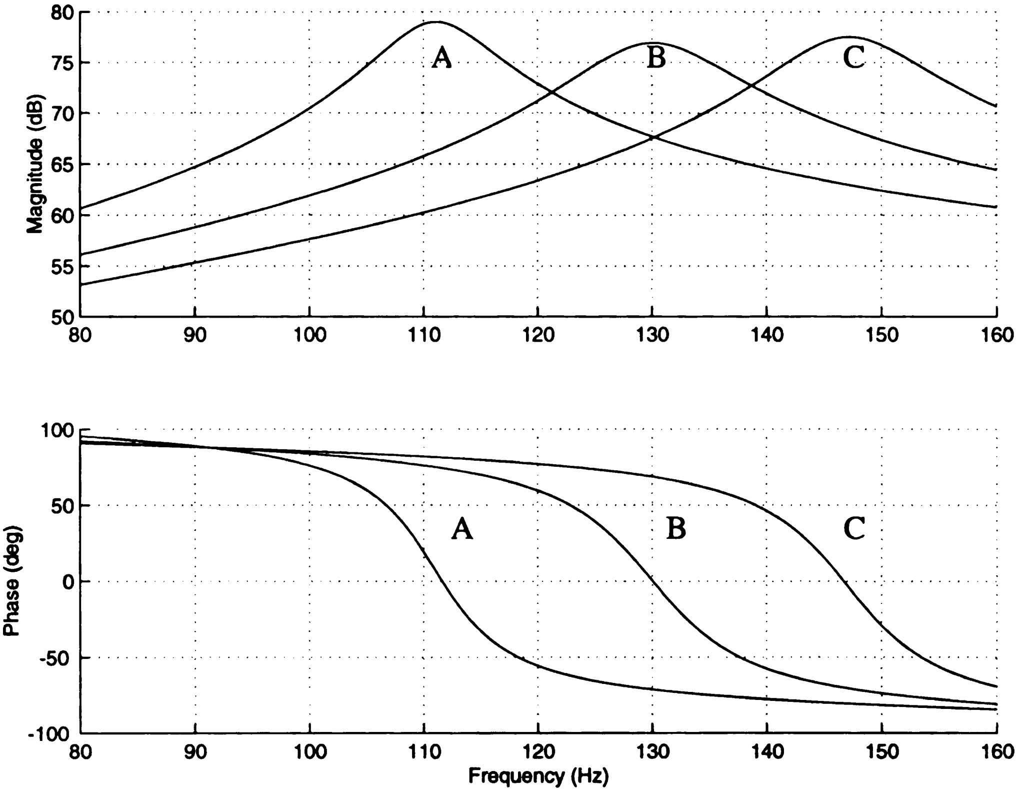

Figure 2.10. Closed-loop SHR frequency response for P_2/D_I transfer function for model including actuator dynamics

Table 2.2. Controller gains identified by model-based empirical controller design

Graph	Resonant Frequency Hz	K_P Gain	K_I Gain
A	112	0.99	-100
B	130	0.99	0
C	145	0.99	100

Figures 2.9 and 2.10 show that the controller successfully achieves the goal of re-tuning the resonator with the actuator. Figure 2.9 clearly shows that varying K_I and K_P results in changing the system resonant frequency and peak amplitude. This result indicates that the compensated acoustic actuator will perform the task of the complex boundary condition as hoped.

EXPERIMENTAL VALIDATION

An experimental apparatus was constructed to validate the theoretical model and to demonstrate the noise reduction capability of the device. In this section the Helmholtz resonator and actuator implementation will be discussed, the PI controller design will be demonstrated and finally, the SHR will be applied to an acoustic duct to demonstrate the control algorithm and noise reduction capability.

The experimental SHR setup consisted of two components: a Helmholtz resonator cavity and a microphone-compensated actuator system. Figure 2.11 shows a photograph of the SHR connected to an acoustic duct and Figure 2.12 shows a schematic of the setup. A cylindrical Helmholtz resonator cavity was constructed from PVC with dimensions 0.075 m in diameter and 0.15 m in length. A cylindrical neck with dimensions 0.018 m diameter and 0.01 m in length, was fitted on one face of the cavity. The microphone-compensated actuator system consisted of a half inch B&K type 4155 microphone sealed through the wall of the cavity. A D-Space Model #1102 floating point, digital signal processor (DSP) was used to implement the speaker compensation, and an acoustic actuator was sealed in the opposite face of the cavity. A DSP sampling rate of 5 kHz was used for all experiments.

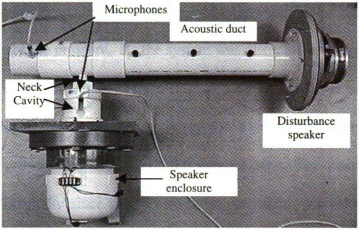

Figure 2.11. Photograph of SHR connected to an acoustic duct with a second audio speaker to inject noise

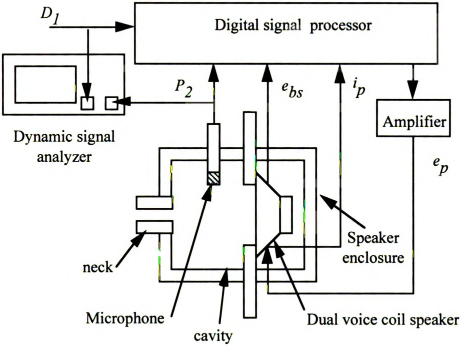

Figure 2.12. Schematic diagram of experimental SHR apparatus

In all phases of the system design, the device was separated from any primary acoustic system. This was not done arbitrarily for convenience, but because traditionally, mechanical and acoustic resonators are designed independently from the primary system. The usefulness of the device would be limited if the resonator response was dependent on the structure of the primary system. Fortunately, this is not the case; resonators can be designed with a tuning frequency and then applied to any suitable primary system. In the absence of a disturbance pressure, P_1, the system was disturbed electrically by the signal D_I injected via the actuator input voltage (Figure 2.8). Although it would be useful to measure the Q_1/P_1 transfer function directly since it is key in the interaction between the resonator and the primary acoustic system, this was not done. The quantity Q_1 is difficult to measure experimentally since it is a zero mean, oscillating air velocity. Although a laser velocity anemometer is a device that can be used for such measurements, it is extremely costly, and experimentally complex. Consequently, the transfer function Q_1/P_1 is difficult to measure directly. Alternatively, the signal, P_2, and therefore, the transfer function P_2/D_I can be measured easily with a microphone. The system can be disturbed by either inputs P_1 or Q_2 since the characteristic polynomial which defines the resonant frequencies is the same regardless of the input. Therefore, the model was validated by comparing the model response for P_2/D_I with experimental measurements.

Speaker Compensation

The goal of the compensation is to produce a constant magnitude and phase relationship between the desired velocity and the actual speaker face velocity. The actuator consisted of a 6 inch dual voice coil speaker with local compensation (Birdsong and Radcliffe, 1999). It was compensated for the mechanical dynamics associated with the mass and compliance of the speaker assembly. It was also compensated for the pressure impedance on the speaker face which becomes critical when applying a control input to an acoustic cavity near an acoustic resonant frequency, as in this experiment.

The actuator was compensated to improve the speaker performance, but finite gain and phase errors in the actuator response affected the system. A speaker velocity estimator (Birdsong and Radcliffe, 1999; Radcliffe and Gogate, 1996) was implemented by combining the voltage in the secondary coil with the current in the primary coil. A 10 ohm resistor was placed in series with the primary speaker coil to measure the current. The velocity estimate was then used to close the loop on the speaker velocity with a proportional controller (Figure 2.13). A value of 30 was used for K_{amp} for all trials. This value for K_{amp} is somewhat smaller than values used by Birdsong and Radcliffe (1999) where gains of as much as 100 were used. The gain K_{amp} was chosen to increase the robustness of the system, which comes at the expense of performance. The speaker velocity was measured directly to confirm that the transfer function of the actual speaker velocity relative to the desired velocity was acceptable. This was done by directing a laser velocimeter through the SHR neck onto reflective tape on the speaker face. With the relatively low value of K_{amp}, there was less than 5 dB and 100 degrees of magnitude and phase between desired and actual speaker velocity in the frequency range of 20 to 200 Hz in all experiments. While this represents a 15 dB and 80 degree improvement over uncompensated audio speakers, it clearly does not approach the response of the ideal actuator model. After the speaker compensator was implemented, the closed-loop speaker compensation was considered a single block in the SHR, and all subsequent open and closed-loop SHR experiments included closed-loop speaker compensation.

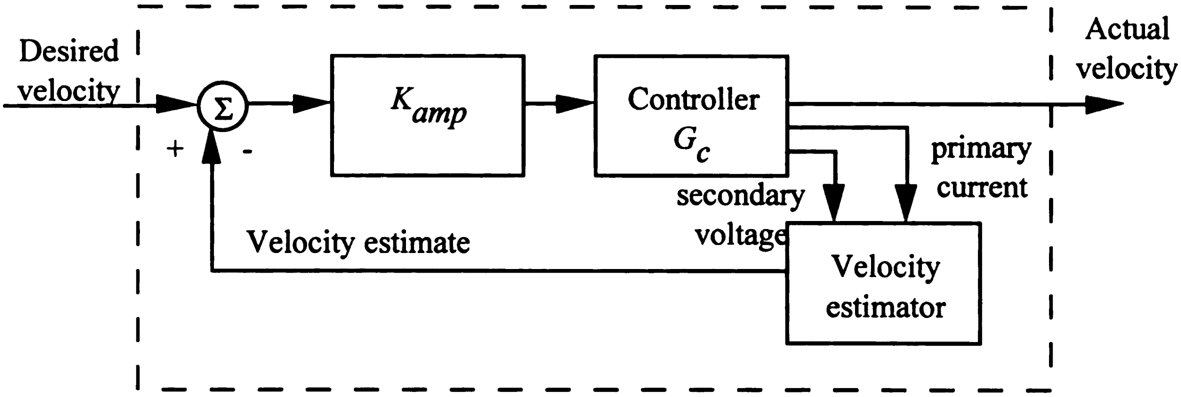

Figure 2.13. Block diagram of dual voice coil speaker compensation used in SHR actuator

PI Controller Design

The PI controller was implemented and closed-loop SHR response was recorded with controller gains $K_P = K_I = 0$. In this configuration, the compensator attempts to hold the speaker face fixed in the presence of the disturbance. White noise was input as the disturbance to the system and the transfer function of P_2/D_l was measured using a Hewlett Packard dynamic signal analyzer model #35660A. With the SHR disconnected from a primary acoustic system, resonance was observed as a peak in the frequency response of the P_2/D_l transfer function. The results indicated that a resonant peak occurred at 120 Hz, however there was significant damping in the system which reduced the peak amplitude. This damping was attributed to mechanical damping in the form of friction and electrical power dissipation in the current sensing resistor, R_m, in the speaker compensator. This damping is large compared to the acoustic damping expected in a passive Helmholtz resonator. Other experiments indicated that damping was significantly reduced when current was not allowed to flow through the sensing resistor.

The closed-loop response was then measured with various non-zero controller gains. As predicted by the model, the analytical mapping between K_P and K_I and the resonant frequency and peak amplitude, (2.9) – (2.12), did not produce the desired results. This was attributed to the deviation of the actuator from the ideal model. Even with the compensator, the effects of the speaker dynamics were not sufficiently minimized.

The empirical technique was used in place of the analytical mapping to tune the system in the presence of significant actuator dynamics. The PI controller design was based on qualitative information learned from the model. The objective was to find gains, K_P and K_I, that placed the resonance at various frequencies, while maintaining the same level of damping. The data was collected by fixing K_I, searching for a K_P that produced the desired peak amplitude, and recording the resonant frequency. The gains K_P and K_I are plotted against resonant frequency in Figure 2.14. Note that although there is a difference in the magnitude, the overall trends of these graphs agree with the data derived from the model in Table 2.2. The K_P gain is negative for all values of ω_C with the most negative value at the nominal resonant frequency (130 Hz). Only a 10% change in K_P is required for the entire range of ω_n. The model predicted that K_P had no change in the range of ω_n = 110 to 145 Hz. The K_I gain ranges from –100 to 200 and passes through zero at the nominal resonant frequency.

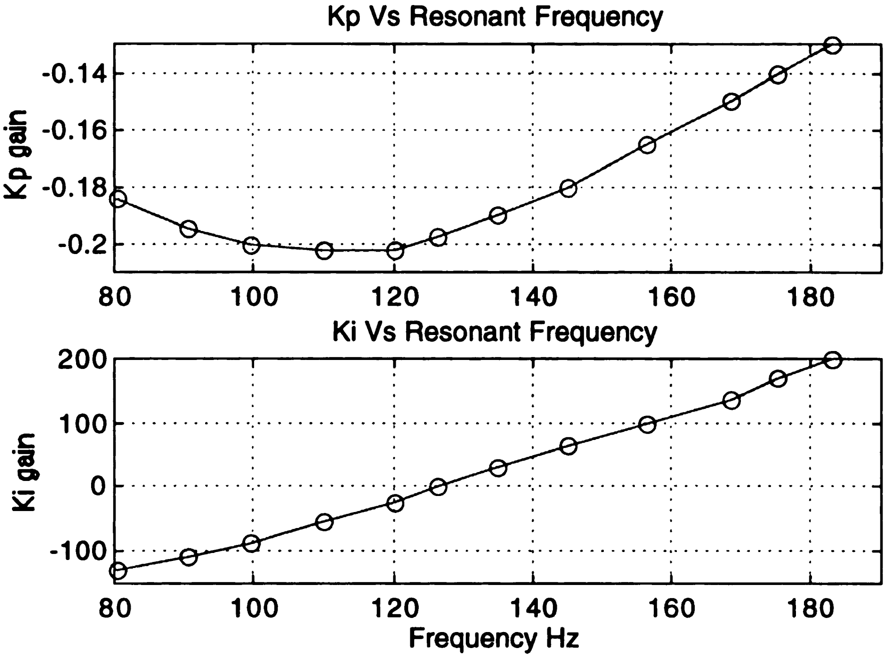

Figure 2.14. Graph of K_P and K_I vs. ω_n determined using an experimental empirical technique

The tuning capabilities of the device are illustrated by the closed-loop frequency response measurements (Figure 2.15). The five graphs show the resonant peak for five separate experiments with ω_n = 80, 110, 140, and 170 Hz and one graph for the controller gains set to zero. Note that the SHR with the gains set to zero is over-damped with approximately 45% damping. With the controller turned on, a resonance is exhibited and positioned at the desired frequency with approximately 5% damping for all cases. This result demonstrates the ability of the controller to tune the SHR to arbitrary frequencies.

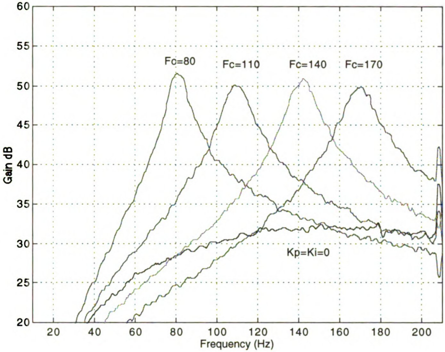

Figure 2.15. Experimental frequency response P_2/D_1 transfer function with $\omega_n = 80, 110, 140$, and 170 Hz and with gains set to zero

An additional experiment was performed to demonstrate the application of the SHR in an acoustic duct system. The SHR was connected to a 3 inch diameter and 32 inch long duct (Figure 2.16). A separate audio speaker was mounted on one end of the duct to inject noise and the other end was left open. A pure 140 Hz tone was injected into the duct and the sound level P_3 was measured in the duct 2 inches from the end with a 1/2 inch B&K microphone. The gains K_P and K_I were set to tune the SHR to 140 Hz and the time response of the microphone signal was recorded as the controller was applied. Figure 2.17 shows P_3 vs. time in open-loop for 0.05 seconds, then the controller is activated. There is a short transient then the P_3 signal is reduced by a factor of approximately 6.7 (-16 dB). Similar results were obtained with the disturbance tones with frequencies ranging from 80 to 180 Hz.

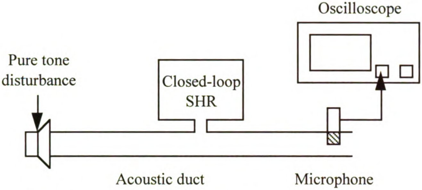

Figure 2.16. Schematic of SHR applied to acoustic duct

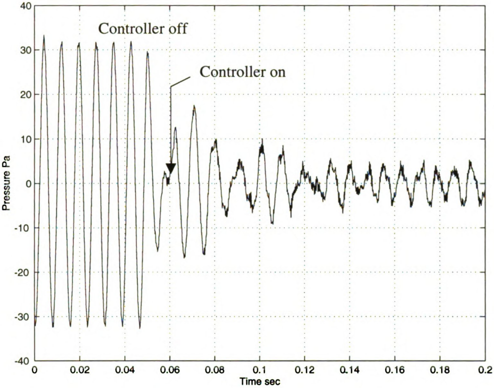

Figure 2.17. Time response of pressure 2 inches from the duct end with a 140 Hz disturbance as the controller is activated, showing a 16 dB noise reduction

CONCLUSIONS

This work presented an electronically tuned semi-active Helmholtz resonator which can be used to quiet noise in enclosed acoustic systems. An analytical model was presented and used to show that an acoustic impedance on the resonator cavity interior can be controlled to modify the overall acoustic response of the system. This changes the apparent resonant frequency and peak amplitude of the acoustic response. It was shown that a simple proportional-integral controller can be used in the feedback control of the device. An analytical mapping solution between the actuator impedance and the controller gains was developed for an ideal actuator, and an empirical mapping technique was developed for an actuator with significant dynamics. A compensated audio speaker was included in the model to demonstrate the effects of actuator dynamics. Experimental lab measurements were presented which demonstrated the tuning ability of the controller and its ability to quiet noise in a duct.

The SHR system represents a powerful new tool in tuning acoustic systems. It adds a nominal resonance to an acoustic system and allows the resonance frequency and peak magnitude to be changed on-line continuously over a range of frequencies. It has advantages over other technologies in that it does not add significant mechanical complexity, it is fault tolerant, and the design places the sensitive sensor and actuator away from the direct path of the process.

Chapter 3

Sound Reduction and Power Flow of the Semi-Active Helmholtz Resonator in an Acoustic Duct

Examination of the acoustic power flow for the semi-active Helmholtz resonator (SHR) and its role in noise reduction in an acoustic duct is considered here. A theoretical model is presented and analyzed to determine the optimum conditions for reducing the transmitted noise in a primary acoustic system with the SHR. These results are used to demonstrate the effectiveness of the SHR in changing the tuned frequency. Experimental results are given and compared with the theoretical model.

MODEL DEVELOPMENT

Power Flow Model

The system of interest is a rigid, long straight duct with a constant cross sectional area, A_D, a SHR attached to the wall at $x = 0$, and a source generating sound at one end of the duct. Figure 3.1 shows a schematic of the system with arrows indicating the directions of incident, reflected, absorbed, and transmitted power.

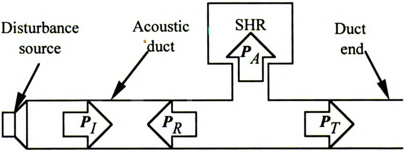

Figure 3.1. Schematic diagram of SHR and acoustic duct showing incident, reflected, absorbed, and transmitted power towards open end

The objective of this study is to develop a relationship for the various power quantities in terms of the SHR properties. A lumped-parameter model (Pierce, 1981) is used which neglects dissipation in the duct, incorporates one-dimensional acoustic theory, assumes continuous pressure, and assumes that the volume velocity is conserved at the junction giving

$$Q_I = Q_A + Q_T \tag{3.1}$$

where Q_I, Q_A, and Q_T are the volume velocities (m^3/s) of the incident, absorbed and transmitted paths. The pressure in the duct is continuous, so the pressure in each path at the intersection is equal

$$P_I = P_A = P_T \tag{3.2}$$

where P_I, P_A, and P_T are the pressures (N/m^2) in the incident, absorbed, and transmitted paths. The relationship between P and Q across a section is named acoustic impedance. Dividing (3.1) by (3.2) gives a relationship between the acoustic impedances for each path as

$$Z_I^{-1} = Z_A^{-1} + Z_T^{-1} \tag{3.3}$$

where Z_I, Z_A, and Z_T are the acoustic impedances (Ns/m^5) of the incident, absorbed and transmitted paths.

The acoustic impedance of the incident path is analyzed by considering the forward traveling and reflected pressure wave in the incident path. The total incident pressure is given by the sum of the forward and reflected wave amplitudes,

$$P_I = \hat{f}\left(e^{-ikx} + \Re e^{ikx}\right) \tag{3.4}$$

where $\hat{f}$ is the pressure amplitude, k is the wave constant (ω/c), x is the spatial variable, and $\Re$ is the pressure-amplitude reflection coefficient that gives the ratio of the reflected to incident pressure wave amplitude. The volume-velocity in the incident path is given by

$$Q_I = \frac{\hat{f}A_D}{\rho c}\left(e^{-ikx} - \Re e^{ikx}\right) \tag{3.5}$$

where ρ is the density (kg/m^3) of the medium, and c is the speed (m/s) of sound. The quantity $\rho c/A_D$ can be defined as Z_0 and represents the acoustic impedance of air in a free field. The acoustic impedance in the incident path is given by the ratio of the pressure to the volume-velocity,

$$Z_I \equiv \frac{P_I}{Q_I} \tag{3.6}$$

Substituting (3.4) and (3.5) into (3.6) gives

$$\frac{Z_I}{Z_0} = \frac{1+\Re}{1-\Re} \tag{3.7}$$

Solving $\Re$ gives,

$$\Re = \frac{Z_I - Z_0}{Z_I + Z_0} \tag{3.8}$$

Substituting (3.3) for Z_I in (3.8) gives

$$\Re = \frac{\left(Z_A^{-1} + Z_T^{-1}\right)^{-1} - Z_0}{\left(Z_A^{-1} + Z_T^{-1}\right)^{-1} + Z_0} \tag{3.9}$$

These results are valid for general values, Z_A, Z_O, and Z_T. However, by considering an idealized boundary condition at the duct end at $x = L$, further analysis can be developed. Consider "anechoic termination" at the duct end so that no reflections occur. While it is difficult to realize such a boundary condition on an acoustic duct, it simplifies the model sufficiently and deviations from this ideal case can be accounted for in experimental results. Under this assumption, $Z_T = Z_0$ and (3.9) can be simplified to give the reflection coefficient, $\Re$ in terms of Z_A and Z_0 as

$$\Re = \frac{-1}{1 + \frac{2Z_A}{Z_0}} \tag{3.10}$$

The transmission coefficient, T gives the amplitude of the transmitted pressure relative to the incident pressure and is given by

$$\mathrm{T} = 1 + \Re \tag{3.11}$$

The fractions of reflected, transmitted and absorbed power to incident power are given by (Pierce, 1981)

$$\mathbf{P}_R / \mathbf{P}_I = |\Re|^2 \tag{3.12}$$

$$\mathbf{P}_T / \mathbf{P}_I = |\mathrm{T}|^2 \tag{3.13}$$

$$\mathbf{P}_A/\mathbf{P}_I = 1 - |\Re|^2 - |T|^2 \tag{3.14}$$

These equations, (3.12), (3.13), and (3.14), are ratios of reflected, transmitted, and absorbed power relative to incident power. The ratios $\mathbf{P}_R/\mathbf{P}_I$ and $\mathbf{P}_T/\mathbf{P}_I$ can range from zero to one, and it can be shown that $\mathbf{P}_A/\mathbf{P}_I$ attains a maximum of one half when the ratio of Z_A/Z_T is one half.

The transmission of power through the intersection depends on the impedance Z_A, which can theoretically vary from 0 to ∞. When $Z_A = \infty$, the SHR acts as a rigid wall. In this case, $\Re = 0$, and $T = 1$, i.e., there is no reflection ($\mathbf{P}_R/\mathbf{P}_I = 0$) and all the power is transmitted ($\mathbf{P}_T/\mathbf{P}_I = 1$). This scenario is equivalent to no SHR present and the system consists of simply a rigid duct which transmits sound perfectly. When $Z_A = 0$ the intersection behaves as an ideal "pressure release" boundary. In this case $\Re = -1$ and $T = 0$, i.e., all of the incident power is reflected ($\mathbf{P}_R/\mathbf{P}_I = 1$) and none is transmitted ($\mathbf{P}_T/\mathbf{P}_I = 0$). The pressure release is the boundary condition used to model a duct with the end open to atmospheric pressure; the pressure at the open end equals zero regardless of the flow. Theoretically, a duct with an open end will be purely reflective with the reflected wave inverted. A pressure release boundary is also used to model the boundary between fluids of significantly varying density such as water and air (Pierce, 1981). In reality the SHR impedance will fall between these extremes, resulting in finite values of Z_A.

Transmission Loss (*TL*) is a measure of the power flow which is commonly used in acoustics (Blaser and Chung, 1978). It is the ratio of transmitted to incident power and is given by

$$TL = \left(\mathbf{P}_T \big/ \mathbf{P}_I \right)^{-1} = \frac{1}{|1+\Re|^2} \tag{3.15}$$

Note that TL is the inverse of $\mathbf{P}_T/\mathbf{P}_I$ and increases as the transmitted power is reduced relative to the incident power. For example, the pressure release condition ($Z_A = 0$, $\Re = -1$) gives $TL = \infty$.

Impedance Control of SHR

The purpose of the SHR is to create a variable Z_A to control the power flow in the system, therefore, a careful analysis of the relationship between Q_A and P_A is needed. A theoretical model of the SHR (Chapter 2) will be described briefly here so that it can be examined in terms of power. The SHR consists of a Helmholtz resonator with one surface of the cavity replaced by a moving surface (Figure 3.2). The system can be represented by the linear time invariant state equations of the form

$$\begin{bmatrix} \dot{Q}_A \\ \dot{V} \end{bmatrix} = \begin{bmatrix} \frac{-R_a}{I_a} & \frac{-1}{I_a C_a} \\ 1 & 0 \end{bmatrix} \begin{bmatrix} Q_A \\ V \end{bmatrix} + \begin{bmatrix} \frac{1}{I_a} & 0 \\ 0 & 1 \end{bmatrix} \begin{bmatrix} P_A \\ Q_C \end{bmatrix} \tag{3.16}$$

$$\begin{bmatrix} Q_A \\ P_C \end{bmatrix} = \begin{bmatrix} 1 & 0 \\ 0 & \frac{1}{C_a} \end{bmatrix} \begin{bmatrix} Q_A \\ V \end{bmatrix} \tag{3.17}$$

where the states are Q_1, the volumetric flow rate or "volume velocity" from the neck (m^3/s) and V, the sum of the volumes introduced through the neck and the inner surface of the cavity (m^3). The inputs are P_1, the pressure at the neck inlet to the cavity (N/m^2), and Q_2, the volume velocity from the movable surface in the cavity (m^3/s). The outputs are Q_1 and P_2, the pressure in the cavity (N/m^2). The other parameters are R_a, the acoustic loss that represents viscous and radiation losses (Ns/m^5), I_a, the acoustic inertia of the mass of air in the resonator neck (Ns^2/m^5), and C_a, the acoustic compliance of the cushion of air in the resonator cavity (m^5/N). An acoustic impedance can be generated on the moving inner surface of the cavity by enforcing a control law between Q_2 and P_2. This closed-loop, positive feedback configuration is shown in Figure 3.3.

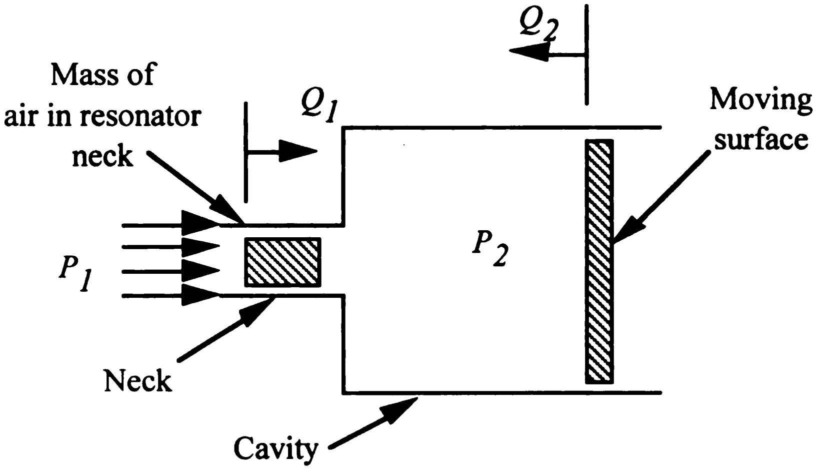

Figure 3.2. Schematic diagram of SHR showing inertia effect in neck and the movable surface in the cavity interior

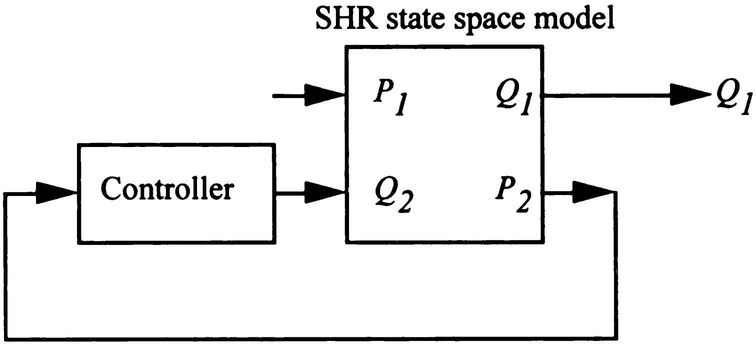

Figure 3.3. Closed-loop SHR system block diagram

Once a control law is chosen, the closed-loop transfer function relating Q_A to P_A and the power flow can be computed. A proportional-integral (PI) controller,

$$G_c(s) = \frac{Q_C}{P_C} = K_P + \frac{K_I}{s} \tag{3.18}$$

produces the desired response (Chapter 2), where K_P and K_I are the proportional and integral gains respectively. The closed-loop transfer function for Q_A / P_A can be computed by combining (3.13) with (3.11) and (3.12) and converting the state equations into the transfer function (Phillips and Harbor, 1996)

$$\frac{Q_A}{P_A} = \frac{1}{Z_A} = \frac{1}{I_a}\left[\frac{s^2 - \frac{1}{C_a}\left(K_P + \frac{K_I}{s}\right)s}{s^3 + \left(\frac{R_a}{I_a} - \frac{K_P}{C_a}\right)s^2 + \left(\frac{1}{I_aC_a} - \frac{K_I}{C_a} - \frac{R_aK_P}{I_aC_a}\right)s - \frac{R_aK_I}{I_aC_a}}\right] \tag{3.19}$$

This equation gives Q_A / P_A (the reciprocal of Z_A) in terms of acoustic parameters which are fixed, and controller gains which can be changed on-line. The above transfer function shows how the acoustic impedance can be changed on line by varying the control gains.

The power flow of the duct and SHR system can be modified on-line by varying Z_A through the controller gains K_P and K_I. The simple case where K_P and K_I are zero corresponds to the condition where the movable boundary in the cavity is held fixed. In this case (3.19) reduces to a simple second order transfer function, consistent with classic Helmholtz resonator theory (Pierce, 1981; Selamet et at., 1995; Tang and Sirignano, 1973), giving

$$\frac{Q_A}{P_A} = \frac{1}{Z_A} = \frac{1}{I_a}\left[\frac{s}{s^2 + \frac{R_a}{I_a}s + \frac{1}{I_aC_a}}\right] \tag{3.20}$$

The denominator of (3.15) is a second order polynomial and resonance will occur when the inertia effects balance the compliance effects leaving only the resistive forces. This occurs at the resonance frequency

$$\omega_n = \sqrt{\frac{1}{I_a C_a}} \tag{3.21}$$

The resonance frequency is important because at this frequency, for the classic Helmholtz resonator resulting from no control action (3.19), Z_A attains the maximum value

$$Z_A = R_a, \quad (\omega = \omega_n, K_p = K_I = 0) \tag{3.22}$$

Substituting (3.19) into (3.10) and computing *TL* (3.15) gives the maximum *TL* at the resonance frequency,

$$TL = \frac{Z_T}{R_a} + 1, \quad (\omega = \omega_n, K_P = K_I = 0) \tag{3.23}$$

This introduces the somewhat surprising result that the *TL* is inversely proportional to R_a, that is, reducing the dissipation in the system will decrease the transmitted power. This highlights the fact that the device does not actually absorb energy, but rather, it reflects energy thus reducing the transmitted energy.

The frequency dependence of the SHR transfer function (3.20) indicates how the SHR (with gains, K_P and K_I, set to zero), selectively absorbs sound in a narrow frequency range. Figure 3.4 shows the frequency dependence of the *TL*, computed by substituting $s = j\omega$, and plotting *TL* in dB vs. normalized frequency ω/ω_n as R_a is decreased. The parameters used in the simulation were identified experimentally for the SHR used in the model validation. They represent the nominal response of the SHR with the gains set to zero. The parameters are A_D = 4.40e-3 m^2, C_a = 7.20e-09 m^5/N, I_a = 162

Ns^2/m^5, and R_a = 7.54 e 4 Ns/m^5. Although these parameters seem somewhat arbitrary, the effect of reducing the acoustic loss term is dramatic. The acoustic loss is decreased from 4.0, 2.0, 1.0, 0.5, and 0.2 times the measured loss coefficient, R_a. As R_a is decreased, the *TL* increases and the bandwidth decreases. For a fixed value of R_a this system will operate most effectively at the center frequency, ω/ω_n = 1, and less effectively above and below ω/ω_n = 1. It should be noted that R_a is determined by material properties and the geometry of the Helmholtz resonator. This analysis shows the SHR should be designed to minimize R_a to attenuate noise most effectively at a single frequency. If the unwanted noise has a wider bandwidth, an alternative objective might be to increase R_a to increase the absorption bandwidth, however this will come at the expense of reduced *TL* at the center frequency.

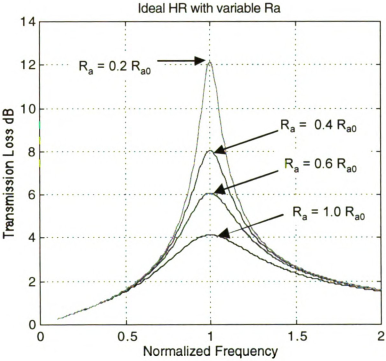

Figure 3.4. Transmission loss vs. normalized frequency with varying acoustic damping 0.2, 0.5, 2.0, and 4.0 * R_{a0}

The frequency dependence of the transmitted, reflected and absorbed power can also be computed using (3.12) – (3.14). The same parameters used in the previous result were used in Figure 3.5 showing the effect of reducing the acoustic loss term in the model. At $\omega_n = 1$ $\mathbf{P}_T/\mathbf{P}_I$ approaches 0, $\mathbf{P}_R/\mathbf{P}_I$ approaches 1 and $\mathbf{P}_A/\mathbf{P}_I$ approaches 0 as R_a is reduced.

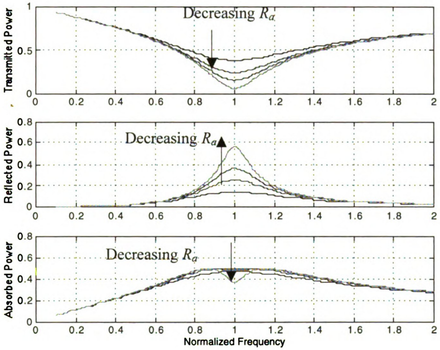

Figure 3.5. Plot of transmitted, reflected, and absorbed power ratios vs. frequency as acoustic loss term is reduced

The unique feature of the SHR is the ability to tune the bandwidth and center frequency of the *TL* by changing the gains K_P and K_I. The controller gains were selected to move the center frequency, ω_n while maintaining a constant peak, *TL* (Figure 3.6), by choosing the appropriate value of K_P and K_I (Table 3.1). The gains in Table 3.1 define the controller impedance, Q_2/P_2. The microphone sensitivity (S_{mic} = 0.05 volts/Pa) and actuator area ($S_d = 0.01$ m^2) are not included in the model. When these are included, the gains that must be implemented on the controller are increased by $1/(S_{mic} * S_d) = 2000$.

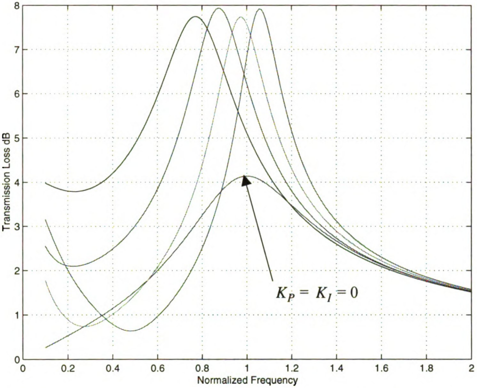

Figure 3.6. Transmission loss vs. normalized frequency for closed-loop SHR, placing resonance at 1.0, 1.1, 1.2, 1.3, and 1.4, showing that the center frequency and damping can be changed by varying K_P and K_I

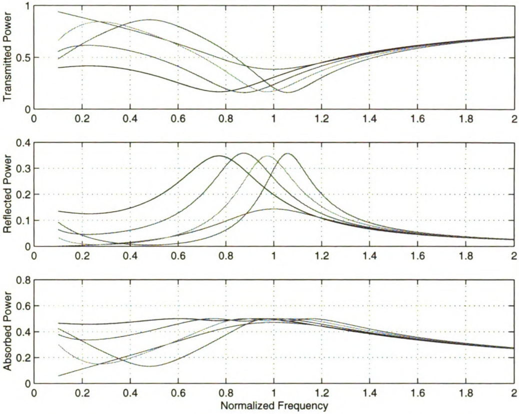

Figure 3.7. Transmitted, reflected, and absorbed power for gain settings used in Figure 3.6

Table 3.1. Controller gains K_P and K_I used to move the resonant peak to various frequencies, ω_n while maintaining constant peak *TL*

ω_n	K_P	K_I
1.00	0	0
0.78	1.5 e –6	-1.5 e –3
0.85	1.7 e –6	-0.5 e –3
0.97	2.1 e –6	0.5 e –3
1.05	2.6 e –6	1.5 e -3

Thus far, the analysis has been presented to explain the power flow in the acoustic duct and SHR system. The model was simplified by the anechoic duct termination assumption and results were presented to illustrate that the function of the SHR is to reflect sound, reducing the transmitted sound from propagating in the duct.

When the duct end is not perfectly anechoic, this analysis must be revised. An open duct end, for example, will reflect sound, resulting in two reflecting regions in the duct: one at the duct end and one at the SHR. The reflection coefficient upstream of the SHR can be computed from (3.10), but (3.11) through (3.15) require the anechoic duct assumption and are no longer valid. Therefore, the transmitted and absorbed power and transmission loss can not be determined from the reflection coefficient alone.

A more complex model could include more details of the duct to show the SHR reduces sound transmitted from the duct end. Nonetheless, this is beyond the scope of this paper. Furthermore, this would obscure the concept of the SHR acting to reflect sound in the duct and reduce the transmission of sound. However, it is necessary to analyze this scenario since the experimental tests used to verify the model employ an open duct end.

A duct open end can be modeled as a perfectly reflective boundary with $\Re$ (Hull and Radcliffe, 1991; Speakerman and Radcliffe, 1988; Seto, 1971; Levine and Schwinger, 1946) given by

$$\Re_D = e^{\left(\pi - \frac{l_e}{c}\omega\right)} \tag{3.24}$$

where l_e is twice the distance from the point of measurement to the duct end. This results in a reflection coefficient of -1 with a time delay from the wave propagating to the boundary and back. The duct end impedance can be computed by

$$Z_D = \frac{1+\mathfrak{R}_D}{1-\mathfrak{R}_D} \tag{3.25}$$

This expression is substituted into (3.9) for Z_T and the reflection coefficient upstream of the SHR, $\mathfrak{R}$ vs. frequency is plotted in Figure 3.8 with various controller gain settings. The interpretation of these results is difficult. Clearly, the dynamics that created a peak in the magnitude of $\mathfrak{R}$ in the anechoic duct termination model create a dip when the duct end is open. These results are compared with experimental results obtained in the next section to validate the model.

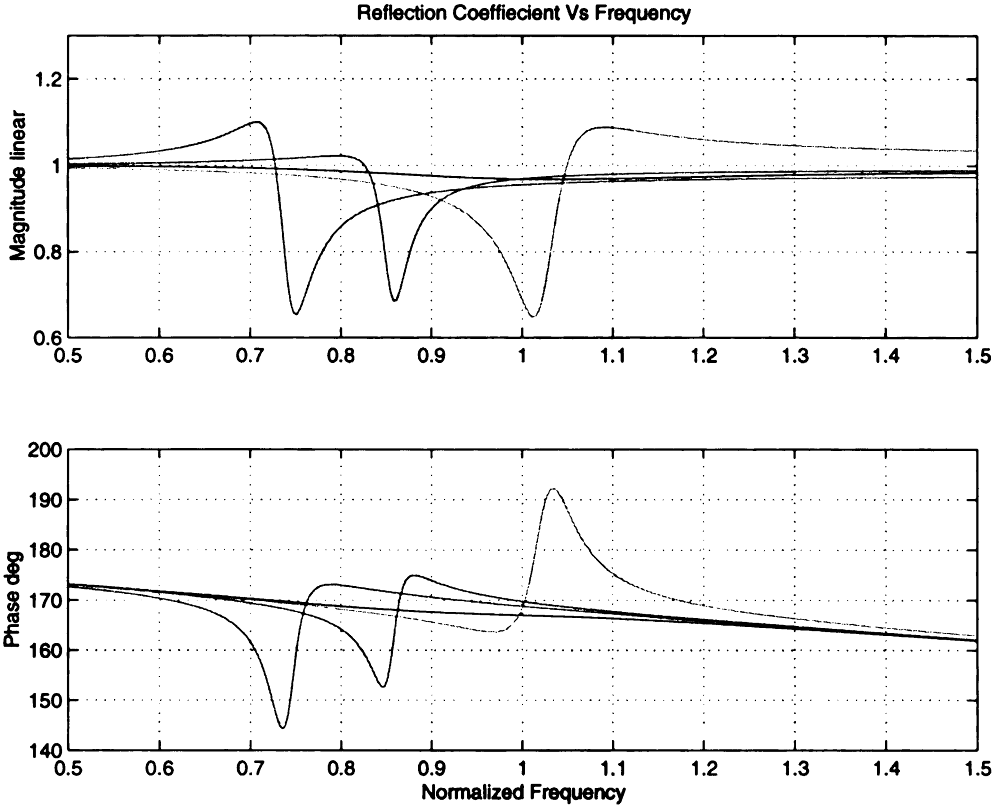

Figure 3.8. Plot of reflection coefficient vs. frequency for open end duct, 3 trials with various controller gains

EXPERIMENTAL VERIFICATION

An experimental apparatus (Figure 3.9) was constructed to verify the analytical model. The setup consisted of a 40 inch long and 3/4 inch diameter acoustic duct with a disturbance noise generating audio speaker at $x = 0$, a SHR at $x = 20$ inches, and the duct end at $x = 40$ inches left open. Two microphones, spaced a distance 0.0254 m apart were placed in the duct upstream of the SHR to measure the reflection coefficient $\Re$.

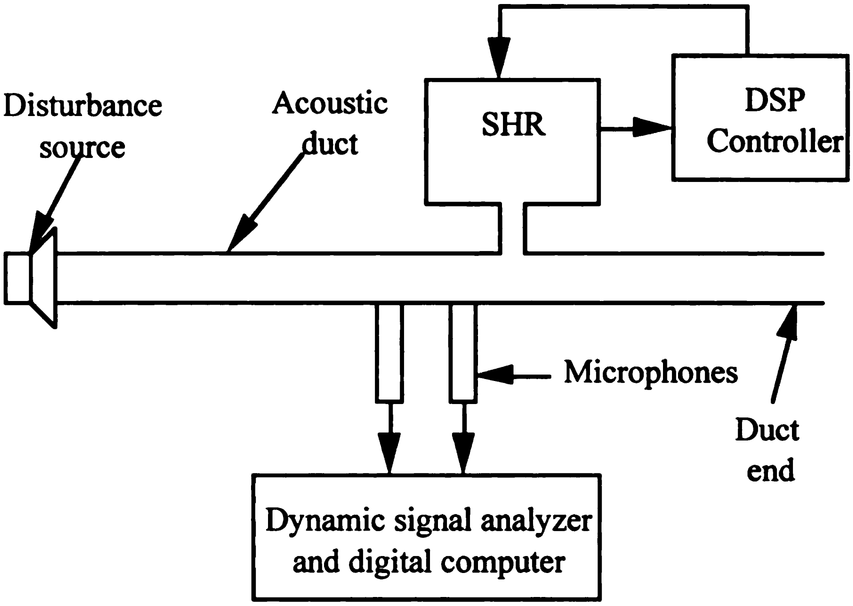

Figure 3.9. Schematic of experimental apparatus used to measure the reflection coefficient in the duct and SHR system

The experimental SHR setup, consisted of two components: a Helmholtz resonator cavity and a microphone-compensated actuator system. A cylindrical Helmholtz resonator cavity was constructed from PVC with dimensions 0.075 m in diameter and 0.15 m in length. A cylindrical neck with dimensions 0.018 m in diameter and 0.01 m in length was fitted on one face of the cavity. The microphone-compensated actuator system consisted of a half inch B&K type 4155 microphone sealed through the wall of the cavity, a D-Space Model #1102 floating point, digital signal processor (DSP) used to implement the controller, and a 6 inch dual voice coil speaker. The actuator was used in the uncompensated configuration (Chapter 4) because the compensated configuration introduced excessive noise which corrupted the experimental measurement of the reflection coefficient. A DSP sampling rate of 5 kHz was used for all experiments.

The reflection coefficient $\Re$, was measured using a transfer function technique for determining the acoustic characteristics of duct systems (ASTM Designation: E 1050 –90; Blaser and Chung, 1978; Chung and Blaser, 1980) The transfer function H_{12}, between the two pressure signals P_1 and P_2 was measured using a Hewlett Packard 35660A dynamic signal analyzer. This data was then used to compute $\Re$ as

$$\Re = \frac{H_{12} - H_{12r}}{H_{12l} - H_{12}} \tag{3.26}$$

where H_{12r} and H_{12l} are the transfer functions (pure time delays) associated with the right- and left-running pressure waves and can be expressed as

$$H_{12r} = e^{-iks} \tag{3.27}$$

$$H_{12l} = e^{+iks} \tag{3.28}$$

where s is the distance between the two microphones, and k is the wave number, (ω/c). White noise was injected into the duct by the disturbance speaker and H_{12} was measured using 100 time averages. A digital computer was then used to compute $\Re$ using (3.26), (3.27) and (3.28).

The first experiment examined the reflection coefficient of the open duct end. The SHR was removed from the duct and the two microphones were placed 1 and 2 inches from the open end. Figure 10 shows $\Re$ vs. frequency with the top graph showing linear magnitude, and the bottom showing phase in degrees. These results show that the reflection coefficient of the duct open end agrees well with (3.24). The magnitude is a constant = 1 and the phase increases with frequency at a rate that corresponds to the pure time delay between the microphone, the duct end and back. These results agree with the theory of Levine and Schwinger (1946).

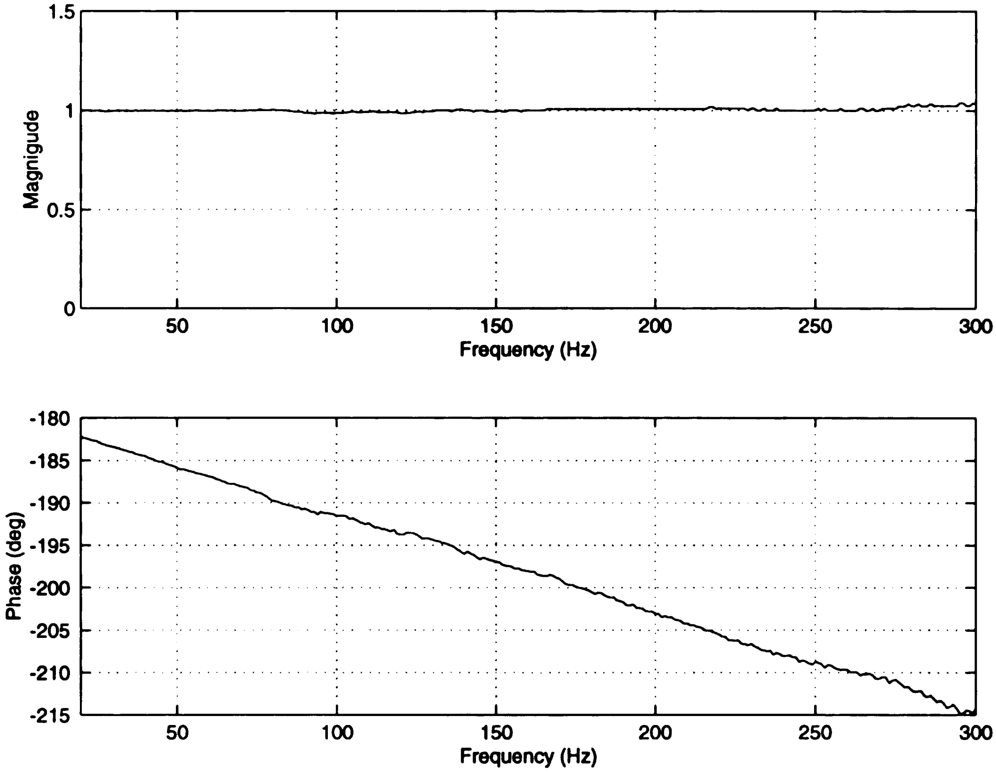

Figure 3.10. Reflection coefficient of open end duct with SHR removed showing the duct end can be modeled as a purely reflective boundary

Next the SHR was inserted in the duct at x = 20 inches, the controller was turned on and $\Re$ was measured for various controller settings. Graphs of $\Re$ with four different controller settings (Table 3.2) are shown in Figure 3.11. The top graph shows the magnitude of $\Re$ vs. frequency and the bottom shows phase vs. frequency. These results show additional dynamics superimposed over a response similar to Figure 3.10, i.e., the SHR adds to the reflection in a narrow frequency band in addition to the reflection of the open end duct. For example, in Figure 3.11.D a dip in the magnitude and a decrease then increase in phase is observed around 240 Hz. The frequency at which this dip occurs changes for each controller setting, demonstrating the ability of the SHR to tune the system and move the frequency of the maximum reflection. The overall trends of the graphs in Figure 3.11 agree with the theoretical graphs of Figure 3.8 verifying that the model agrees with the experimental results. It should be noted that the controller gains for the theory and experiment are not equivalent. This is not surprising since the theory models the actuator as a pure gain with no dynamics and the actuator used in the experiment exhibits significant dynamics. In this article, the controller and actuator models are kept simple intentionally, to focus the attention on the acoustics of the system. A thorough examination of the controller and actuator dynamics is given in Chapter 5.

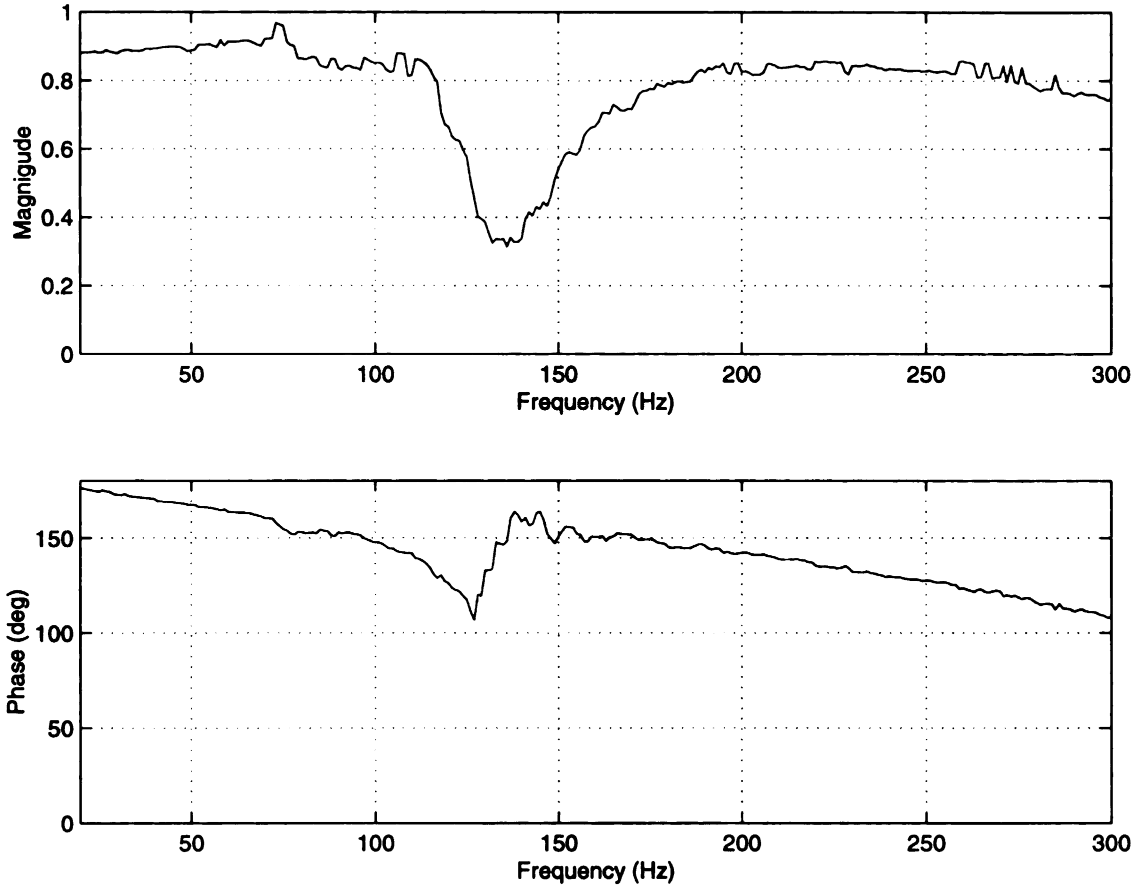

Figure 3.11.A. Experimental plot of the reflection coefficient upstream of the SHR with the controller in closed-loop to change the frequency of the reflection added to the duct by the device R_l at 150 Hz

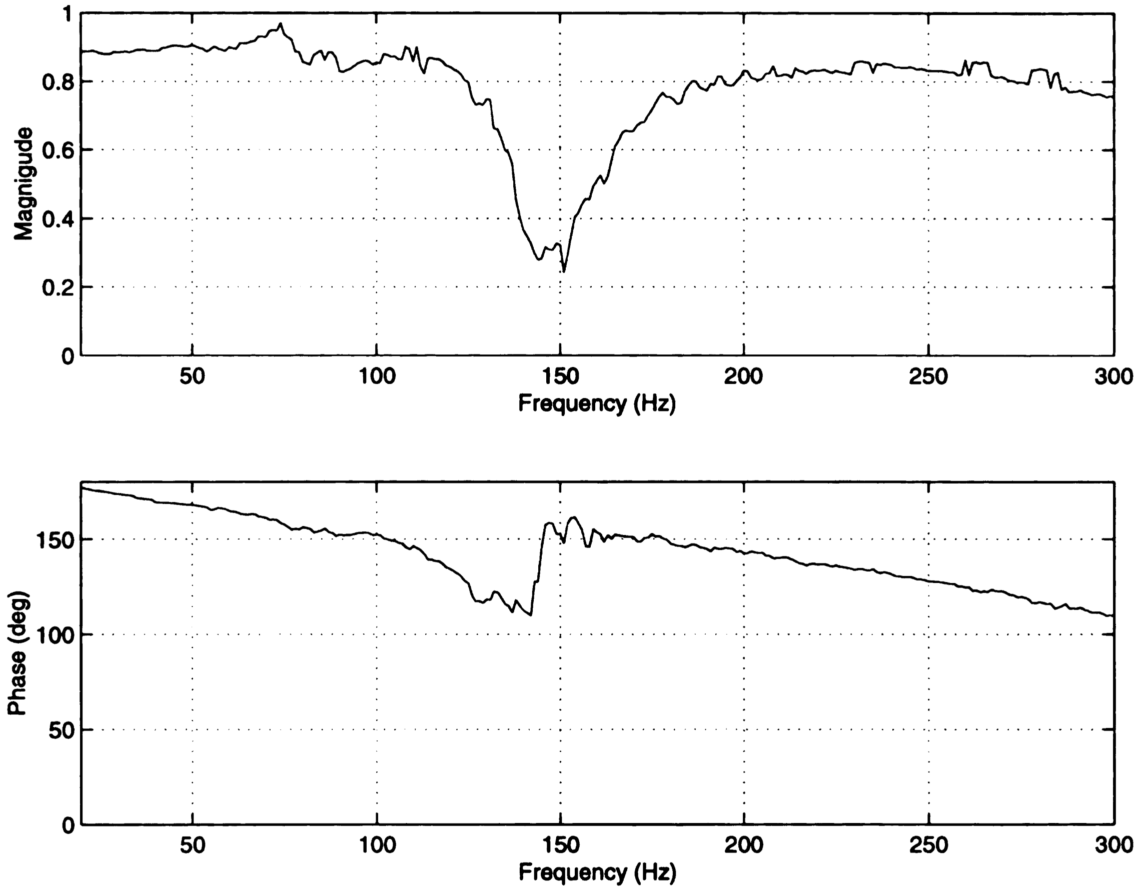

Figure 3.11.B. Experimental plot of the reflection coefficient upstream of the SHR with the controller in closed-loop to change the frequency of the reflection added to the duct by the device R_l at 165 Hz

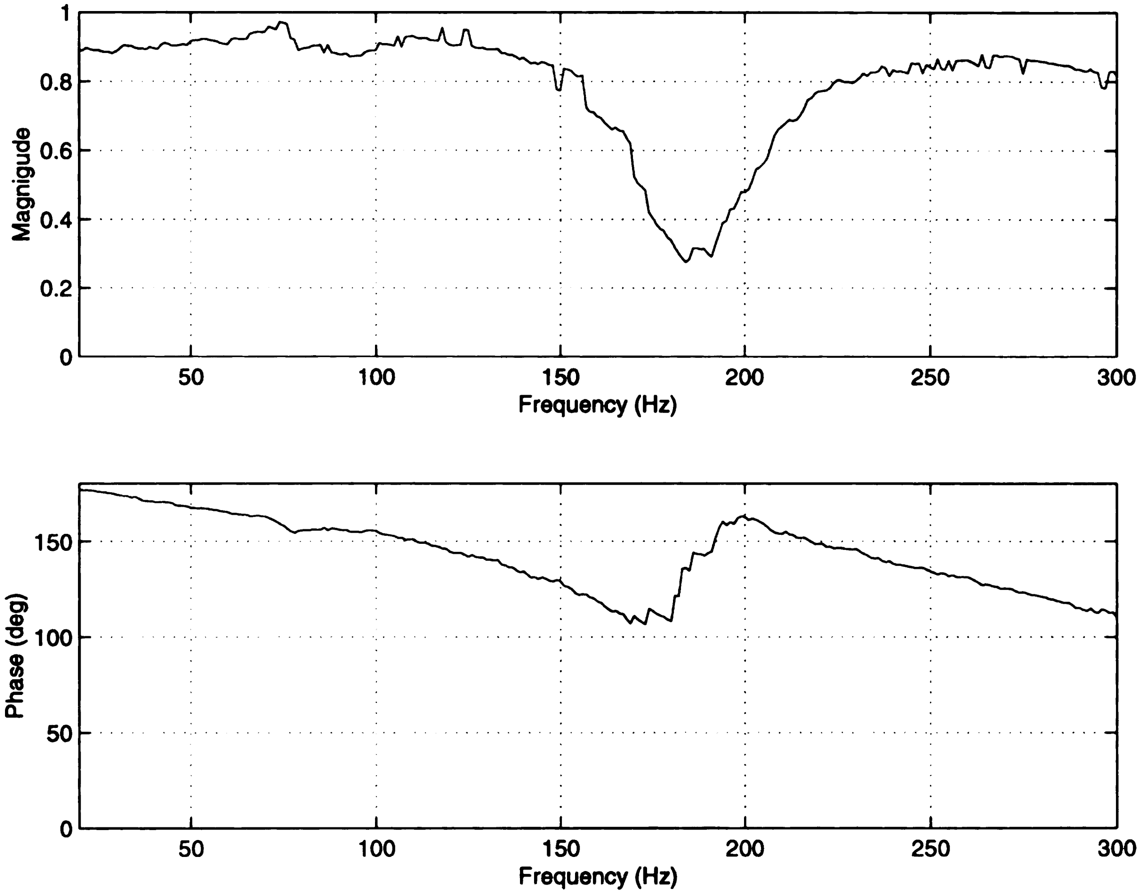

Figure 3.11.C. Experimental plot of the reflection coefficient upstream of the SHR with the controller in closed-loop to change the frequency of the reflection added to the duct by the device R_l at 210 Hz

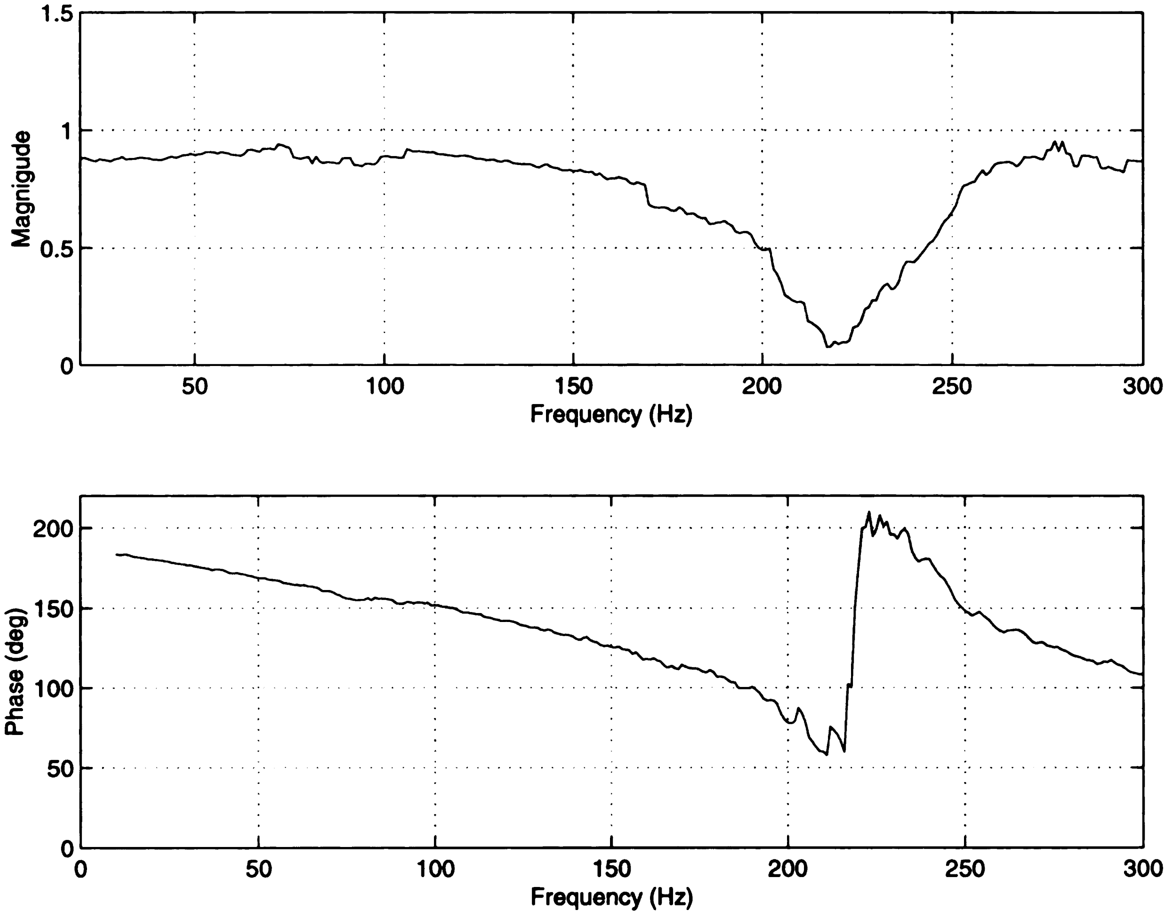

Figure 3.11.D. Experimental plot of the reflection coefficient upstream of the SHR with the controller in closed-loop to change the frequency of the reflection added to the duct by the device R_l at 240 Hz

Table 3.2 Controller gains used to generate Figure 3.11

Figure	Min | T | Frequency (Hz)	K_P	K_I
11.A	150	2245	-1.0
11.B	165	2430	-0.3
11.C	210	1220	1.0
11.D	240	2520	2.5

While the relation for the transmission coefficient (3.15) does not strictly hold for the reflective duct end, it is instructive to consider the transmission coefficient for these results. Figure 3.12 shows a plot of the magnitude of T, computed from $T = 1 + \Re$, where $\Re$ is defined by the data in Figure 3.11.D. The minimum $|T|$ occurs at 240 Hz.

Note that this does not correspond to the frequency of the minimum in $|\Re|$; both the magnitude and phase of $\Re$ must be considered to determine the minimum $|T|$.

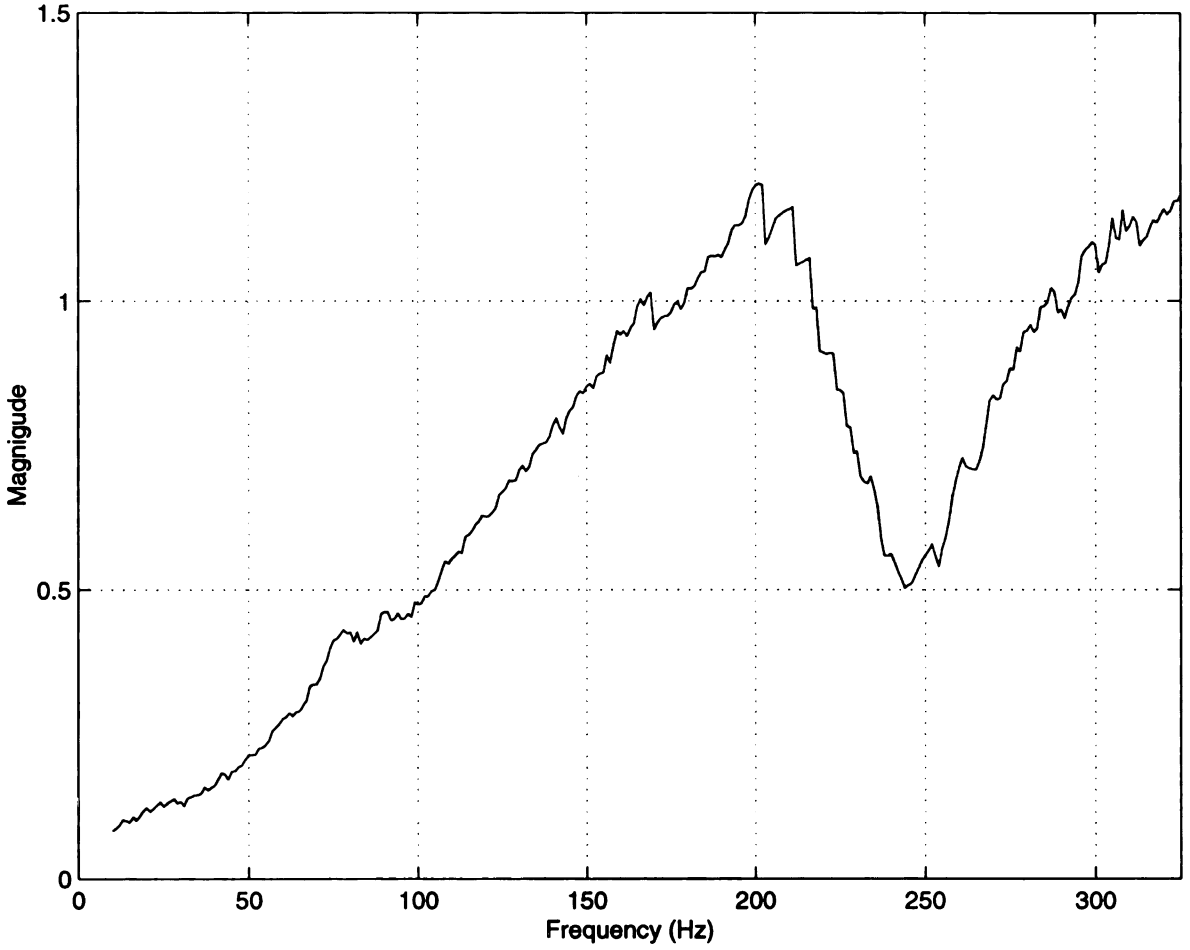

Figure 3.12. Plot of transmission coefficient for data in Figure 3.11.D

Another view of the relationship between $\Re$ and T is made by plotting a parametric polar plot of $\Re$ vs. frequency (Figure 3.13). At low frequencies, $\Re$ is real and equal to -1. As frequency increases the angle increases. However, near 240 Hz a loop occurs and $\Re$ approaches a negative real number indicating more reflection. At each point on the graph a vector can be drawn to represent $\Re(\omega)$, and an associated vector $T(\omega)$ by subtracting $1-\Re(\omega)$. A vector diagram (Figure 3.12) locates the magnitude (and frequency) for the minimum $|T|$. For this experiment the minimum $|T|$ was 0.45 and the associated $\Re$ was 0.6 which occurred at 240 Hz. Similar analysis of the other data in Figure 3.11 results in the minimum $|T|$ located at 150, 165, 210 and 240 Hz for the four different controller settings.

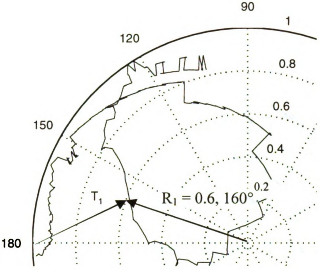

Figure 3.13. Parametric polar plot of reflection coefficient magnitude and phase vs. frequency with controller turned on showing vectors for minimum transmission coefficient, T and associated $\Re$

An additional experiment was performed to demonstrate the application of the SHR in an acoustic duct system (ASTM Designation: E 477 –96). The SHR was connected to a 3/4 inch diameter, 20 inch long duct (Figure 3.14). A separate audio speaker was mounted on one end of the duct to inject noise and the other end was left open. A pure tone of 185 Hz frequency was injected into the duct and the sound level P_3 was measured near the duct end with a 1/2 inch B&K microphone. The gains K_P and K_I were set to tune the SHR to 185 Hz and the time response of the microphone signal was recorded as the controller was activated. Figure 3.15 shows P_3 vs. time in open-loop for 0.055 seconds; then the controller was activated. There was a short transient then the P_3 signal was reduced by a factor of approximately 3 (10 dB). Similar results were obtained with disturbance tones with frequencies ranging from 180 to 300 Hz. This demonstrates the ability of the device to create a reflective region in the duct, which increases the reflected power and reduces the transmitted power.

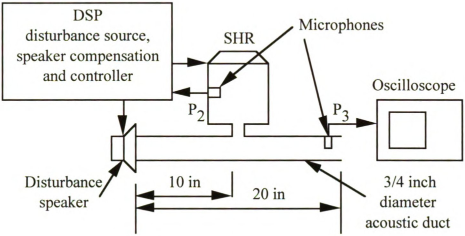

Figure 3.14. Schematic of SHR applied to acoustic duct

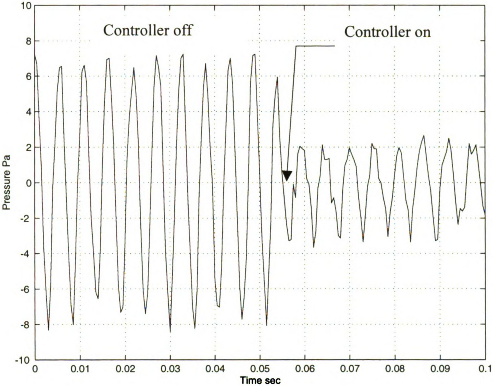

Figure 3.15. Time response of pressure at duct end with pure tone disturbance as controller is activated showing 10 dB noise reduction

CONCLUSIONS

In this article a controllable resonator was presented which can be tuned to move the resonant frequency and change the damping characteristics via a closed-loop controller. It was shown that by attaching the resonator as a side branch in a duct, the resonator impedance creates a narrow frequency band pressure release region in the duct. This increases the sound reflection and reduces the sound transmission through the duct when the resonator is tuned to match a disturbance noise with a narrow band frequency. Although the duct was modeled with an open end to compare the experimental and model results, the conclusions are valid regardless of the duct termination. It was shown that the optimum resonator impedance to reflect sound is a large, positive real impedance. Theoretically, an infinite impedance will result in all of the incident sound reflected and none transmitted. Experimental measurements of the reflection coefficient in a duct were made with the closed-loop control system and compared with theory. Finally, experimental results demonstrated that the closed-loop resonator provided as much as 10 dB of noise reduction to a disturbance tone in a duct.

Chapter 4

A Comparison of Acoustic Actuators for the Semi-Active Helmholtz Resonator

This paper examines the implementation of an acoustic actuator in a tunable semi-active Helmholtz resonator (SHR). The advantages and limitations of a compensated speaker are studied and compared with an uncompensated speaker. It is shown that the speaker compensator reduces the effects of internal dynamics and boosts the actuator control authority but inadvertently introduces noise into the system. Alternatively, the uncompensated speaker has weaker control authority, but does not introduce noise into the system. These results suggest that both compensated and uncompensated actuators can be useful for different applications.

The semi-active Helmholtz resonator (Temkin, 1981) is an acoustic device with behavior that can be used to selectively quiet narrow band noise in acoustic systems. It consists of a static Helmholtz resonator with a sensor, controller, and actuator added to the interior of the resonator cavity (Figure 4.1). The nominal resonant frequency and damping of the device was determined by the dimensions of the resonator neck and cavity but can be modified by the closed loop feedback system. When driven by a pressure from a primary acoustic system, such as an acoustic duct, the resonator responds with a large magnitude volume velocity through the resonator neck which is in phase with the pressure. This creates a "pressure release" boundary condition, which inverts and reflects the incident pressure wave back up the duct, thus reducing the transmitted pressure wave and reducing the transmitted sound (Pierce, 1981).

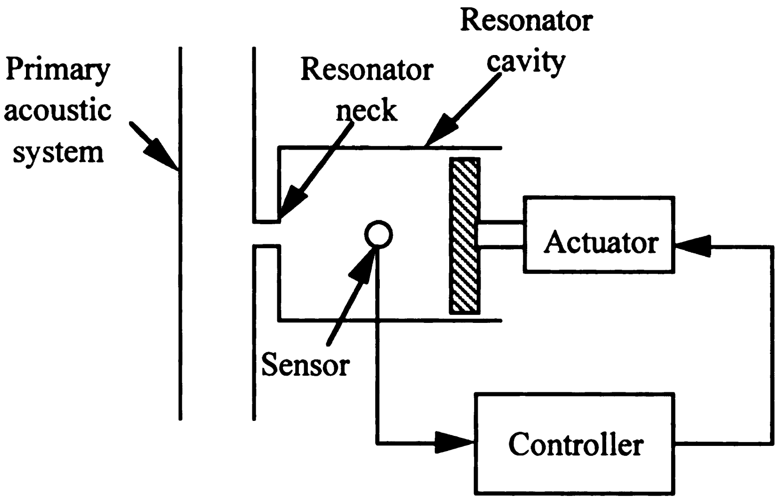

Figure 4.1. Schematic of a semi-active Helmholtz resonator connected to a primary acoustic system

The actuator is a critical component in the implementation of the SHR, and strongly affects the closed-loop performance of the system. Internal actuator dynamics will affect the closed-loop response of the system since the actuator and acoustic resonator become tightly coupled by the pressure interaction between the two systems. Electromechanical audio speakers are often used for acoustic actuators because of their low cost and commercial availability. However, audio speakers are not ideal actuators. They typically have a resonance frequency between 50-150 Hz (for bass speakers) resulting in large magnitude and phase variation in their operating frequency range. Furthermore, the speaker velocity response is strongly affected by the pressure interaction with the acoustic system. A resonance in the acoustic system will impede the speaker velocity, resulting in weak control authority.

The closed-loop feedback control design for the SHR is also affected by the actuator performance. A simple proportional-integral (PI) controller is used in the SHR, and an analytical solution can be found that maps the controller gains to the acoustic resonant frequency and damping ratio (Chapter 2). However this assumes that the actuator has no dynamics, and the transfer function is a pure gain. Actuator dynamics complicate this mapping, resulting in the need of a higher order controller.

This sensitivity of the system response and the desire to avoid using a higher order controller motivates the use of local feedback compensation of the actuator. This technique adds a local feedback loop to the actuator (Figure 4.2), which drives the actuator output to the input voltage making the response approach a pure gain of one, as the loop gain is increased. The goal of the compensator is to boost the control authority. It also simplifies the controller design, since actuator response approaches the ideal response. Compensation for audio speakers has been proposed in many forms (Harwood, 1974; Klaassen and de Koning, 1968; Holdaway, 1963; Tanner, 1951). Birdsong and Radcliffe (1999) proposed a technique using a dual voice coil speaker with local feedback compensation that resulted in a compensated acoustic actuator with minimal magnitude and phase error below 400 Hz. This design compensated the internal speaker dynamics and the pressure interaction with the acoustic system. The compensated acoustic actuator was chosen as the actuator for the SHR because of these strengths.

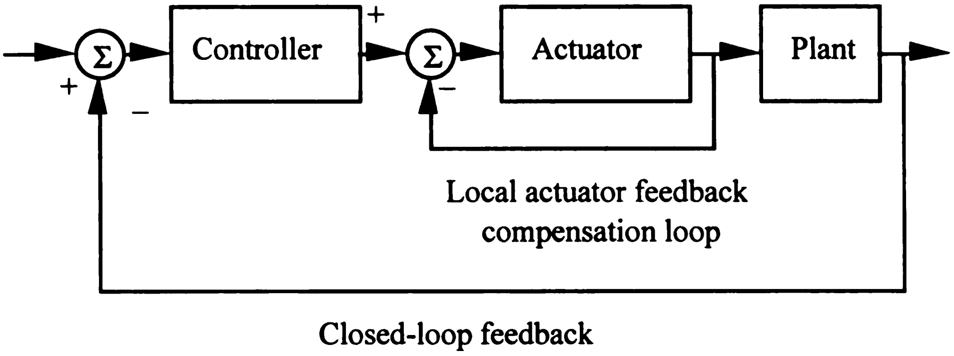

Figure 4.2. Local actuator feedback compensation used to boost actuator authority, minimize actuator dynamics, and simplify controller design

This paper discusses three major topics: analytical model development, coupled system simulations, and experimental results. In the first section, separate analytical models for each component are presented, including the acoustic resonator, controller, speaker, and compensator. In the second section, the models are coupled and various configurations are examined. First, the closed-loop resonator model with an ideal actuator is presented. Then, the ideal actuator is replaced by the uncompensated speaker model. Next, the speaker compensator is added, and the compensated speaker model is applied to the closed-loop control system model. Finally the uncompensated speaker model is applied to the closed-loop control system demonstrating the advantages and disadvantages of the compensation technique. The last section presents experimental results which are compared with the analytical model and which demonstrate the effectiveness of the actuator implementation in the SHR.

ANALYTICAL MODEL DEVELOPMENT

The closed-loop compensated SHR consists of several interconnected components: an acoustic resonator, a feedback controller, an audio speaker, and a compensator. Analytical models for each have been developed in other works, and will be presented here briefly. The reader is referred to the references for complete descriptions of the components. These component models will be assembled into coupled system models in the next section.

Resonator

The central component of the SHR is a Helmholtz resonator with one surface of the cavity replaced by a moving surface (Figure 4.3). The system can be represented by linear time invariant state equations (Chapter 2)

$$\begin{bmatrix} \dot{Q}_1 \\ \dot{V} \end{bmatrix} = \begin{bmatrix} \frac{-R_a}{I_a} & \frac{-1}{I_a C_a} \\ 1 & 0 \end{bmatrix} \begin{bmatrix} Q_1 \\ V \end{bmatrix} + \begin{bmatrix} \frac{1}{I_a} & 0 \\ 0 & 1 \end{bmatrix} \begin{bmatrix} P_1 \\ Q_2 \end{bmatrix} \tag{4.1}$$

$$\begin{bmatrix} Q_1 \\ P_2 \end{bmatrix} = \begin{bmatrix} 1 & 0 \\ 0 & \frac{1}{C_a} \end{bmatrix} \begin{bmatrix} Q_1 \\ V \end{bmatrix} \tag{4.2}$$

where the states are Q_1, the volumetric flow rate or "volume velocity" from the neck (m^3/s) and V, the sum of the volumes introduced through the neck and the inner surface of the cavity (m^3). The inputs are P_1, the pressure at the neck inlet to the cavity (N/m^2), and Q_2, the volume velocity from the movable surface in the cavity (m^3/s). The outputs are Q_1 and P_2, the pressure in the cavity (N/m^2). The other parameters are R_a, the acoustic loss that represents viscous and radiation losses (Ns/m^5), I_a, the acoustic inertia of the mass of air in the resonator neck (Ns^2/m^5), and C_a, the acoustic compliance of the cushion of air in the resonator cavity (m^5/N).

With the movable surface held fixed, the system is a second order oscillator (Temkin, 1981) with resonant frequency and damping given by

$$\omega_n = \sqrt{1/C_a I_a} \tag{4.3}$$

$$\zeta = \frac{R_a}{2}\sqrt{\frac{C_a}{I_a}} \tag{4.4}$$

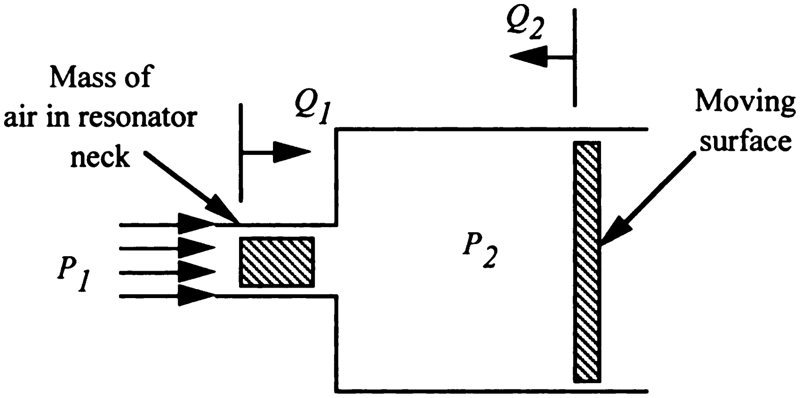

Figure 4.3. Schematic diagram of SHR showing inertia effect in neck and the movable surface in the cavity interior

Controller

A proportional-integral controller can be used to generate an acoustic impedance between Q_2 and P_2, on the moving inner surface of the SHR cavity. This creates a closed-loop, positive feedback configuration (Figure 4.4).

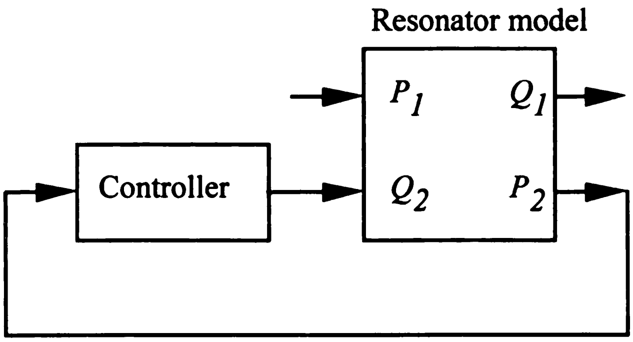

Figure 4.4. Closed-loop positive feedback SHR system block diagram with disturbance through P_1

A PI controller can be modeled by the transfer function,

$$G(s) = \frac{Q_2}{P_2} = K_P + \frac{K_I}{s} \tag{4.5}$$

where K_P, and K_I are the proportional and integral gains respectively.

Speaker

The actuator is modeled as a dual voice coil speaker (Figure 4.5). The dual voice coil speaker has certain characteristics that make it ideal for use as an acoustic actuator. It has 2 independent wire coils intertwined and wrapped around a bobbin which is allowed to slide over a permanent magnet. The state equations for a dual voice coil speaker can be represented by the linear time invariant state equations (Radcliffe and Gogate, 1996; Birdsong and Radcliffe, 1999)

$$\frac{d}{dt}\begin{bmatrix} Q_2 \\ q_2 \\ \lambda \end{bmatrix} = \begin{bmatrix} \frac{-R_s}{I_s} & \frac{-1}{C_s I_s} & \frac{blS_d}{I_c I_s} \\ 1 & 0 & 0 \\ \frac{-bl}{S_d} & 0 & \frac{-R_m - R_c}{I_c} \end{bmatrix} \begin{bmatrix} Q_2 \\ q_2 \\ \lambda \end{bmatrix} + \begin{bmatrix} 0 & 0 \\ 0 & \frac{-S_d}{I_s} \\ 1 & 0 \end{bmatrix} \begin{bmatrix} e_p \\ P_2 \end{bmatrix} \tag{4.6}$$

where the states are the volume velocity and volume displacement from the speaker Q_2, and q_2, and the electromagnetic flux in the speaker coil λ. The inputs are the primary coil voltage, e_p, and pressure on the speaker face, P_2. The output equation is given by

$$\begin{bmatrix} e_{bs} \\ i_p \\ Q_2 \end{bmatrix} = \begin{bmatrix} bl\left(1 - \frac{M_c}{I_c}\right) & 0 & \frac{-M_c}{I_c^{\,2}}(R_c + R_m) \\ 0 & 0 & \frac{1}{I_c} \\ 1 & 0 & 0 \end{bmatrix} \begin{bmatrix} Q_2 \\ q_2 \\ \lambda \end{bmatrix} + \begin{bmatrix} \frac{M_c}{I_c} & 0 \\ 0 & 0 \\ 0 & 0 \end{bmatrix} \begin{bmatrix} e_p \\ P_2 \end{bmatrix} \tag{4.7}$$

where the outputs are the voltage in the secondary coil, e_{bs}, the current in the primary coil, i_p, and Q_2. The parameters in (4.6) and (4.7) are the speaker face area, S_d, speaker inertia, I_s, speaker compliance, C_s, speaker friction, R_s, speaker coil resistance, R_c, speaker coil inductance, l_c, speaker coil mutual inductance, M_c, speaker electromechanical coupling factor, *bl*, and the primary coil current sensing resistance, R_m.

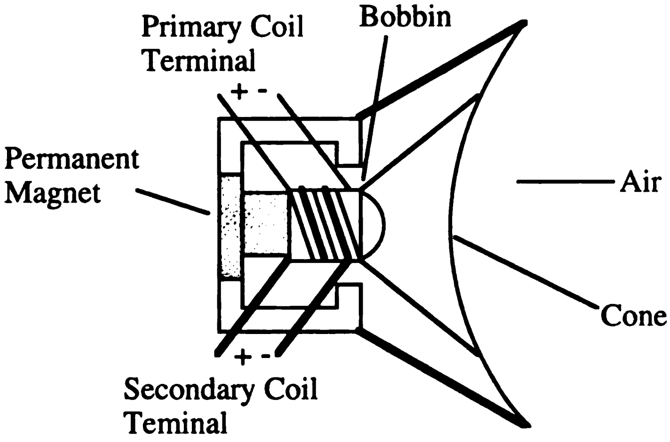

Figure 4.5. Dual voice-coil speaker diagram

Compensator

The velocity frequency response of the speaker can be improved with local feedback compensation. The volume velocity of the speaker, Q_2, is strongly affected by the dynamics of the speaker and the pressure input, P_2. These effects will combine to create magnitude and phase variations in the primary coil voltage to speaker velocity response, Q_2/e_p. One method of reducing these unwanted effects is to apply a proportional feedback controller (Figure 4.6) resulting in the closed system,

$$T_{spkr}(s)=\frac{V_{spkr}(s)}{V_d(s)}=\frac{K_{amp}G_{spkr}(s)}{1+K_{amp}G_{spkr}(s)H(s)} \tag{4.8}$$

where V_{spkr} is the speaker velocity, V_d is the desired velocity, G_{spkr} is the transfer function that relates the input voltage to speaker velocity, K_{amp} is an amplifier gain, and *H(s)* is a velocity sensor. If the sensor transfer function is a real constant, *k*, over the controller bandwidth, then the closed loop transfer function, $T_{spkr}(s)$, will approach a constant, $1/k$ with zero phase. This compensation forces the speaker cone velocity v_{spkr} to accurately follow the desired velocity input. The speaker volume velocity, Q_2, is equal to the speaker area, S_d, multiplied by the speaker velocity, v_{spkr}. The result is independent of the speaker dynamics and the input pressure provided that the sensor has a constant transfer function over the controller bandwidth.

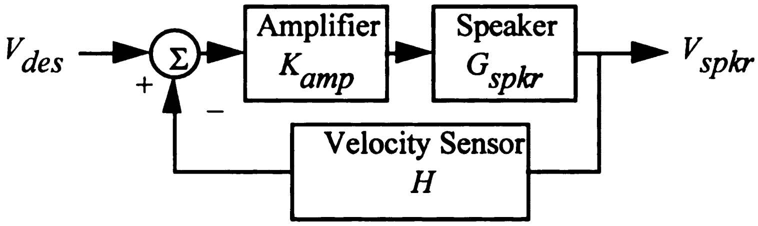

Figure 4.6. Block diagram of speaker and compensator

As K_{amp} is increased, the transfer function approaches $1/H(s)$ and the magnitude and phase variation approach zero This approach requires that the velocity of the speaker face be measured. A speaker velocity sensor is therefore needed which accurately predicts the speaker velocity in the presence of speaker and plant dynamics.

The relation between the speaker velocity and the two other measurable outputs (the secondary coil voltage, e_{bs}, and the primary coil current, i_p) can be computed from (4.6) and (4.7) in terms of e_{bs} and i_p yielding

$$v_{spkr}(s) = H_{bs} e_{bs}(s) - H_p(s) i_p(s) \tag{4.9}$$

where $H_{bs} = 1/bl$ and $H_p(s) = sM_c/bl$.

The secondary coil voltage, e_{bs}, can be measured directly from the speaker coil. The primary coil current, i_p, can be determined from the voltage across a resistor, R_m, placed in series with the primary coil, while H_{bs} is a pure gain ($1/bl$). The mathematically improper, differentiating transfer function, H_p, cannot be strictly realized exactly, but an approximation

$$\hat{H}_p(s) = \frac{M_c}{bl}\left(\frac{p_1 s}{s + p_1}\right) \tag{4.10}$$

can be used, where p_1 is a pole location selected such that $\hat{H}_p(s)$ approximates $H_p(s)$ over the controller bandwidth. Feedback compensation can now be implemented using the signal from the velocity sensor to compute the error between the desired velocity and the sensor velocity and a proportional controller to drive the speaker velocity to the desired velocity.

COUPLED SYSTEM SIMULATION

Assembly of the component models allows the investigation of the coupled system dynamics using numerical simulation. The simulation was performed using Matlab and Simulink software on a digital computer. This software allows state space and transfer function models to be interconnected in a single model to compute coupled system, frequency response graphs. The numerical values for the acoustic resonator and speaker parameters used in the simulation are given in Table 4.1. These values were measured from the physical devices used in the experimental results section and have been shown to be accurate (Birdsong and Radcliffe, 1999). The speaker was a 6 inch dual voice coil speaker and the resonator cavity was constructed from PVC pipe fittings with dimensions given in Table 4.1

Table 4.1. SHR Model Parameter Values

bl	2.45 N/A	R_c	5.7 ohm
c_o	343 m/s	R_m	10 ohm
C_s	0.000260 m/N	R_s	3.745 N sec/m
I_c	0.002 H	S	0.000254 m^2
I_s	0.0076 Kg	S_d	0.0133 m^2
l_e	0.010 m	V	0.002 m^3
M_c	0.001 H	ρ_o	1.18 Kg/m^3
S_{mic}	4 mv/ P_A		

Resonator and Controller with Ideal Actuator

The first coupled system model that will be considered is the acoustic resonator with a closed-loop feedback controller and an ideal actuator (Figure 4.7). This is a simple model which assumes that the actuator is ideal, i.e., it has a transfer function that is a pure gain of one. The cavity pressure, P_2, is fed to the controller and the controller output is fed into the resonator cavity volume velocity input, Q_2. The system can either be disturbed by the input, P_1, or by the disturbance signal, D_l, which is also added to the controller output.

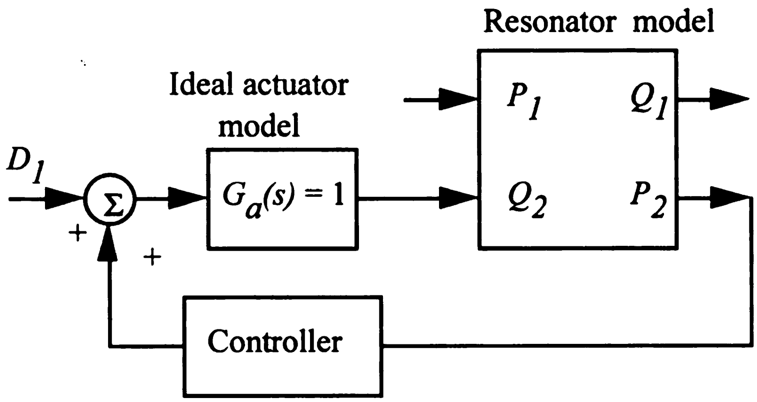

Figure 4.7. Block diagram of simple coupled system model including acoustic resonator, closed-loop feedback controller, and ideal actuator model

The eigenstructure of the system can be modified with the positive feedback controller. With the controller gains set to zero (open-loop), the system resonates at the nominal resonant frequency and damping (4.3) and (4.4). The numeric values for the resonator model nominal, resonant frequency and damping are f_n = 205 Hz and ζ = 0.025. By varying the controller gains K_P and K_I, the resonant frequency and damping can be varied. Figure 4.8 shows the P_1/Q_1 transfer function for this model for various values of K_P and K_I (Table 4.2).

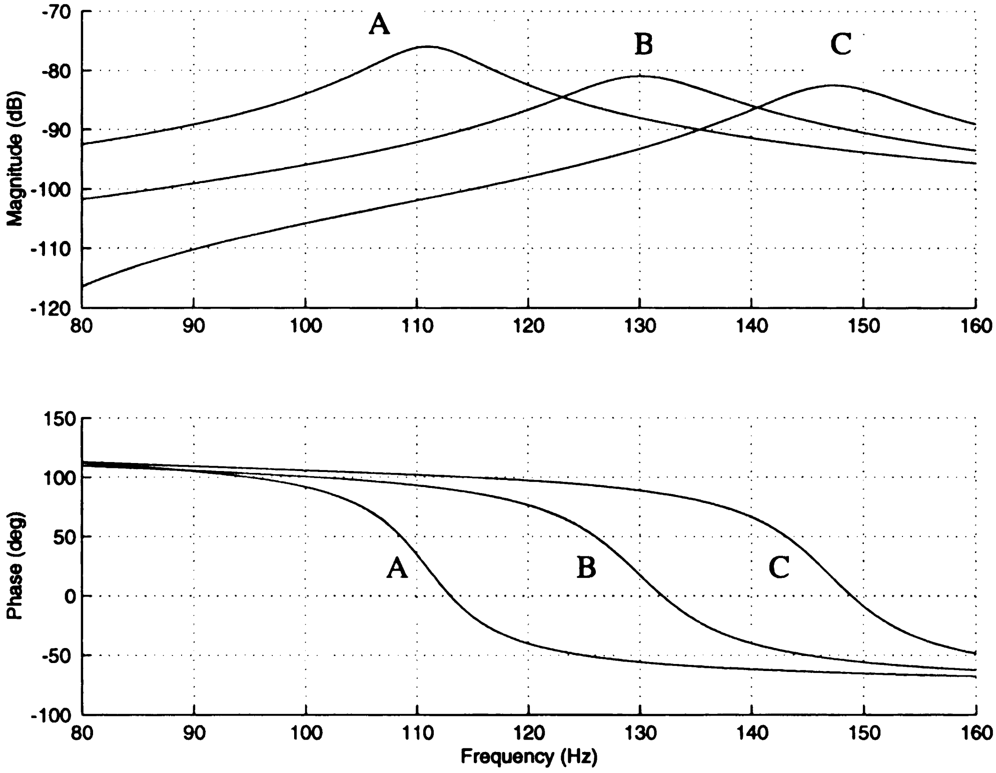

Figure 4.8. Frequency response simulation of resonator and closed-loop feedback controller with ideal actuator showing that the resonant frequency and damping can be changed by varying the controller gains

Table 4.2. Controller gains used to create Figure 4.8

Graph	K_P Gain	K_I Gain	Resonant Frequency (Hz)	Percent Damping
A	0.99	-100	112	10
B	0.99	0	130	10
C	0.99	100	145	10

The feedback controller makes the system response appear identical to the response of three different passive Helmholtz resonators with different tuned frequencies. In each curve the magnitude attains a maximum at the same frequency that the phase crosses zero. This is identical to the response of a passive resonator. The important feature here is that the change in frequencies was created by electronic tuning, not by changing the physical dimensions of the resonator.

This system, with the ideal actuator model, can be used to compute an analytical solution that maps the PI controller gains, K_I and K_P, to the closed-loop frequency response values of ω_n and ζ. This is the basis for an adaptive control algorithm that changes the gains on line to tune the system to track a disturbance signal with slow time varying frequency (Chapter 5). However, without the ideal actuator assumption, this mapping is not valid, and a different, more complicated controller design is required.

Resonator and Speaker

The ideal actuator will be replaced by the dual voice coil speaker model and the coupled system will be simulated with the controller removed. The speaker must provide a controlled Q_2 to the resonator for the response to be similar to the previous model. Figure 4.9 shows the speaker model coupled with the resonator model. The speaker output, Q_2, is connected to the resonator input, and the resonator output, P_2, is connected to the speaker input. The speaker is driven by a voltage applied to the primary coil, and the secondary coil is left in open circuit.

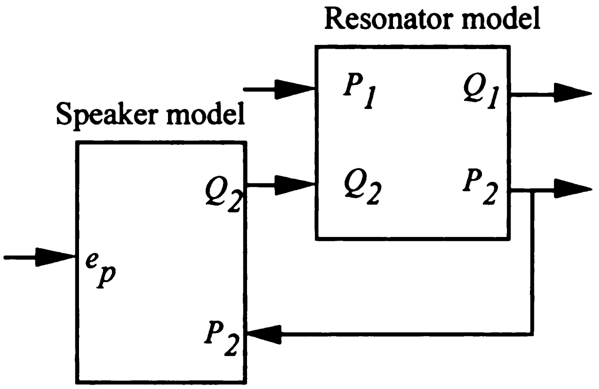

Figure 4.9. Block diagram of resonator and speaker models showing coupling through Q_2 and P_2

The frequency response of the output, Q_2, to input, e_p, reveals that the speaker does not behave as an ideal actuator with pure gain of one. The open-loop frequency response of the Q_2/e_p transfer function was simulated (Figure 4.10). The response shows two resonance peaks, one at 80 Hz and one at 290 Hz. There is 20 dB of magnitude variation and 180 degrees of phase variation between 50 and 300 Hz. Clearly, the speaker does not respond as an ideal actuator. This motivates the application of the local feedback compensation.

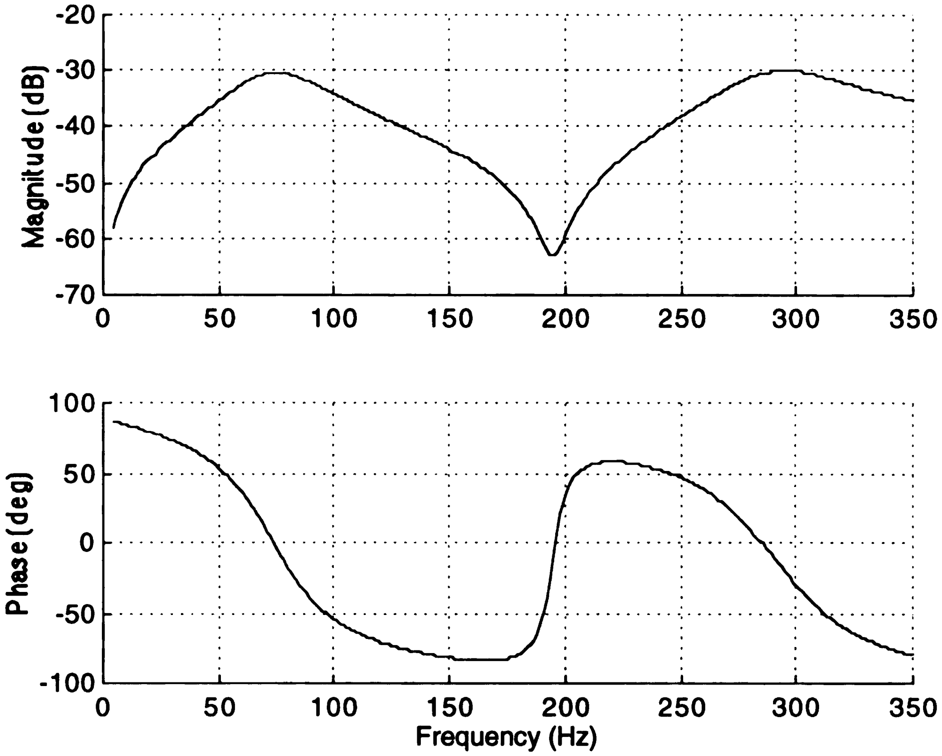

Figure 4.10. Frequency response simulation of the Q_2/e_p transfer function for the resonator and speaker model with the controller removed

Resonator, Speaker, and Compensator

A local feedback compensator model is added to the speaker model (Figure 4.11) to improve Q_2/e_p response. The velocity estimator generates a signal, v_{est}, which is subtracted from the input D_l. The error is then amplified by a proportional gain, K_{amp}, and the resulting signal becomes the input to the speaker, e_p. The local feedback compensation closes the loop around the speaker velocity, driving the actual velocity to the desired velocity. The compensated speaker model can be represented in subsequent models with a single block with inputs, D_l, and P_2, and output, Q_2, as indicated by the dashed box.

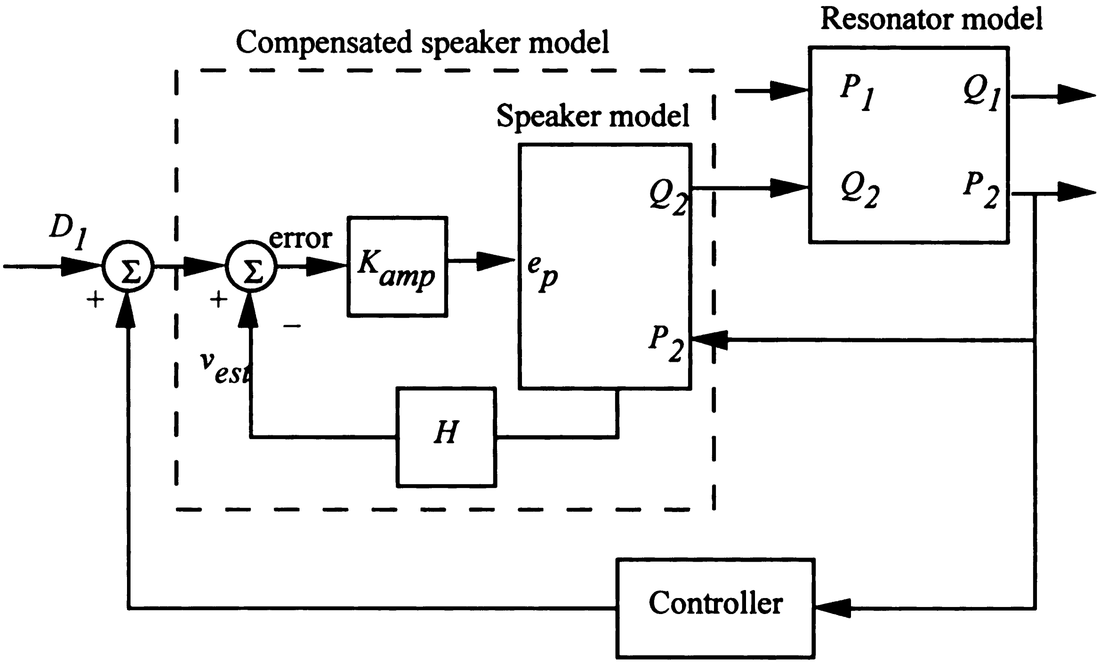

Figure 4.11. Block diagram of resonator and speaker with local feedback compensation, and controller removed

The compensator improves the low frequency response somewhat, but degrades the high frequency response. The effect of the compensator on the speaker can be illustrated by examining the frequency response of the Q_2/D_l transfer function. Figure 4.12 shows the response with K_{amp} = 30, 50, 100, and 200. As K_{amp} is increased, the low frequency response is improved. The magnitude and phase variation is reduced from 15 dB and 125 degrees between 20 and 100 Hz without the compensation (Figure 4.10) to 7 dB and 70 degrees with the compensation and K_{amp} = 200 (Figure 4.12). However, above 100 Hz the response is worse than with the uncompensated actuator. The compensator adds phase above 100 Hz increasing the maximum phase from 75 degrees at 150 Hz for the uncompensated actuator to 150 degrees for the compensated actuator with K_{amp} = 200. The compensator is not effective in driving the speaker velocity to the desired velocity at the acoustic resonant frequency (205 Hz). The increases in K_{amp} have only marginal effect at increasing the magnitude at 205 Hz.

These results indicate that the compensator does not provide adequate speaker performance to make the speaker model approach the ideal actuator model. This does not imply that the actuator is not useful in the controller. It only implies that the speaker dynamics must be considered in the controller design as discussed in the introduction. A more detailed discussion of the controller design is given in Chapter 2.

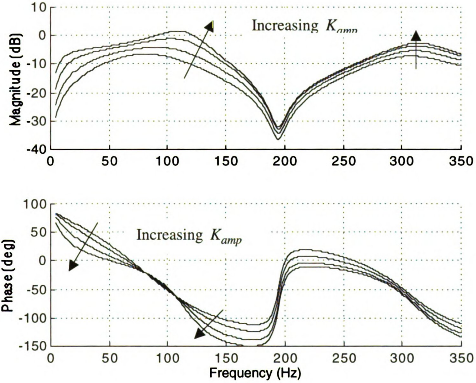

Figure 4.12. Frequency response simulation of the Q_2/D_I transfer function with the resonator and speaker with local feedback compensation added and controller removed, arrows indicate direction of increasing K_{amp} = 30, 50, 100, 200

Resonator, Speaker, Compensator and Controller.

Finally, with the compensated speaker model assembled, the closed loop control of the resonator can be modeled. Figure 4.13 shows the block diagram of the resonator and compensated speaker and controller with a disturbance D_2. The compensated speaker block contains the blocks in the dashed box in Figure 4.11.

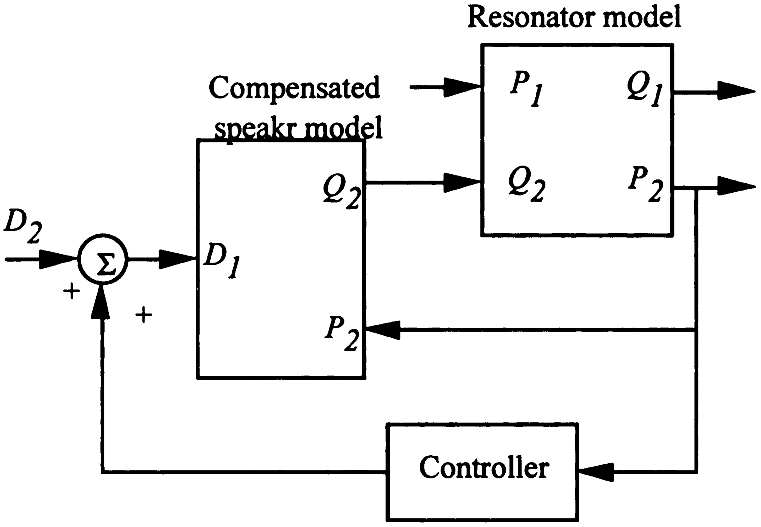

Figure 4.13. Block diagram of resonator, compensated speaker, and feedback controller with disturbance D_2

The closed-loop, compensated system response can now be simulated to verify that the acoustic resonance of the system can be modified by the feedback controller. A model based, empirical controller design (Chapter 2) was used to find gains that produced the desired response. Figure 4.14 shows the frequency response of the Q_1 / P_1 transfer function for four cases with the controller gains given in Table 4.3. These results show that the compensated actuator successfully implements the closed-loop control. The controller moves the frequency of the peak and zero phase to 106, 123, and 139 Hz. Note that the maximum amplitude of each resonant peak decreases with frequency. Also, the magnitude of graph C falls below the open-loop graph A at 45 Hz. This shows that if the

SHR is mistune then the closed-loop response can be worse than the open-loop response. These results show that with proper tuning, the compensated actuator and SHR behave as a tunable acoustic resonator.

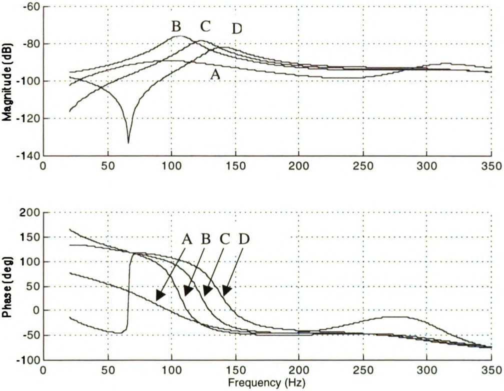

Figure 4.14. Frequency response of the Q_1/P_1 transfer function with the resonator, compensated speaker and feedback controller for four cases with gains shown in Table 4.3

Another transfer function P_2/D_l, is of interest in this system because it is used to compare the model and experimental results. Although the Q_1/P_1 transfer function is the key to the effectiveness of the device for noise control, it is difficult to measure experimentally. The volume velocity flow, Q_1, is a zero mean oscillating air velocity. A laser velocity anemometer can be used to make such a measurement, but this is an expensive and complex device. Instead, the P_2/D_l transfer function can be examined to observe the resonant frequency and damping. Figure 4.15 shows the closed-loop P_2/D_I transfer function with the gains in Table 4.3. The model based empirical controller design finds gains, K_P and K_I, that produce resonant peaks with constant magnitude in the P_2/D_I transfer function. Note this results in resonant peaks that decrease in amplitude with increasing frequency in the Q_1/P_1 transfer function (Figure 4.14). As before, the magnitude attains a peak and the phase crosses zero at the resonant frequency.

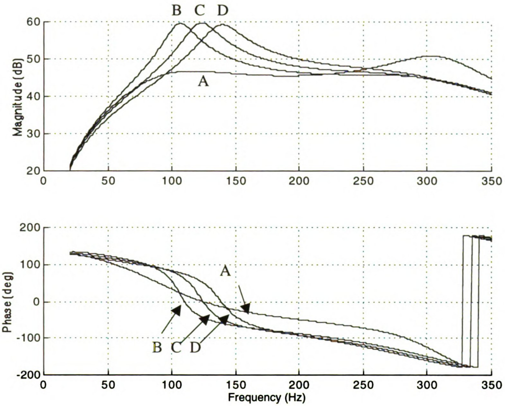

Figure 4.15. Frequency response of the compensated P_2/D_I transfer function: A: open-loop, B, C, and D closed-loop with gains selected to increase resonant peak and move resonant frequency

Table 4.3. Compensator and Controller gains used in Figures 4.14 and 4.15

Curves	A	B	C	D
Compensator In or Out	In	In	In	In
K_{amp}	30	30	30	30
K_P	0	-0.81	-0.90	-0.90
K_I	0	-250	0	250
Resonant Frequency (Hz)	102	106	123	139
Percent Damping	50	10	10	10

One undesirable feature of the speaker compensator is that it introduces noise into the actuator output. This is because it uses the voltage from the speaker secondary coil to estimate the secondary coil current. The secondary coil voltage is a low-level signal with a low signal-to-noise ratio. The noise is amplified by the compensator gain K_{amp}. This can be analyzed by modeling a disturbance D_3 input to the secondary coil current. The frequency response of the transfer function for P_2/D_3 is shown in Figure 4.16 for the compensator and controller settings in Table 4.3. These results indicate that random noise in the frequency range of 50 – 400 Hz will be injected into the actuator output. Although the signal-to-noise ratio could be increased by increasing the number of windings on the secondary coil, this was not done in this work.

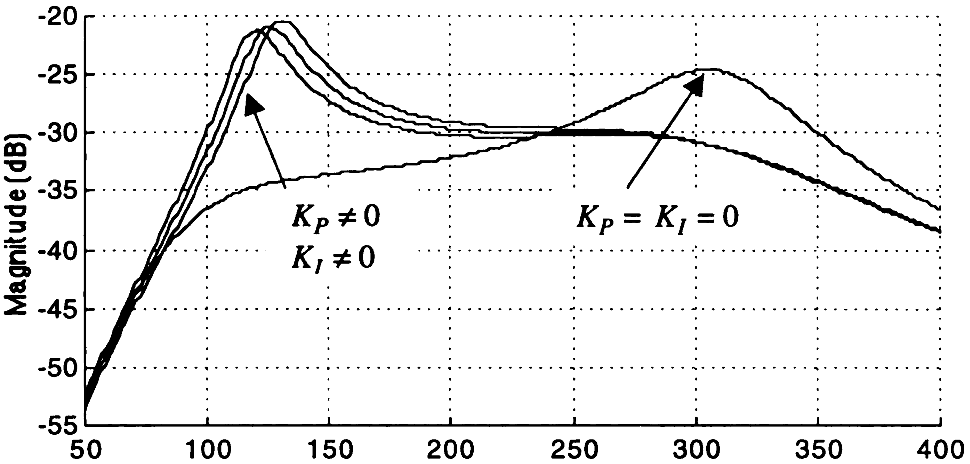

Figure 4.16. Frequency response of P_2 to current sensor disturbance for resonator, compensated speaker and feedback controller model with gains from Table 4.3

In summary, these simulations were presented to show that the compensated speaker is effective in implementing the control of the SHR. It was shown that the uncompensated actuator performance had excessive magnitude and phase variations and did not have unity gain. These actuator dynamics complicate the closed-loop controller design because the analytical mapping of the controller gains to the acoustic resonant frequency and damping assumes the actuator has unit gain. The speaker compensation was added as an attempt to minimize the actuator dynamics and simplify the controller design. It was shown that the compensation improved the speaker response below 100 Hz, but degraded the response above 100 Hz and that the coupled resonator and compensated speaker response did not converge to the resonator and ideal actuator model. The inability to remove the actuator dynamics from the system motivated the development of a model based, empirical controller design which was used to find controller gains that successfully re-tuned the acoustic system. These results bring into question the value of the speaker compensation and whether the compensation is worth the expense of the added complexity and introduction of noise.

Resonator, Speaker, and Controller (No Compensation)

A final model will be examined which includes the resonator, uncompensated speaker, and feedback controller, to compare the compensated system with the uncompensated system. The block diagram for the speaker compensation, Figure 4.11 includes a switch that removes the local feedback compensation from the loop. The model was assembled with the same components as the previous model, but with the local feedback compensation removed. The frequency response of the P_1/Q_1 transfer function for the resonator, uncompensated speaker, and feedback controller was then simulated and shown in Figure 4.17. It was found that the PI controller was not able to amplify and move the low frequency resonance (80 Hz). Instead the high frequency resonance at 290 Hz was amplified and moved by the application of the controller. Note that a peak in magnitude is attained and a zero phase occurs at the different resonant frequency. This verifies that the uncompensated actuator can be used in the SHR system.

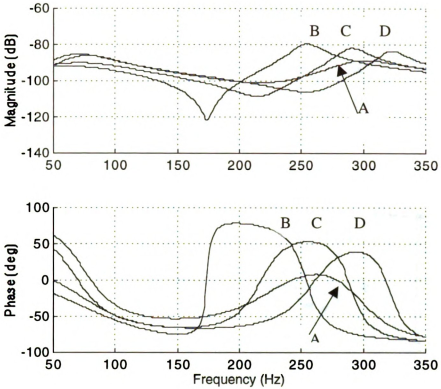

Figure 4.17. Frequency response simulation of the Q_1/P_1 transfer function with the resonator, uncompensated speaker, and feedback controller coupled model with controller gains from Table 4.4

The frequency response of the P_2/D_1 transfer function was also simulated, shown in Figure 4.18 for comparison with experimental results.

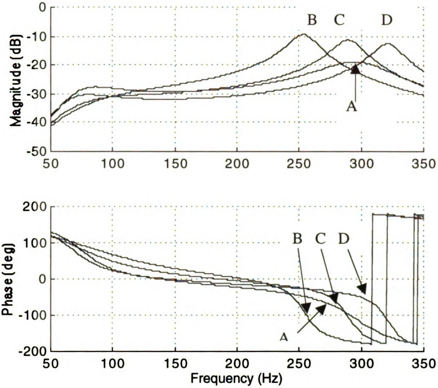

Figure 4.18. Frequency response simulation for the P_2/D_I transfer function with the resonator, uncompensated speaker, and feedback controller coupled model with controller gains from Table 4.4

Table 4.4. Controller gains used in Figures 4.17 and 4.18

Curves	A	B	C	D
K_P	0	-10	0	10
K_I	0	12,800	9,600	1,600
Resonant Frequency (Hz)	298	254	290	322
Percent Damping	50	10	10	10

The controller gains were selected to increase and decrease the resonance approximately 10% from the nominal value while maintaining a damping ratio of 10%. Note considerably different gains are needed to obtain these results as compared with the compensated system. The integral gain, K_I, is much larger than before, 1,600 to 12,800 compared to –100 to 100 for the uncompensated system. There are several explanations for this. A value of K_{amp} = 1 was used in the uncompensated system compared with

K_{amp} = 30 in the compensated system. Also, the integral of the pressure signal decreases with frequency, requiring a gain three times as large to affect the resonance at 300 Hz as one at 100 Hz. Note, too, that the trends of the gains are very different from those of the uncompensated system. A more complete discussion of the mapping of the controller gains to the resonant frequency and damping is beyond the scope of this article and is given in Chapter 5. Finally, note that the peak magnitudes of graphs B, C and D in Figure 4.17 are approximately 5 dB less than those with the compensated speaker model, Figure 4.14. Increasing the peak magnitude further would require reducing the system damping, which would lead to reducing the stability margin of the system.

These results indicate that the SHR with the uncompensated actuator is capable of producing an electronically tuned acoustic resonator. No significant noise is introduced into the system because the compensator is not present. Also the nominal resonant frequency is increased significantly to 300 Hz compared to the compensated system (130 Hz). However, the maximum magnitude of the uncompensated system is less than that of the compensated system.

A comparison of the compensated and uncompensated actuators suggest that each have use for different applications. The larger magnitude response of the compensated actuator suggests that it will be more effective in controlling noise in a narrow frequency band. That is, the compensated SHR will reflect more narrow frequency sound in a duct than the uncompensated SHR. It, therefore, may be more effective when the objective is to minimize narrow band pressure oscillations. However, the compensated SHR adds broadband noise to the system, thus degrading some of the noise reduction that is sought.

The uncompensated SHR does not reflect as much noise in a duct, but does not add as much noise to the system. It, therefore, may be more effective when the objective is to improve overall sound quality.

EXPERIMENTAL VALIDATION

An experimental apparatus was constructed to validate the theoretical model and to demonstrate the noise reduction capability of the device. A Helmholtz resonator and actuator are presented. The compensated, then uncompensated actuator was implemented, and the results are compared with theory.

The experimental SHR setup consisted of two components: a Helmholtz resonator cavity and a microphone-compensated actuator system. Figure 4.19 shows a photograph of the SHR connected to an acoustic duct and Figure 4.20 shows a schematic of the setup. A cylindrical Helmholtz resonator cavity was constructed from PVC with dimensions 0.075 m in diameter and 0.15 m in length. A cylindrical neck with dimensions 0.018 m in diameter and 0.01 m in length was fitted on one face of the cavity. The microphone-compensated actuator system consisted of a half-inch B&K type 4155 microphone sealed through the wall of the cavity. A D-Space Model #1102 floating point digital signal processor (DSP) was used to implement the speaker compensation, and an acoustic actuator was sealed in the opposite face of the cavity. A DSP sampling rate of 5 kHz was used for all experiments. The actuator consisted of a 6-inch dual voice coil speaker with local compensation (Birdsong and Radcliffe, 1999) to improve the speaker velocity response.

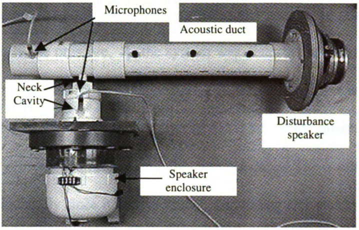

Figure 4.19. Photograph of SHR connected to an acoustic duct with a second audio speaker to inject noise

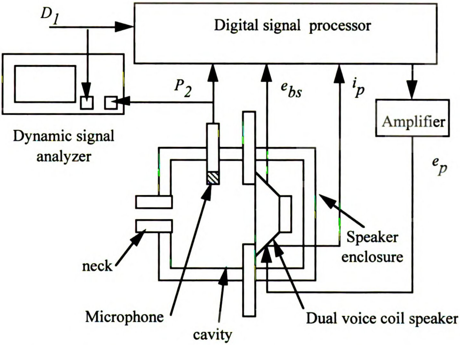

Figure 4.20. Schematic diagram of experimental SHR apparatus

In all phases of the system design, the device was separated from any primary acoustic system. This was not done arbitrarily for convenience, but because traditionally, mechanical and acoustic resonators are designed independently from the primary system. The usefulness of the device would be limited if the resonator response was dependent on the structure of the primary system. Fortunately, this is not the case; resonators can be designed with a tuning frequency and then applied to any suitable primary system. In the absence of a disturbance pressure, P_1, the system was disturbed electrically by the signal D_I injected via the actuator input voltage (Figure 4.20). Although it would be useful to measure the Q_1/P_1 transfer function directly since it is key in the interaction between the resonator and the primary acoustic system, this was not done. The quantity Q_1 is difficult to measure experimentally since it is a zero mean, oscillating air velocity. A laser velocity anemometer is a device that can be used for such measurements, however it was not used here because it is extremely costly, and experimentally complex. Consequently, the transfer function Q_1/P_1 is difficult to measure directly. Alternatively, the quantity P_2 and therefore, the transfer function P_2/D_I can be measured easily with a microphone. The system can be disturbed by either inputs P_1 or Q_2 since the characteristic polynomial which defines the resonant frequencies is the same regardless of the input. Therefore, the model was validated by comparing the model response for P_2/D_I with experimental measurements.

Compensated Actuator Results

A speaker velocity estimator (Birdsong and Radcliffe, 1999; Radcliffe and Gogate, 1996) was created by combining the voltage in the secondary coil with the current in the primary coil. A 10 ohm resistor was placed in series with the primary speaker coil to measure the current (Figure 4.21). The velocity estimate was then used to close the loop on the speaker velocity with a proportional controller (Figure 4.11). A value of $K_{amp} = 30$ was used in all trials. This value for K_{amp} is somewhat smaller than values used by Birdsong and Radcliffe (1999), where gains of as much as 100 were used.

The gain K_{amp} was chosen to increase the robustness of the system, which comes at the expense of performance.

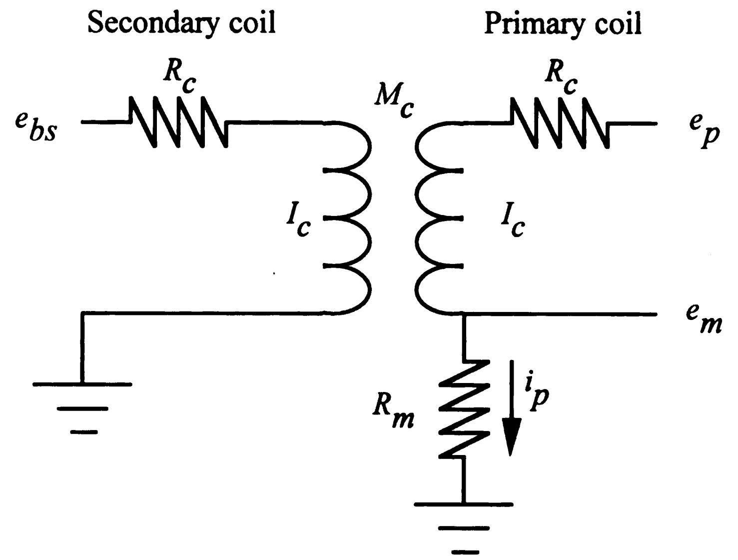

Figure 4.21. Primary coil current sensing circuit

Next, the controller was added to the system and gains were found to amplify the resonant peak and shift the resonant frequency. The gains were found using a model-based empirical technique (Chapter 5) that produced a response with different resonant frequencies and constant peak amplitude. Figure 4.22 shows the results for 4 experiments, curves labeled A, B, C, and D, which were generated using the controller gains in Table 4.5. These gains reduced the percent damping from 50% with $K_I = K_P = 0$ to 5% and shifted the peak from 130 Hz to 100 Hz and 170 Hz. Some discrepancies were found between the experimental and model gains, however the overall trends agreed with the gains in Table 4.3. The reader is refered to Chapter 4 for a more complete discussion of the mapping of the controller gains to the resonant frequency and peak amplitude.

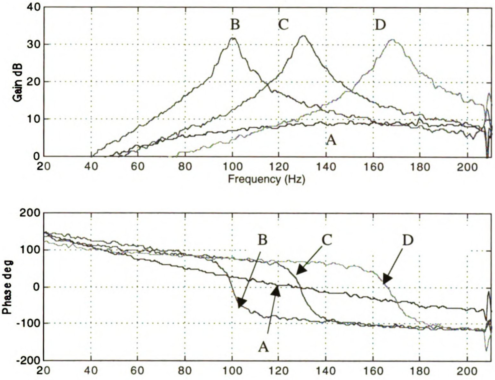

Figure 4.22. Experimental closed-loop frequency response of coupled system with compensated actuator showing that controller amplifies the peak magnitude and moves the resonant frequency

Table 4.5. Controller gains used in Figure 4.22

Graph	A	B	C	D
K_P	0	-0.34	-0.34	-0.24
K_I	0	-120	30	250
K_{amp}	30	30	30	30
Resonant Frequency (Hz)	130	100	130	170
Percent Damping	50	5	5	5

The next experiment demonstrates noise reduction in a duct and the introduction of random noise into the system by the actuator compensator. In this experiment the SHR was attached to an acoustic duct and a pure tone of 130 Hz was injected into one end of the duct by a second audio speaker (Figure 4.23). The sound pressure level (SPL) was then recorded at the duct end with the SHR in two configurations: first, with the uncompensated open-loop system, then with the compensated, closed-loop system with the controller gains selected to tune the system to 130 Hz. Figure 4.24 shows both spectra. With the uncompensated, open-loop system, the pure tone appears as a 117 dB spike in the spectrum at 130 Hz (dashed line). Other harmonics at 60 and 180 are attributed to distortion in the disturbance speaker. With the compensated, closed-loop system, the spectrum (solid line), shows the tone at 130 Hz is reduced dramatically to 85 dB, representing a 32 dB noise reduction. Nonetheless, significant background noise is introduced by the closed-loop actuator in a broad band between 60 and 200 Hz. This sound is below 80 dB, but becomes significant since the disturbance has been reduced to 85 dB. The shape of the broadband noise is similar to the P_2/D_2 transfer function result predicted by the model in Figure 4.10. It is attributed to random electrical noise introduced in the speaker secondary coil voltage and magnified by the compensation amplifier K_{amp}. The overall sound pressure level was also recorded at the open duct end using a B&K sound level meter. With the uncompensated, open-loop system, the overall sound pressure level was 118 dB, and with the compensated closed-loop system, the overall sound pressure level was 100 dB, representing 18 dB of overall SPL noise reduction. In summary, the narrow band noise at 130 Hz was reduced by 30 dB, but the overall SPL reduction was only 18 dB because of the addition of the broadband noise by the compensated actuator. Similar results were obtained with a disturbance frequency ranging from 100 to 150 Hz.

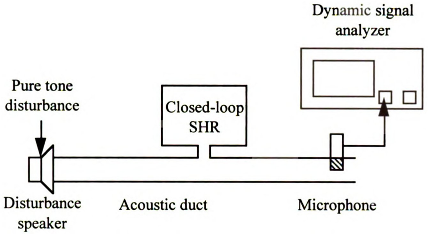

Figure 4.23. Schematic of experimental setup

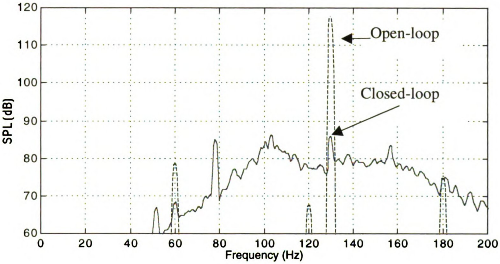

Figure 4.24. Sound pressure level in acoustic duct with SHR used to reduce pure tone disturbance, dashed line: compensator and controller out of the loop, solid line compensator and controller in the loop with controller gains set to tune SHR to the disturbance tone frequency of 130 Hz

Uncompensated Actuator Results

The previous experiments were repeated with the actuator in the uncompensated configuration. Figure 4.25 shows the uncompensated closed-loop P_2/D_I response without the duct with gains from Table 4.6. As predicted by the model, the uncompensated actuator does not resonate at the lower frequency. Instead the only resonance occurs at a higher frequency near 240 Hz. The controller was able to amplify the magnitude by 20 dB and shift the resonant frequency from 240 Hz with gains K_P = K_I = 0 higher and lower in frequency by 25 Hz. The resonant frequency for K_P = K_I = 0 is lower than the value predicted by the model, but otherwise, there is good agreement between these results and those derived from the model (Figure 4.12).

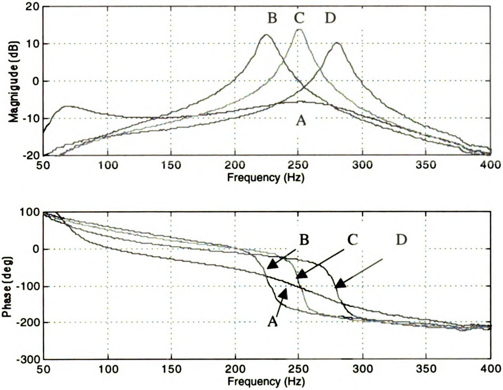

Figure 4.25. Experimental frequency response of closed-loop SHR with uncompensated actuator

Table 4.6. Controller gains used in Figure 4.25

Graph	A	B	C	D
K_P	0	0	1.0	2.0
K_I	0	2520	2520	1740
K_{amp}	1	1	1	1
Resonant Frequecy (Hz)	250	225	250	280
Percent Damping	50	6	6	6

The last experiment shows that the SHR with the uncompensated actuator reduces noise in a duct without introducing significant random noise into the system. The SHR and duct setup (Figure 4.23) was repeated with the uncompensated actuator and SHR. A pure tone of 185 Hz was injected into the duct end by the second audio speaker. Figure 4.26 shows the SPL spectrum recorded at the duct end with 2 configurations: first open-loop (dashed line), then closed-loop with gains set to tune the system to match the noise frequency (solid line). With the open-loop system, the peak SPL is 107 dB at 185 Hz. With the closed-loop system, the noise level is reduced to 98 dB, representing a 9 dB noise reduction. The background noise level is below 60 dB indicating that the uncompensated actuator does not introduce significant noise to the system. The overall SPL measured with a sound level meter showed identical results (9 dB noise reduction) indicating that in both open and closed-loop settings the noise is dominated by the narrow band tone at 185 Hz.

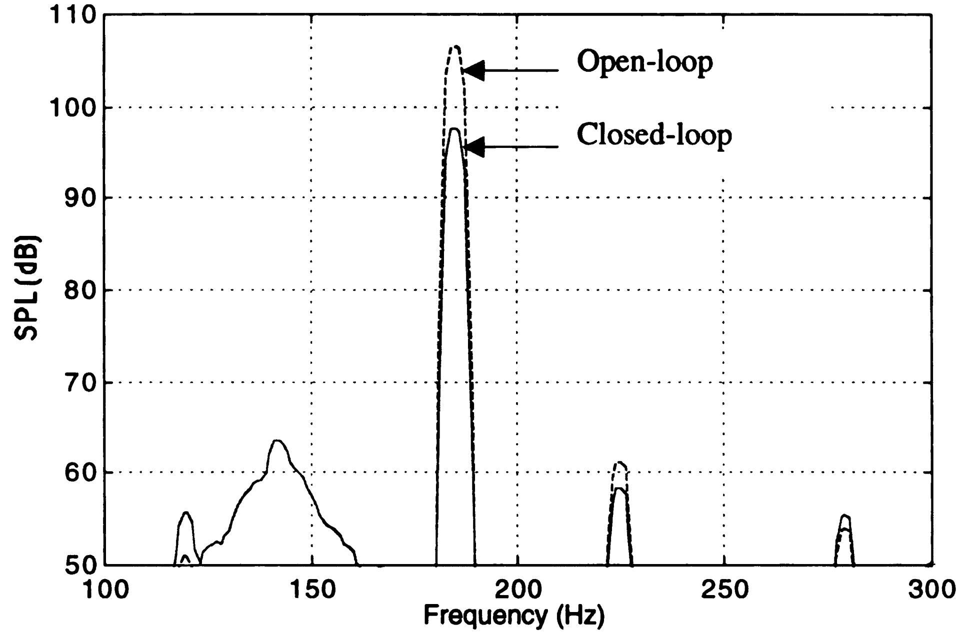

Figure 4.26. Sound pressure level spectrum with pure tone disturbance at 185 Hz with open and closed-loop SHR and uncompensated actuator

CONCLUSIONS

The actuator is a critical component in the implementation of the SHR. Compensated and uncompensated actuators were presented. Both were shown by analytical model and experimental results to be effective in the SHR. Both uncompensated and compensated actuators introduced significant dynamics into the system, requiring modification of the feedback controller design. However the compensated actuator was found to introduce random noise, degrading the overall SPL noise reduction. The uncompensated actuator did not introduce noise into the system, but could not generate as strong a resonance as the compensated actuator. It also had a higher resonant frequency. These conclusions lead to a criterion for choosing which actuator is optimal for different applications. For applications where a narrow band disturbance must be minimized without concern for the sound quality, the compensated actuator is superior. Alternatively, if sound quality is of concern, then the random noise introduced by the compensation may be objectionable even though the overall SPL is higher. In this case, the uncompensated actuator may be a better choice.

CHAPTER 5

Adaptive Control of a Semi-Active Helmholtz Resonator

A closed-loop adaptive control strategy is presented in this article for the SHR. Previously, the device was presented in a configuration that could be tuned to reflect sound back to the source at a single command frequency, selected to match the frequency of the unwanted noise. If this frequency changed, the command frequency could be modified by redesigning the control gains. This involved the operator turning potentiometers to vary the controller gains until the peak in the frequency response of the SHR coincided with the unwanted noise frequency. In this article, control strategies are considered which eliminate the human tuning process and replace it with an automated algorithm. The objective is to develop a self-tuning acoustic resonator that will track a pure tone, noise source with a slow time-varying frequency. A slow time-varying signal will consist of a pure tone with a frequency that changes at a rate on the order of 1 Hz/sec, which is intended to be typical of a rotating machine's performance.

A theoretical model of the system with an ideal actuator is presented and an analytical controller design is developed. An actuator model with internal dynamics is then added and shown to degrade the performance of the analytical controller design. This motivates the use of a model-based empirical controller design based on qualitative information learned from the model. A gain-scheduled adaptive controller is developed using this design technique. Numerical simulations and experimental results are given to demonstrate the effectiveness of the system at reducing noise in a duct and tracking a disturbance tone with slow time-varying frequency.

CONTROLLER DESIGN

A model of the system is first presented for the controller design. The central component of the SHR is a Helmholtz resonator with one surface of the cavity replaced by a moving surface (Figure 5.1). The system can be represented by linear time invariant state equations (Chapter 2)

$$\begin{bmatrix} \dot{Q}_1 \\ \dot{V} \end{bmatrix} = \begin{bmatrix} \frac{-R_a}{I_a} & \frac{-1}{I_a C_a} \\ 1 & 0 \end{bmatrix} \begin{bmatrix} Q_1 \\ V \end{bmatrix} + \begin{bmatrix} \frac{1}{I_a} & 0 \\ 0 & 1 \end{bmatrix} \begin{bmatrix} P_1 \\ Q_2 \end{bmatrix} \tag{5.1}$$

$$\begin{bmatrix} Q_1 \\ P_2 \end{bmatrix} = \begin{bmatrix} 1 & 0 \\ 0 & \frac{1}{C_a} \end{bmatrix} \begin{bmatrix} Q_1 \\ V \end{bmatrix} \tag{5.2}$$

where the states are Q_1, the volumetric flow rate or "volume velocity" from the neck (m^3/s) and V, the sum of the volumes introduced through the neck and the inner surface of the cavity (m^3). The inputs are P_1, the pressure at the neck inlet to the cavity (N/m^2), and Q_2, the volume velocity from the movable surface in the cavity (m^3/s). The outputs are Q_1 and P_2, the pressure in the cavity (N/m^2). The other parameters are R_a, the acoustic loss that represents viscous and radiation losses (Ns/m^5), I_a, the acoustic inertia of the mass of air in the resonator neck (Ns^2/m^5), and C_a, the acoustic compliance of the cushion of air in the resonator cavity (m^5/N).

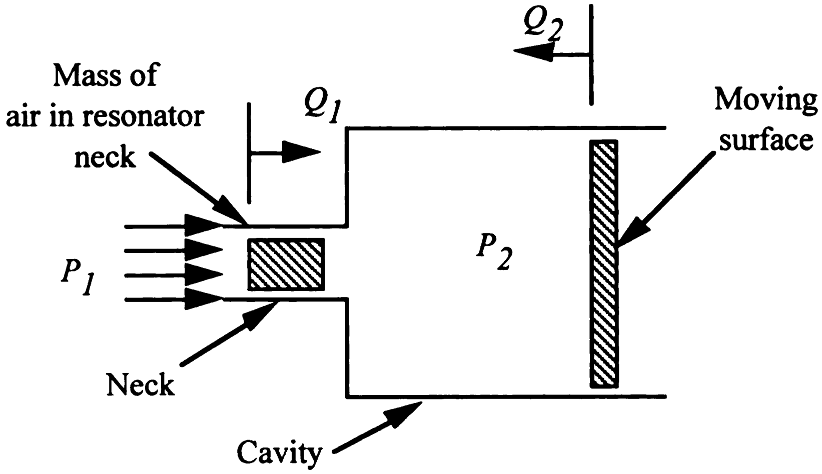

Figure 5.1. Schematic diagram of SHR showing inertia effect in neck and the movable surface in the cavity interior

An acoustic impedance can be generated on the moving inner surface of the cavity by enforcing a control law between P_2 and Q_2. This closed-loop, positive feedback configuration is shown in Figure 5.2. The actuator is first modeled as a transfer function with a pure gain of 1. The system can be disturbed either by P_1 or by D_l.

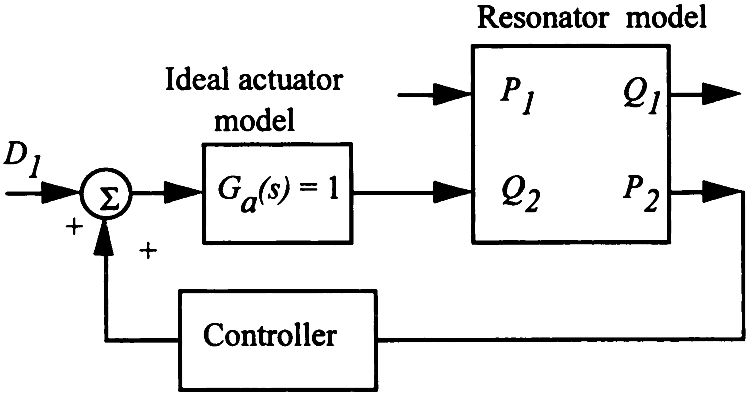

Figure 5.2. Closed-loop SHR system block diagram with disturbance through P_1

A proportional-integral (PI) controller,

$$G(s) = \frac{Q_2}{P_2} = K_P + \frac{K_I}{s} \tag{5.3}$$

can be used to generate the acoustic impedance on the cavity surface, where K_P and K_I are the proportional and integral gains respectively. The closed-loop transfer function for Q_1 / P_1 can be computed by substituting (5.3) into (5.1) and (5.2) converting the state equation into a transfer function (Phillips and Harbor, 1996), and simplifying which gives

$$\frac{Q_1}{P_1} = \frac{1}{I_a}\left[\frac{s^2 - \frac{1}{C_a}\left(K_P + \frac{K_I}{s}\right)s}{s^3 + \left(\frac{R_a}{I_a} - \frac{K_P}{C_a}\right)s^2 + \left(\frac{1}{I_a C_a} - \frac{K_I}{C_a} - \frac{R_a K_P}{I_a C_a}\right)s - \frac{R_a K_I}{I_a C_a}}\right] \tag{5.4}$$

This form of the transfer function shows how the controller gains affect the system response. The system is obviously not a simple second order resonator. The denominator of the transfer function is third order and the numerator is second order. More insight can be drawn from (5.4) by making some simplifying assumptions. For example, letting $R_a = K_P = 0$ and rearranging yields

$$\frac{Q_1}{P_1} = \frac{1}{s I_a}\left[\frac{s^2 - K_I}{s^2 + \left(\frac{1 - K_I I_a}{C_a I_a}\right)}\right] \tag{5.5}$$

This equation shows how K_I affects the poles of the transfer function. The term in brackets in the denominator of (5.5) represents the effective resonant frequency (squared) of the system. A positive K_I decreases the effective resonant frequency, and a negative K_I increases it. Recall that the control system uses positive feedback. This trend is the reverse of negative feedback systems where positive gain increases the effective stiffness of the system. Also note that the system response is volume velocity relative to pressure. In mechanical resonators systems, the displacement relative to force impedance becomes stiffer as the proportional gain is increased. Displacement is the integral of velocity, explaining why an integral controller gain changes the apparent stiffness in this system.

Similarly, setting $K_I = 0$ gives

$$\frac{Q_1}{P_1} = \frac{1}{I_a}\left[\frac{s - \frac{K_P}{C_a}}{s^2 + \left(\frac{R_a}{I_a} - \frac{K_P}{C_a}\right)s + \frac{1}{I_a C_a}\left(1 - R_a K_P\right)}\right] \tag{5.6}$$

This equations shows that K_P appears as a term that is subtracted from the acoustic loss term R_a. Increasing K_P reduces the apparent acoustic loss and hence reduces the system damping. The apparent acoustic loss can be either increased with a negative K_P, adding additional damping to the system, or decreased with a positive K_P, reducing system damping and increasing the peak magnitude at resonance.

This analysis illustrates the ability of the SHR to change the dynamic response of the system. Each gain K_P and K_I gives an input to change the apparent resonant frequency and peak amplitude of the Helmholtz resonator. The advantage of this effect is that the response of the Helmholtz resonator is modified without changing the physical dimensions, i.e., cavity volume, neck length or cross section area. The change in response is caused only by the interaction of the controller with the Helmholtz resonator.

Finally, setting $K_P = K_I = 0$ produces a transfer function that gives the nominal resonant frequency of the device. Note that $K_P = K_I = 0$ implies that the actuator is held fixed and becomes a rigid wall of the cavity.

A range of gains K_I and K_P that produce a stable system can be found by examining the characteristic polynomial (denominator of (5.4)). The system is stable provided that there are no sign changes in the coefficients of the characteristic polynomial (Phillips and Harbor 1996). This produces the following ranges for the gains:

$$K_P < \frac{R_a C_a}{I_a} \tag{5.7}$$

$$K_I < 0 \tag{5.8}$$

These bounds on the gains determine the limitation of the controller to tune the system, defining a design space for the controller gains. Acoustic loss is affected by K_P (5.6). The limit (5.7) translates into a maximum amount of damping that can be removed from the system before marginal stability is reached. The resonant frequency is affected by K_I (5.5). The limit (5.8) translates into a limit on the direction the resonance frequency can be moved from the nominal value. In this case a negative K_I increases the value of the resonance frequency, and (5.8) indicates that the resonance frequency can not be decreased from the nominal value.

A slightly modified controller increases the limits on the gains and thereby increases the tunable range of the SHR. The integrator in 5.3 has infinite DC gain. By adding a low frequency pole, p_l, to the integrator

$$G(s) = \frac{Q_2}{P_2} = K_P + \frac{K_I}{s + p_1} \tag{5.9}$$

the DC gain is reduced to a finite value. Substituting (5.9) into (5.1) and (5.2) produces the closed loop system. The coefficients of the characteristic polynomial can be computed in terms of the acoustic and controller parameters. The space of stable gains can be visualized by setting each coefficient equal to 0 and plotting the resulting functions in the K_P-K_I space. Each curve gives a bound defined by a coefficient in the characteristic polynomial. Figure 5.3 shows the stable gain space indicated by the shaded area, with p_I = 100 and acoustic parameters in Table 5.1. The gain K_P has an upper limit of K_P = 1.1 e -6 (positive) (curve A), and no lower limit. The gain K_I has an upper limit of K_I = 6.0 e -3 (positive) (curve B) and no lower limit. The curve labeled C is a redundant constraint on K_I. The dashed lines indicate the negative direction of each coefficient. These results indicate that K_I can have both positive and negative values. The resonant frequency is affected by K_I, therefore the apparent resonant frequency of the system can be both increased and decreased.

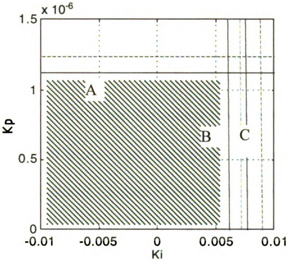

Figure 5.3. Plot of stable gain space for controller gains K_P and K_I

Table 5.1. Acoustic parameters used in simulation

Parameter	Value
I_a	162 $\mathrm{Ns^2/m^5}$
C_a	7.2e-9 $\mathrm{m^5/N}$
R_a	7.5e4 $\mathrm{Ns/m^5}$

Analytical Controller Design

An analytical controller design is developed by computing an analytical mapping from the controller gains to the resonant frequency and damping of the closed-loop system. The design space defined by the range of stable gains can be examined using pole placement. The desired denominator of the transfer function can be represented by

$$G(s)_{\text{desired}} = \left(s^2 + 2\zeta\omega_n s + \omega_n^2\right)(s + p) \tag{5.10}$$

The values of the damping ratio, ζ and the natural frequency, ω_n can be chosen. The pole p_2 can not be chosen, but becomes an output of the calculation. The ideal integrator (5.3) is used to simplify the model. Setting (5.10) equal to the denominator of (5.4) and matching coefficients in s, the values of K_P, K_I and p_2 can be computed from the resulting linear system of equations. The solution is given by

$$K_p = \frac{R_a - 2C_a R_a^2 \omega_n \zeta - 2C_a I_a^2 \omega_n^3 \zeta + 4C_a I_a R_a \omega_n^2 \zeta^2}{R_a^2 + I_a^2 \omega_n^2 - 2I_a R_a \omega_n \zeta} \tag{5.11}$$

$$K_I = \frac{\omega_n^2\left(I_a - C_a R_a^2 - C_a I_a^2 \omega_n^2 + 2C_a I_a R_a \omega_n \zeta\right)}{R_a^2 + I_a^2 \omega_n^2 - 2I_a R_a \omega_n \zeta} \tag{5.12}$$

$$p_2 = \frac{R_a\left(C_a R_a^2 + C_a I_a^2 \omega_n^2 - I_a - 2 I_a C_a R_a \omega_n \zeta\right)}{C_a I_a\left(R_a^2 + I_a^2 \omega_n^2 - 2 I_a R_a \omega_n \zeta\right)} \tag{5.13}$$

where it is assumed that the acoustic parameters are known. The values for ω_n and ζ are replaced by command variables ω_c and ζ_c which are chosen to produce the desired system response.

Gain-Scheduled Adaptive Control

An adaptive gain-scheduled control algorithm can be constructed from the above formulations. The gain scheduling variable ω_C is updated at a rate much slower than the time constant of the resonant system and must be estimated from the disturbance signal on line. The objective is to tune the system so that a resonance with a large peak occurs at an arbitrary command frequency, ω_C, which is set to equal the estimated value of ω_n. The height of the peak can be controlled by setting the value of ζ_c. The strategy used here is to place the complex poles at a constant distance from the imaginary axis for all values of ω_C. This can be accomplished by applying the constraint

$$\zeta_c = k / \omega_c \tag{5.14}$$

where k is a scalar constant that defines the distance of the complex poles from the imaginary axis assuming that ζ_c is small. The parameter, k is equivalent to the inverse of the time constant of the complex poles (Phillips and Harbor, 1996). Figure 5.4 shows a plot of the closed-loop system pole locations indicated by an 'x' computed with gains from (5.11) – (5.13) with the parameters in Table 5.1 and ω_C ranging from 560 to 820 rad/s. The distance of the real pole closest to the imaginary axis for the smallest value of

ω_C depends on the value of k. Ideally this pole is aligned with the complex poles so that the slowest settling time is minimized. This optimum value of k can be determined from the model by trial and error. For the case shown here, a value of $k = 4$ (time constant = 0.25 sec) aligned the smallest real pole with the complex poles. The choice of k has little effect on the real poles for larger values of ω_C, where the real pole is far to the left of the complex poles, indicating a fast settling time.

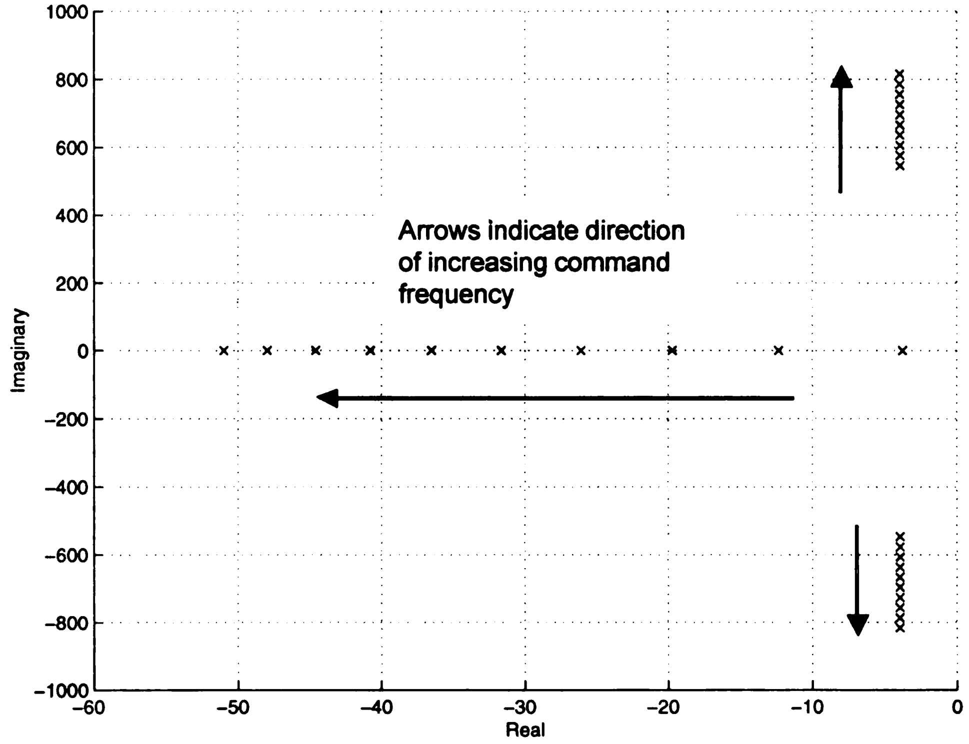

Figure 5.4. Plot of pole locations for gain-scheduled controller algorithm for command frequency ranging from 560 to 820, $k = 4$ aligns the smallest real pole with the complex poles for the smallest value of ω_C

Gain-Scheduled Controller Simulation

For simplicity, the control will be implemented with the resonator neck open to atmospheric pressure instead of connected to a primary acoustic system. The normal operation is with a primary acoustic system producing P_1 at the resonator neck and having this input become the disturbance to the system. From the control viewpoint, the system can be disturbed by either input, P_1 or Q_2. The motivation for disturbing the system through Q_2 is that this approach eliminates the dynamics associated with the primary acoustic system and focuses the analysis on the dynamics of the SHR alone. Also, this is the traditional approach used in mechanical and acoustic resonator design. In the absence of a driving pressure, P_2, the system will be disturbed electronically. Figure 5.2 shows the block diagram of the SHR with a disturbance D_I, added to the controller output. The other input, P_1, is then set to zero, representing atmospheric pressure at the SHR neck, and Q_1 is a free boundary condition.

The closed-loop transfer function relating the system output P_2 to the input D_I is computed from (5.1) and (5.2) and given by (5.15). Note the denominator of (5.15) which characterized the system dynamics is identical to the previous implementation (5.4) where the disturbance was through P_1. This confirms that the previous stability and gain scheduling analysis applies when the disturbance is through either P_1 or Q_2. It should be noted that the numerators of (5.4) and (5.15) are not identical. This will result in different magnitudes and phase characteristics between the two transfer functions. However the resonant frequency and damping is a function of the characteristic polynomial which is invariant to the choice of inputs and outputs.

$$\frac{P_2}{D} = \frac{s\left(s + \frac{R_a}{I_a}\right)}{s^3 + \left(\frac{R_a}{I_a} - \frac{K_P}{C_a}\right)s^2 + \left(\frac{1}{I_a C_a} - \frac{K_I}{C_a} - \frac{R_a K_P}{I_a C_a}\right)s - \frac{R_a K_I}{I_a C_a}} \tag{5.15}$$

The preceding gain-scheduled controller was applied to the plant model and the time response was simulated for various inputs. A block diagram of the system is shown in Figure 5.5. Note that the frequency of P_2 must be determined on-line. This can be done by various methods. For the simulation, the instantaneous frequency was known to the controller, i.e., the frequency estimator was perfectly accurate and responded instantaneously. This was a significant assumption used to simplify the model and simulation.

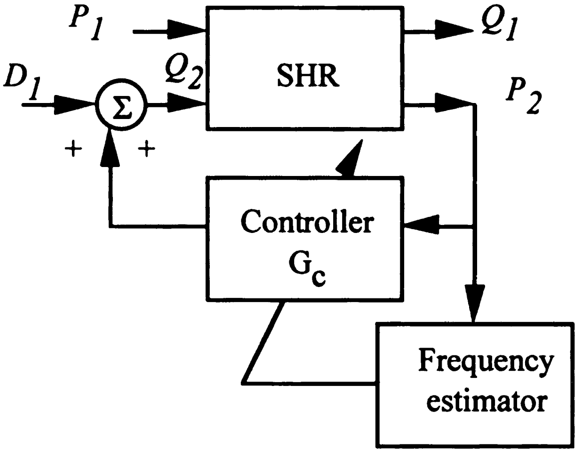

Figure 5.5. Adaptive gain scheduling control block diagram

The numerical simulation demonstrates that the system tracks a disturbance with slow time-varying frequency. The disturbance frequency starts at 565 rad/s (90 Hz) and increases to 595 rad/s (95 Hz) in 2 seconds. Figure 5.6 shows the time response of the system. The top graph shows the frequency estimate output. The input D_1, is a sinusoidal input with amplitude 1 N/m^2. The middle graph shows P_2 with the controller turned off. The amplitude is initially small and decreases further as the disturbance frequency moves away from the nominal resonant frequency (86 Hz). The bottom graph shows P_2 with the controller turned on. The controller re-tunes the system so that the resonant frequency tracks the changing input frequency. The system starts from rest and the amplitude grows until steady state is achieved, after about 0.5 seconds. At steady state, the amplitude of P_2 is 15 times (23 dB) larger than the open-loop response. As the input frequency changes, the amplitude remains constant compared to the open-loop case, where the amplitude diminished as the driving frequency moves away from the nominal resonant frequency. This simulation demonstrates that the system acts as a resonator with variable tuning which tracks the input signal frequency.

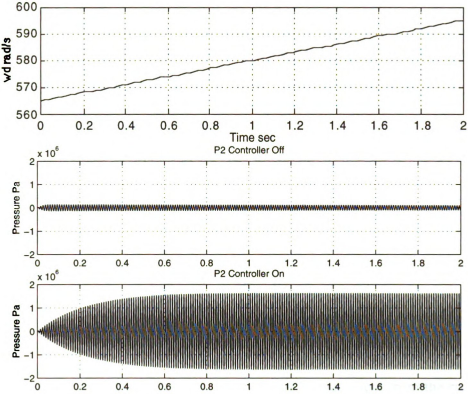

Figure 5.6. Numerical simulation of SHR to disturbance tone with time-varying frequency showing that system resonates with constant magnitude as the disturbance frequency changes

Actuator Dynamics

Analysis was performed to investigate the effects of actuator dynamics on the closed-loop response of the system. The previous analysis assumed an ideal actuator, i.e., the actuator velocity, and Q_2 is proportional to the voltage input to the actuator. This is a reasonable assumption for analysis of the fundamental response of the SHR since further detail depends on the structure of the actuator. However, pole placement is known to be sensitive to modeling errors and a gain scheduling control strategy must account for actuator dynamics.

A velocity compensated dual voice coil speaker will be used in the experimental verification of the SHR. An accurate model of this device was presented by Birdsong and Radcliffe (1999). This actuator compensates the velocity for internal dynamics and pressure interactions on the face of the actuator. The result is an actuator with reduced magnitude and phase variation between command signal and actuator output within a limited frequency range of 20 to 400 Hz. The dual voice coil speaker can be represented by the linear time invariant state equations (Radcliffe and Gogate, 1996; Birdsong and Radcliffe, 1999).

$$\frac{d}{dt}\begin{bmatrix} Q_2 \\ q_2 \\ \lambda \end{bmatrix} = \begin{bmatrix} \frac{-R_s}{I_s} & \frac{-1}{C_s I_s} & \frac{blS_d}{I_c I_s} \\ 1 & 0 & 0 \\ \frac{-bl}{S_d} & 0 & \frac{-R_m - R_c}{I_c} \end{bmatrix} \begin{bmatrix} Q_2 \\ q_2 \\ \lambda \end{bmatrix} + \begin{bmatrix} 0 & 0 \\ 0 & \frac{-S_d}{I_s} \\ 1 & 0 \end{bmatrix} \begin{bmatrix} e_p \\ P_2 \end{bmatrix} \tag{5.16}$$

where the states are the volume velocity and volume displacement from the speaker, Q_2, and q_2, and the electromagnetic flux in the speaker coil, λ. The inputs are the primary coil voltage, e_p, and pressure on the speaker face, P_2. The output equation is given by

$$\begin{bmatrix} e_{bs} \\ i_p \\ Q_2 \end{bmatrix} = \begin{bmatrix} bl\left(1 - \frac{M_c}{I_c}\right) & 0 & \frac{-M_c}{I_c^{\,2}}(R_c + R_m) \\ 0 & 0 & \frac{1}{I_c} \\ 1 & 0 & 0 \end{bmatrix} \begin{bmatrix} Q_2 \\ q_2 \\ \lambda \end{bmatrix} + \begin{bmatrix} \frac{M_c}{I_c} & 0 \\ 0 & 0 \\ 0 & 0 \end{bmatrix} \begin{bmatrix} e_p \\ P_2 \end{bmatrix} \tag{5.17}$$

where the outputs are the voltage in the secondary coil, e_{bs}, the current in the primary coil, i_p, and Q_2. The parameters in (5.16) and (5.17) are the speaker face area, S_d, speaker inertia, I_s, speaker compliance, C_s, speaker friction, R_s, speaker coil resistance, R_c, speaker coil inductance, I_c, speaker coil mutual inductance, M_c, speaker electromechanical coupling factor, bl, and the primary coil current sensing resistance, R_m.

A velocity estimator can be generated from two measurable speaker outputs (the secondary coil voltage, e_{bs}, and the primary coil current, i_p)

$$v_{spkr}(s) = H_{bs}e_{bs}(s) - H_p(s)i_p(s) \tag{5.18}$$

where $H_{bs} = 1/bl$ and $H_p(s) = s\, M_c/bl$.

The secondary coil voltage, e_{bs}, can be measured directly from the speaker coil. The primary coil current, i_p, can be determined from the voltage across a resistor, R_m, placed in series with the primary coil. The mathematically improper, differentiating transfer function, H_p, cannot be realized exactly, but an approximation

$$\hat{H}_p(s) = \frac{M_c}{bl}\left(\frac{p_1 s}{s + p_3}\right) \tag{5.19}$$

can be used, where p_3 is a pole location selected such that $\hat{H}_p(s)$ approximates $H_p(s)$ over the controller bandwidth. Feedback compensation can now be implemented using the signal from the velocity sensor to compute the error between the desired velocity and the sensor velocity and a proportional controller to drive the speaker velocity to the desired velocity. The compensated speaker model can now be coupled with the resonator and controller model (Figure 5.7) and the closed loop response can be simulated.

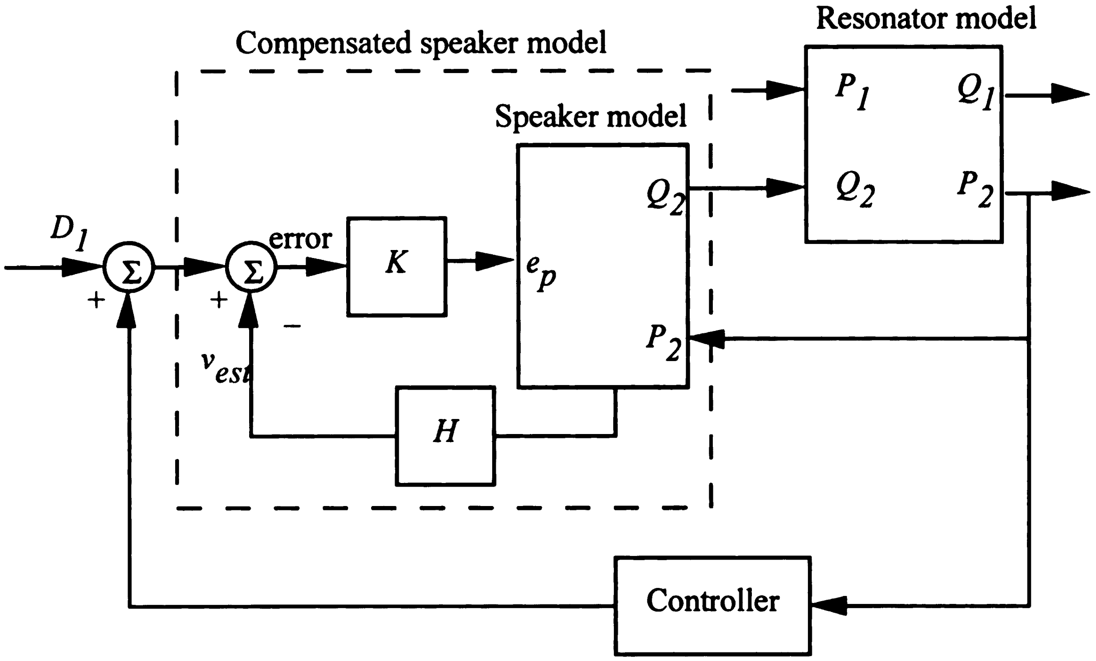

Figure 5.7. Block diagram of resonator, controller, and compensated speaker with disturbance through D_l

The effect of the actuator dynamics on the controller design can be determined by examining the closed-loop pole locations. The gain schedule control algorithm used in the results presented in Figure 5.4 is applied to the SHR and speaker model. The pole locations of the closed-loop system are calculated for various values of ω_c and plotted in Figure 5.8. The actuator model adds additional dynamics and therefore there are more poles. Figure 5.8 shows one real pole and 4 complex poles as ω_c is varied from 560 to 820 rad/s. In addition, there are 2 higher frequency complex poles not shown in Figure 5.9 because they are located an order of magnitude to the left of the poles of interest and the different scales would make it difficult to compare with Figures 5.4. The gain schedule objective is to provide varying resonant frequencies with the same time constant. The additional actuator dynamics prevents this from occurring. The complex poles are no longer aligned and the imaginary part of the poles do not correspond with the values of ω_c.

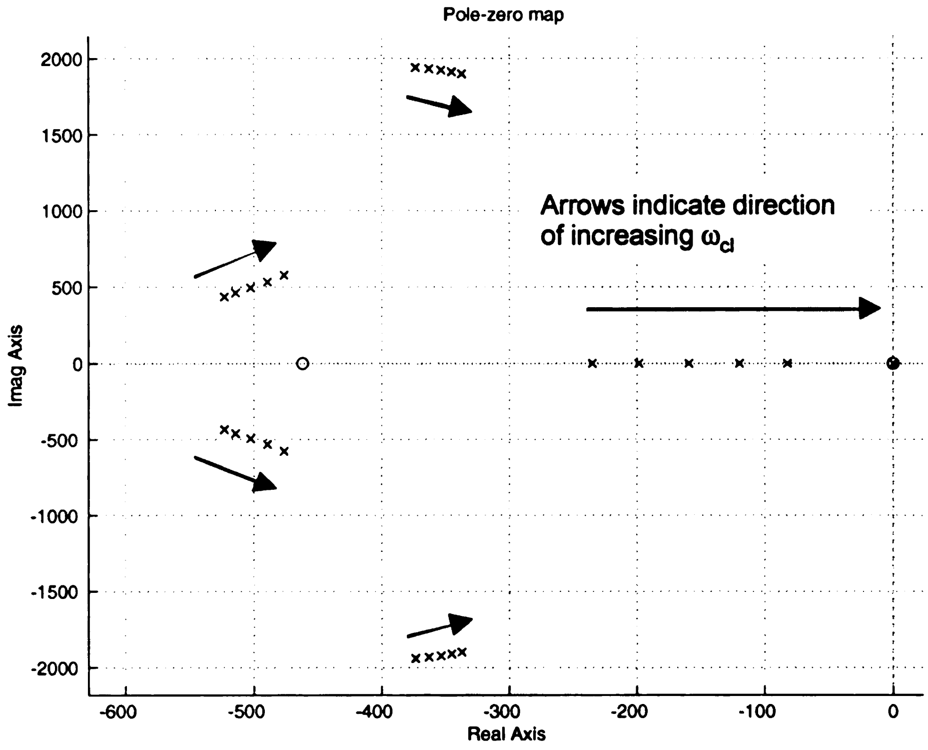

Figure 5.8. Pole locations of SHR with actuator dynamics and ideal SHR gain scheduling algorithm showing that the root locus no longer achieves the desired pole placement strategy when finite actuator gains are included in the model

The analytical control design is not effective in the presence of finite unmodeled actuator dynamics and a different approach must be taken. The ideal actuator assumption was unrealistic. The analytical controller design is too sensitive to changes in the pole locations from unmodeled actuator dynamics. A new control design is needed that captures these effects. The closed-loop response of the system is a complex function of the acoustic and actuator parameters. The SHR (5.4) is a third order model, and the actuator model is a third order model (5.16), so the combination is sixth order. The closed form solution given by (5.11) through (5.13) relating K_P and K_I to ω_n and ζ

does not account for actuator dynamics. Furthermore, a new solution is not easily found for the sixth order model that maps the controller gains K_P and K_I to ω_n and ζ.

A different approach that can be used in place of the analytical controller design is a model-based empirical controller design. The assembled model, including the SHR (5.1) and (5.2), the controller (5.9), and the actuator (5.16) and (5.17) can be used to search for values of K_P and K_I that produce complex poles that meet the same criterion as before i.e., move the resonant frequency while maintaining equal time constants. The model eigenvalues can be computed for different gains using numerical simulation. Although there is no closed-form solution that guides the search for the gains, a good starting place is to use the same trends found in the analytical controller design. The SHR and ideal actuator model indicated that K_I affects the apparent resonant frequency (5.5) and K_P affects the apparent damping (5.6). The search technique used here fixes a value of K_I, then searches K_P to produce the desired damping. Alternatively, instead of maintaining constant damping, the technique could align the real parts of the complex poles, thus maintaining an equal time constant for different resonant frequencies. The distance from the imaginary axis to a pole gives the inverse of the time constant for the pole (Phillips and Harbor, 1996). This criterion was used for K_P. This was repeated for various values of K_I until an empirical mapping was found between frequency and damping.

The empirical controller design successfully produced a mapping between the controller gains and the resonant frequency and damping. Figure 5.9 shows the values of K_P and K_I on the vertical axis, vs. the resulting resonant frequency on the horizontal axis. The gains were selected to maintain equal time constants for each setting. It was found that the resonant frequency was strongly correlated with K_I, and both negative and positive values of K_I produced stable systems (all poles in the left half plane). Negative values of K_P increased the time constant (reduced the distance between the imaginary axis and the complex poles). An extremely flat, parabolic-shaped trend was observed between K_P and the resonant frequency, with the minimum located at the nominal resonant frequency (130 Hz). Slight variations in K_P were required to obtain equal time constants with less than approximately 10% variation in K_P for most settings.

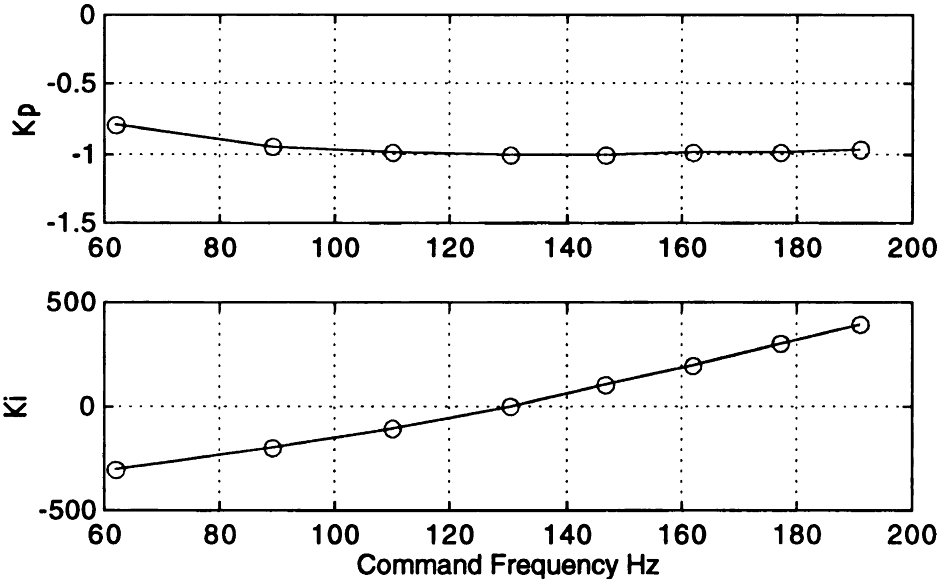

Figure 5.9. Plot of K_P and K_I vs. ω_C determined using model-based empirical controller design technique

Figure 5.10 shows the pole locations of the closed-loop system for the gains from Figure 5.9. Higher frequency poles are not shown to focus on the complex poles that produce the acoustic resonance. The complex poles are aligned at –30 resulting in a time constant of 1/30 = .033 seconds. The resonant frequency can be computed from the distance of each pole to the origin and range from 62 to 191 Hz.

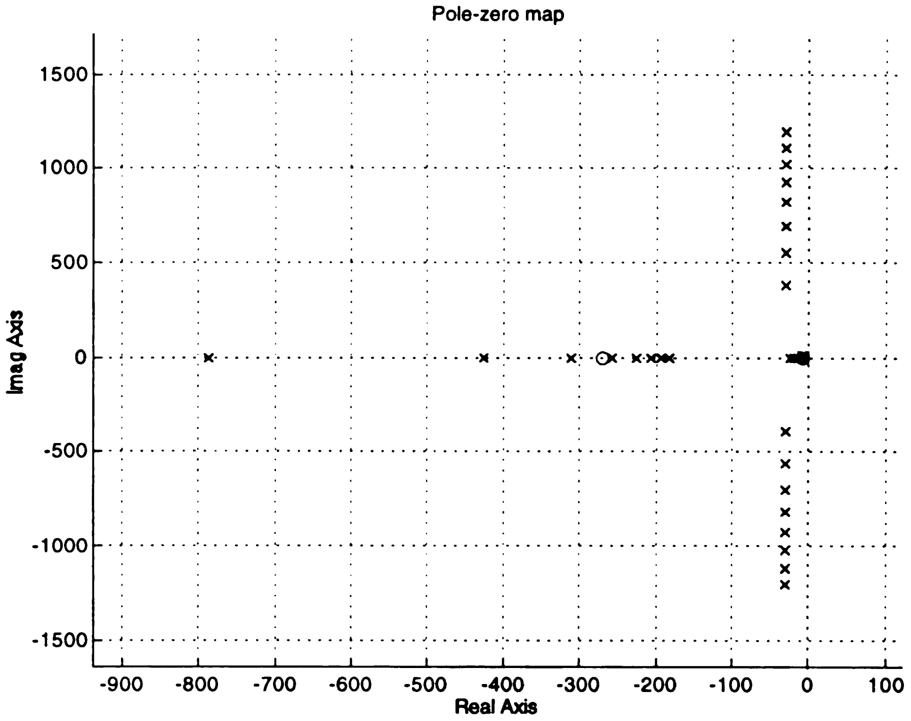

Figure 5.10. Plot of closed-loop pole locations for 7 controller settings derived from the model-based empirical controller design technique

Stability is guaranteed provided all closed-loop poles lie in the left half plane. This can be confirmed by examining the eigenvalues of the closed-loop system model for the scheduled gains. The controller design process is based on placing the complex poles in the left half plane, but other poles appear near the origin in Figure 5.10. These poles are associated with the integrator and choosing the value of p_I (5.9) moves them away from the imaginary axis. Kahlil (1996) presents a stability proof for slow time-varying systems that applies to the gain-scheduled control of the SHR. The proof is simplified by the additional condition that the system with the scheduling variable "frozen" is linear, as is the SHR model. This proof concludes that the system is stable given a limit to the rate of change of the scheduling variables, which can be related to parameters in the model. It is assumed in this control design that the scheduling variable ω_c changes much slower than the dynamics of the system.

In summary, the SHR gain-scheduled controller was designed using a model-based empirical technique. The scheduling variable is the disturbance noise frequency that must be estimated on line. The details of frequency estimator techniques are not discussed here. The gain-scheduled controller then schedules 2 gains: K_P and K_I in a PI controller. The model predicts the trends of K_P and K_I vs. ω_n and identifies that ω_n and ζ are very sensitive to small changes in K_P. This sensitivity identified the need for experimental verification of the empirical gain scheduling, especially in scheduling K_P, to achieve the desired response. Finally, it should be noted that the analysis was performed on the SHR with no primary acoustic system. This is common practice with classical Helmholtz resonator design, where the device is designed to resonate at a frequency while separate from any primary acoustic system. The SHR control algorithm was designed this way, and, in the experimental validation, an acoustic duct will be added to verify the performance of the device on a primary acoustic system.

EXPERIMENTAL VALIDATION

An experimental apparatus was constructed to validate the theoretical model and demonstrate the effectiveness of the SHR at reducing noise in a duct. In this section the Helmholtz resonator and actuator implementation will be presented, the gain scheduling controller will be implemented and finally, the SHR will be applied to an acoustic duct to demonstrate the control algorithm's tracking and noise reduction capability.

The experimental SHR setup consisted of two components: a Helmholtz resonator cavity and a microphone-compensated actuator system. Figure 5.11 shows a photograph of the SHR connected to an acoustic duct and Figure 5.12 shows a schematic of the setup without the duct. A cylindrical Helmholtz resonator cavity was constructed from PVC with dimensions 0.075 m in diameter and 0.15 m in length. A cylindrical neck with dimensions 0.018 m diameter and 0.01 m in length, was fitted through one face of the cavity. The control system consisted of a microphone, controller and actuator. A half-inch B&K type 4155 microphone was sealed through the wall of the cavity, a D-Space Model #1102 floating point, digital signal processor (DSP) was used to implement the speaker compensation, the controller, and to generate a disturbance tone, and a compensated 6-inch dual voice coil speaker was used as the actuator. A DSP sampling rate of 5 kHz was used for all experiments.

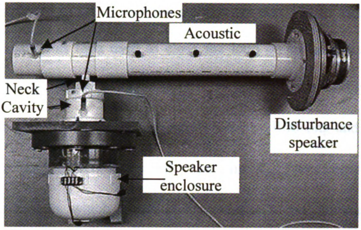

Figure 5.11. Photograph of SHR connected to an acoustic duct with a disturbance speaker to inject noise

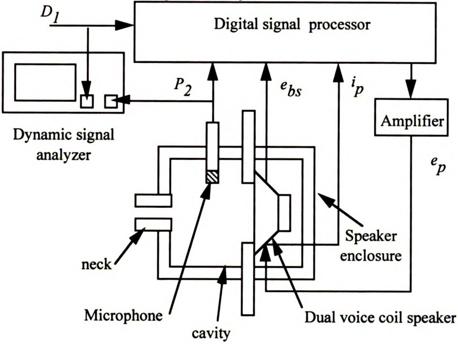

Figure 5.12. Schematic diagram of experimental SHR apparatus

Speaker Compensation

The speaker was compensated to improve its performance, but finite gain and phase errors in the actuator response affected the system. A speaker velocity estimator (Birdsong and Radcliffe, 1999; Radcliffe and Gogate, 1996) was implemented by combining the voltage in the secondary coil with the current in the primary coil. A 10 ohm resistor was placed in series with the primary speaker coil to measure the current. The velocity estimate was then used to close the loop on the speaker velocity with a proportional controller (Figure 2.13). A value of $K_{amp} = 30$ was used for all trials. This value for K_{amp} is somewhat smaller than values used by Birdsong and Radcliffe (1999) where gains of as much as 100 were used. The gain K_{amp} was chosen to increase the robustness of the system, which comes at the expense of performance. The speaker velocity was measured directly to confirm that the transfer function of the actual speaker velocity relative to the desired velocity was acceptable. This was done by directing a laser velocimeter through the SHR neck onto reflective tape on the speaker face. With the relatively low value of K_{amp}, there was less than 5 dB and 100 degrees of magnitude and phase between desired and actual speaker velocity in the frequency range of 20 to 200 Hz in all experiments. While this represents a 15 dB and 80 degree improvement over uncompensated audio speakers, it clearly does not approach the ideal actuator model of a transfer function with a pure gain of 1. After the compensator was implemented, the closed-loop speaker compensation was considered a single block in the SHR, and all subsequent open and closed-loop SHR experiments included closed-loop speaker compensation.

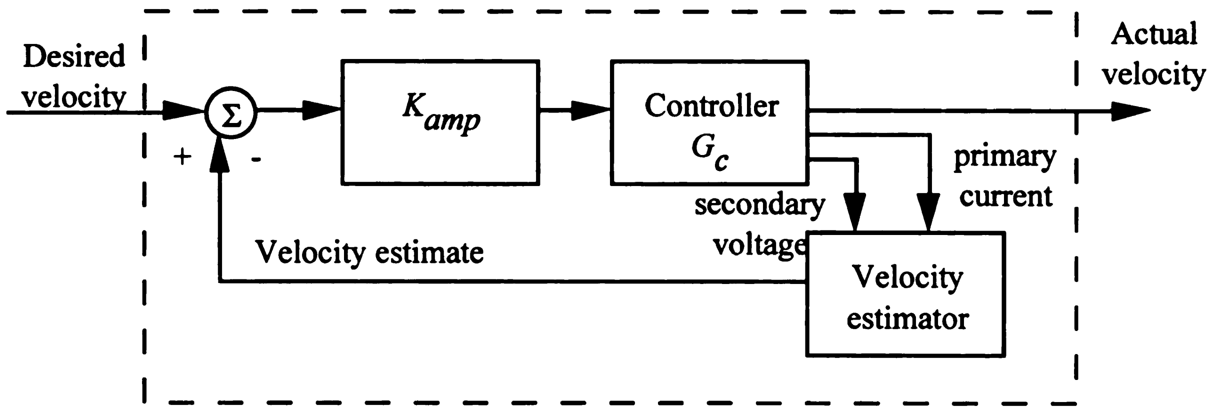

Figure 5.13. Block diagram of dual voice coil speaker compensation used in SHR actuator

PI Controller Design

The PI controller was implemented and the closed-loop SHR response was recorded with controller gains $K_P = K_I = 0$. In this configuration, the compensator attempts to hold the speaker face fixed in the presence of the disturbance. White noise was input as the disturbance to the system and the transfer function of P_2/D_I was measured using a Hewlett Packard dynamic signal analyzer model #35660A. With the SHR disconnected from a primary acoustic system, resonance was observed as a peak in the frequency response of the P_2/D_I transfer function. The results indicated that a resonant peak occurred at 120 Hz, however there was significant damping in the system, which reduced the peak amplitude. This damping was attributed to mechanical damping in the form of friction and electrical power dissipation in the current sensing resistor, R_m, in the speaker compensator. This damping is large compared to the acoustic damping expected in a passive Helmholtz resonator (Tang, and Sirignano, 1973). Other experiments indicated that damping was significantly reduced when current was not allowed to flow through the sensing resistor.

The closed-loop response was then measured with various non-zero controller gains. As predicted by the model, the analytical mapping between K_P and K_I and the resonant frequency and peak amplitude (2.11) – (2.13) did not produce the desired results. This was attributed to the deviation of the actuator from the ideal model. Even with the compensator, the effects of the speaker dynamics were not sufficiently minimized.

The empirical technique was used in place of the analytical mapping to tune the system in the presence of significant actuator dynamics. The PI controller design was based on qualitative information learned from the model. The objective was to find gains, K_P and K_I, that placed the resonance at various frequencies, while maintaining the same level of damping. The data was collected by fixing K_I, searching for a K_P that produced the desired peak amplitude, and recording the resonant frequency. The gains K_P and K_I are plotted against resonant frequency in Figure 2.14, which compares the experimentally derived controller gains with the model derived controller gains (Figure 5.9). Note that although there is a difference in the magnitude of the K_P gains, the overall trends of these graphs agree. The difference in the K_P value is attributed to the difficulty in estimating the damping parameters in the model. The K_P gain is negative for all values of ω_C with the most negative value at the nominal resonant frequency (130 Hz). Only a 10% change in K_P is required for the entire range of ω_C. The K_I gain ranges from –300 to 400 and passes through zero at the nominal resonant frequency. It should be noted that although there is good agreement between experimental and model results, the controller should not rely on the gains derived from the model, but should be determined experimentally.

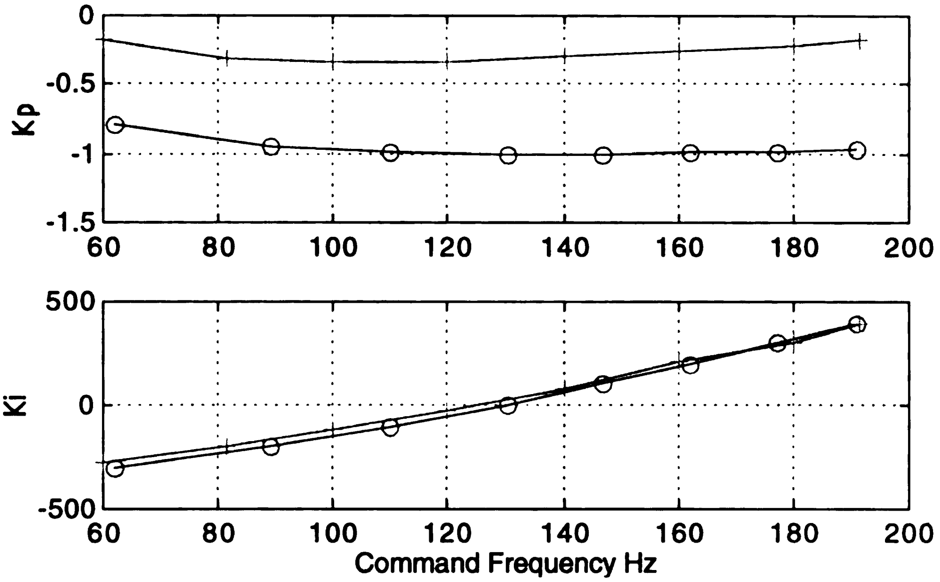

Figure 5.14. Graph of K_P and K_I vs. ω_c determined using an experimental empirical technique (+) and model-based empirical technique (o)

The tuning capabilities of the device are illustrated by the closed-loop frequency response measurements (Figure 2.15). The curves show the resonant peak for separate experiments with ω_c = 80, 110, 140, and 170 Hz and one curve for the controller gains set to zero. Note that the SHR with the gains set to zero is over-damped with approximately 45% damping. With nonzero controller gains, a resonance is exhibited and positioned at the desired frequency with approximately 5% damping for all cases. This result demonstrates the ability of the controller to tune the SHR to arbitrary frequencies.

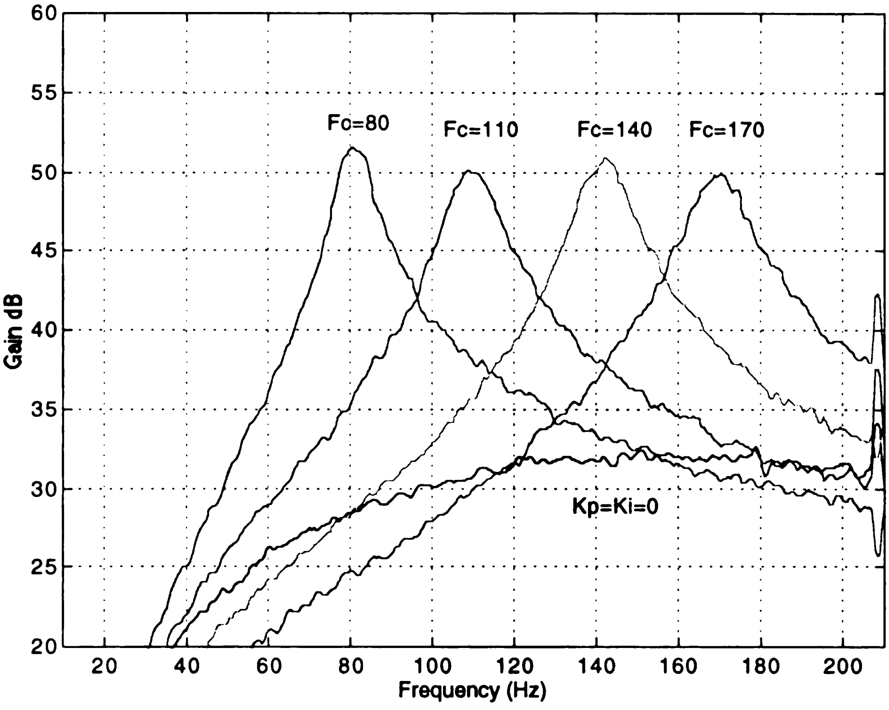

Figure 5.15. Experimental frequency response P_2/D_l for gain scheduling controller with ω_c = 80, 110, 140, and 170 Hz and with gains set to zero

Noise Reduction of a Time-varying Disturbance Tone in an Acoustic Duct

The final demonstration illustrates the SHR's ability to quiet noise in a primary acoustic system and to track a time-varying disturbance tone. Previous experiments examined the performance with no primary acoustic system to focus on the dynamics of the SHR alone. In this experiment, the SHR was connected to an acoustic duct and a pure tone noise was injected into one end and sound pressure levels were measured at the open end of the duct (Figure 5.16). The setup consisted of a 0.78 m long and 0.076 m diameter PVC pipe with the disturbance signal generated by a 6 inch audio speaker at x = 0 m, the SHR at x = 0.58 m, and a 1/2 inch B&K microphone type #4155 at x = 0.76 m to record P_3. The pure tone disturbance signal was generated by the DSP and the frequency, ω_c was known exactly by the controller.

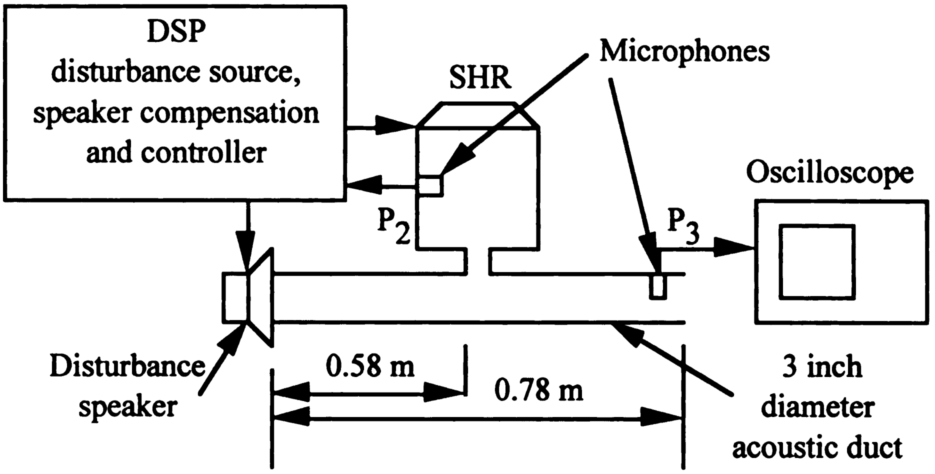

Figure 5.16. Schematic diagram of SHR connected to acoustic duct for noise quieting experiment, DSP generates disturbance tone and controls SHR, pressure is recorded in cavity and at duct opening on an oscilloscope

First, the system was tested to examine the effect of the closed-loop controller with a stationary disturbance tone. The noise reduction was measured by comparing P_3 with the controller (and compensator) deactivated, and activated. Other more common measures of noise reduction, such as insertion loss (ASTM Designation: C 634 – 96) compare the sound pressure level with the silencer inserted and removed from the system. This was not used here since the objective was to isolate the effect of the controller on the system. Figure 5.18 shows P_2 and P_3 with ω_C = 130 Hz as the controller is turned on at time t_0 = 0.05 sec. Before time t_0, the amplitude of P_3 is approximately 30 N/m^2 (124 dB), and the amplitude of P_2 is approximately 40 N/m^2 (126 dB). After t_0 there is a transient for approximately 0.02 sec, and the amplitude of P_3 reduces to 5 N/m^2 (107 dB) and P_2 increases to 200 N/m^2 (140 dB). The decrease in P_3 represents 17 dB of noise reduction in the unwanted sound transmitted from the duct to the room. The increase in P_2 represents the amplified resonance (reduction in damping) of the SHR. High frequency noise is also exhibited in the closed-loop P_3 signal due to noise introduced into the system by the local speaker compensation. This noise is unavoidable with the current speaker compensation algorithm and degrades the noise reduction results somewhat by generating relatively low level, approximately (85 dB overall SPL) broadband noise in closed-loop. This effect does not contribute to the overall SPL significantly since it is 22 dB below the 107 dB dominant noise signal. However, it is easily perceived by a human listener and produces the perception that the controller adds noise, reducing the overall effectiveness.

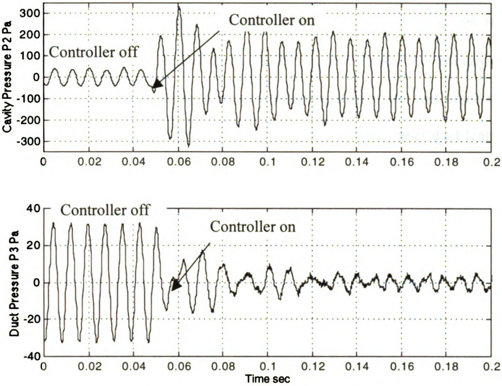

Figure 5.17. Pressure near duct opening, P_3 and pressure in SHR cavity, P_2 versus time with a 130 Hz disturbance noise as controller is activated, showing 17 dB reduction

Finally, the system was tested with a time-varying disturbance tone frequency to demonstrate the controller's tracking ability and the noise reduction at various frequencies. It was found that the range of tunable frequencies was sensitive to the K_{amp}, and that by reducing it from 30 to 28, a wider range could be achieved at the expense of reducing the magnitude of the noise reduction. The experiment was run twice: first in open-loop then again in closed-loop. In each trial P_3 versus time was recorded as ω_c was ramped from 80 to 180 Hz in 9 seconds. Figure 5.18 shows open- and closed-loop RMS P_3 versus time (top), ω_c versus time (middle), and noise reduction versus time (bottom), computed by subtracting closed-loop from open-loop RMS P_3. The open-loop SPL increases with ω_c due to the presence of an acoustic duct resonance at 190 Hz. This illustrates the difficulty in separating the SHR dynamics from the primary acoustic system dynamics and explains why the gain scheduling design was performed without a primary acoustic system. In other experiments not shown here, other duct lengths were used, and it was shown that there was little change in the system response. The noise reduction is defined by the difference between closed-loop and open-loop (bottom). The bottom graph shows that the noise reduction varies from 5 dB to as much as 15 dB. The effective range of frequencies for the device, defined as 6 dB or greater noise reduction, is 90 - 170 Hz. The low frequency (< 90 Hz) limitation is attributed to finite actuator travel. As the frequency is reduced, the controller requires larger displacements to generate a constant magnitude velocity. The speaker face can only generate displacements on the order of 1 cm. The high frequency (> 170 Hz) limitation is attributed to the control design. The algorithm found gains that produced peaks with equal magnitude in the frequency response of the P_2/D_l transfer function. The model reveals that this will produce peaks with magnitudes that decrease with frequency in the response of the Q_1/P_1 transfer function. This transfer function, not P_2/D_l interacts with the duct and creates the pressure release boundary condition. An attempt to compensate for this by changing the control strategy would require reducing the stability margin of the system. This experiment demonstrates that the SHR gain-scheduled adaptive control algorithm can track time-varying disturbance tone frequencies and provide significant noise reduction in acoustic systems over a range of frequencies.

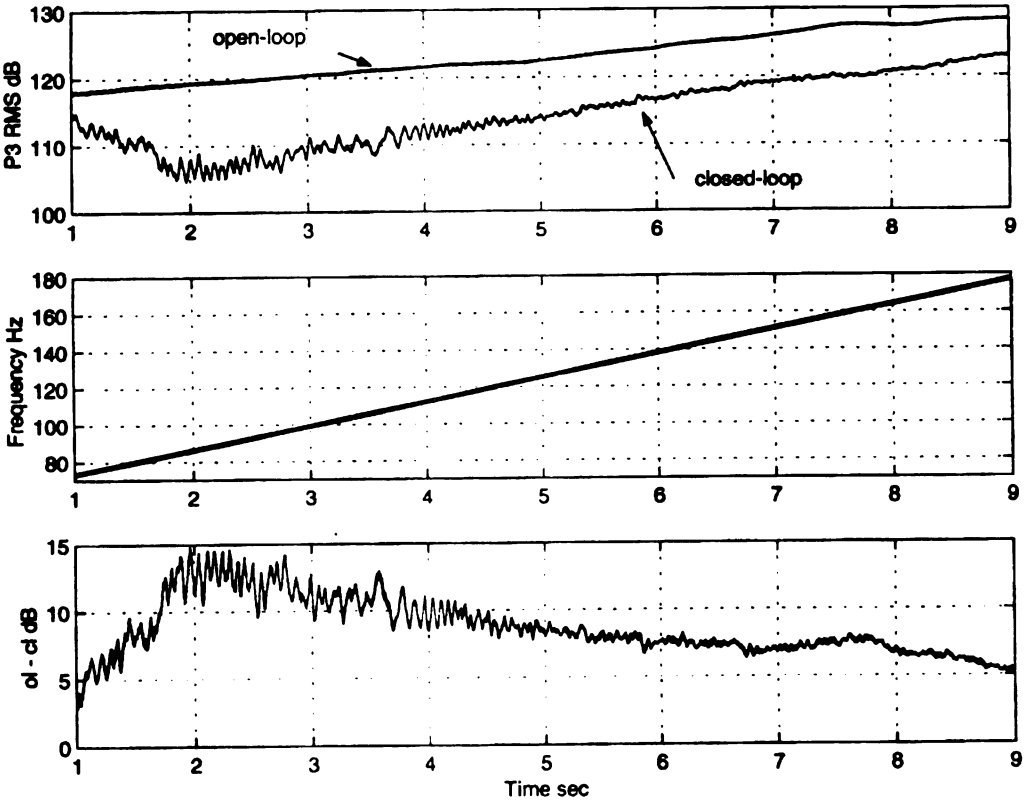

Figure 5.18. Time-varying disturbance results showing open and closed-loop RMS pressure P_3 near duct opening (top), disturbance tone, ω_c (middle), and noise reduction versus time computed from closed-loop subtracted from open-loop RMS P_3 (bottom) showing between 6 and 15 dB of noise reduction between 90 and 170 Hz

CONCLUSIONS

In this article, a model for the SHR was analyzed for closed-loop adaptive control. A stability analysis was presented and an analytical controller design was developed that produced a gain scheduling controller algorithm. This allows the system to track a disturbance tone with slow time-varying frequency while maintaining optimum amplitude and damping characteristics. It was shown that the analytical controller design was not effective in the presence of unmodeled actuator dynamics, and a model-based empirical controller design was presented which included actuator dynamics. The model was used to identify key factors in determining the gain scheduling algorithm, such as the effect of actuator dynamics, and sensitivity. Finally, experiments showed that the device was able to provide at 6 to 15 dB of noise reduction as the frequency of a disturbance tone varied with time from 90 to 170 Hz.

The control algorithm presented here has several beneficial features. It is composed of simple, inexpensive components that are commercially available. It requires a low order controller and can be implemented with a PI controller with variable gains. The tuning algorithm can run at a relatively slow speed and does not require a high speed digital signal processor. No sensor is required outside of the SHR cavity. This means that the only connection to the primary acoustic system is the resonator neck and the design is independent of the primary system. Finally, the sensitive components in the controller are all located in the resonator cavity out of the direct path of the acoustic duct. This reduces the likelihood of damage from debris and harsh environmental conditions. The controllable SHR is a powerful and adaptive tool in reducing unwanted noise in acoustic systems.

Chapter 6

Conclusions

This dissertation presents the invention of an electronically tuned semi-active Helmholtz resonator. This device can be attached to a primary acoustic system, such as a duct, to reduce the transmission of narrow frequency band noise. It can be adaptively tuned on-line to track a disturbance signal with slow time-varying frequency. It has several advantages over similar inventions. There are no complex moving parts or mechanisms so it is cheaper and easier to implement. The sensitive components are removed from the primary acoustic system and placed in the resonator cavity, so they are less susceptible to damage from harsh environments. The device is fault tolerant: in the event that the controller is turned off, it continues to provide nominal acoustic filtering. Also, it requires only one connection to the primary acoustic system. No sensors are required external to the device, so that its operation is not dependent on the structure of the primary acoustic system. The control algorithm is relatively simple and easy to implement. This work focused on four major topics related to the device: the overall invention and development of the SHR, an analysis of the power flow in the device, a study of implementation issues, and finally, the development of an adaptive control algorithm.

An analytical model was first developed which included the resonator, controller and an ideal actuator. It was shown that the acoustic impedance of the SHR could be modified by controlling the acoustic impedance on the actuator face. An analytical relationship between the actuator impedance and the SHR impedance was presented and used to derive an analytical controller design. This design produced controller gains for a simple proportional integral controller from the desired resonant frequency and peak amplitude. Numerical simulation was used to show that this controller successfully re-tuned the SHR. Next, the ideal actuator model was replaced with a compensated speaker model and it was revealed that the control design was no longer effective in the presence of unmodeled actuator dynamics. A model-based empirical control design was presented that included the effects of actuator dynamics but required a trial-and-error search technique. Experimental results were presented that demonstrated the control design and the effectiveness of the SHR in quieting noise in a duct. Future topics that relate to the overall design of the SHR include investigating other resonator configurations and generalizing the technique to other vibration reduction problems. The overall concept of this invention does not rely on the use of a Helmholtz resonator. Other classes of acoustic resonators are available and may have advantages in different applications, such as higher frequency noise control, where the use of Helmholtz resonators is limited. The concept may also be applied to mechanical vibration problems.

The second major topic in this work concerned the power flow in the SHR and an acoustic duct. This topic answered the question, "Where does the sound go?" It was shown that the SHR creates a region in the duct that reflects the incident sound back to the source, thus reducing the transmitted sound. Expressions were developed for the incident, reflected and transmitted acoustic power, reflection coefficient, and transmission loss as a function of the acoustic parameters and control gains. It was concluded that the device is most effective when there is no dissipation in the resonator. This highlights the point that the commonly used term, "sound absorber" is a misnomer in this case since there is little absorption. Instead, the mode of operation is sound reflection. The model and experimental results demonstrated that the closed-loop control of the SHR moved the center frequency of the reflection coefficient to desired values.

The third topic in this work concerned implementation issues regarding the choice of actuator. A local feedback compensator was added to a speaker which was used to implement the control input to the SHR. It was discovered that the compensator improved the low frequency response of the speaker moderately but degraded the high frequency response. It also added broadband noise to the system. The closed-loop SHR controller together with the compensated speaker provided as much as 32 dB of noise reduction in a narrow frequency band, yet the overall sound pressure level reduction was only 18 dB due added broadband noise. The speaker was then applied to the SHR without the compensation and it was discovered that the control authority was reduced but no random noise was introduced into the system. The narrow band noise was reduced by 9 dB and the overall sound pressure level was reduced by 9 dB since no noise was added by the controller. This led to the conclusion that the compensated speaker is more desirable when the objective is to reduce narrow band sound and overall sound pressure level, while the uncompensated speaker is more desirable when the objective is to improve the sound quality. Future work in the implementation of the SHR includes improving the actuator. A common problem in active acoustic noise control is lack of effective actuators. While this problem has received much attention, it is clear from this work that more work must be done in this area.

The fourth topic in this work concerned a closed-loop adaptive control strategy for the SHR. A gain-scheduled controller was developed from the empirical control design. Numerical simulations and experimental results showed that the device was able to track a disturbance noise with slow time-varying frequency. Between 10 and 15 dB of noise reduction was demonstrated with a disturbance frequency that varied from 100 to 150 Hz. Future work in this topic includes optimal, adaptive control design. The gain scheduling controller is the least complex of the adaptive control algorithms. An algorithm could be developed to start from the controller gains prescribed by this work and search for more optimal gains while minimizing an error function.

In conclusion, the SHR developed in this work has many beneficial features that make it a useful tool to quiet noise in enclosed acoustic systems. It is an improvement over passive resonators because it can track a disturbance noise when the frequency changes from the nominal tuned frequency. It is also a relatively simple device that requires only one connection to the primary acoustic system. Furthermore, it can be implemented with a low order controller and the design is independent of the primary acoustic system.

References

ASTM Designation: C 634 - 96, "Standard Terminology Relating to Environmental Acoustics"

ASTM Designation: E 1050-90, "Standard Test Method for Impedance and Absorption of Acoustical Materials Using a Tube, Two Microphones, and a Digital Frequency Analysis System"

ASTM Designation: E 477-96, "Standard Test Method for Measuring Acoustical and Airflow Performance of Duct Liner Materials and Prefabricated Silencers"

ASTM E 1265-90, "Standard Test Method for Measuring Insertion Loss of Pneumatic Exhaust Silencers," ASTM E 1265-90, 1995.

Bedout, Francheck, et. Al. 1997, "Adaptive-Passive Noise Control with Self-Tuning Helmholtz Resonators," Journal of Sound and Vibration, v 202, p109-123.

Beranek L. L., Ver I. L., 1992, "Noise and Vibration Control Engineering," John Wiley & Sons, New York.

Birdsong, C. B., and Radcliffe, C. J., 1999, "A Compensated Acoustic Actuator for Systems with Strong Dynamic Pressure Coupling," Journal of Vibrations and Acoustics, Vol. 121, pp. 89-94.

Birdsong, C., 1996, "A Compensated Actuator for an Acoustic Duct," Masters Thesis, Michigan State University.

Blaser, D., and Chung, J., 1978, "A Transfer Function Technique for Determining the Acoustic Characteristics of Duct Systems with Flow," Inter-Noise, San Francisco, May.

Chung, J., and Blaser D., 1980, "A Transfer function method of measuring in-duct acoustic properties. I. Theory," J. Acoust. Soc. Am. 68(3), Sept.

Furstoss, M., Thenail, D., and Galland, M. A., 1996, "Surface Impedance Control for Sound Absorption: Direct and Hybrid Passive/Active Strategies," Journal Sound and Vibrations, vol. 203, p 219-236.

Garrett, K., 1992 , "Inter-cylinder charge Robbing: Key factor in Induction-Tract Tuning." Automotive Engineer v 17 n 4 Aug-Sept.

Graham, C. R., and Graves, M. C., et. al., 1992, "General Motors High Performance 4.3L V6 Engine," SAE Transaction, vol. 101, Sect 3, p 1305-1320.

Hartmann, W., 1997, "Signals, Sound, and Sensation," American Institute of Physics, Woodbury, New York.

Harwood, H.D., 1974, "Motional Feedback in Loudspeakers," Wireless World, 80, pp. 51-52.

Heidelberg, L. J., and Gordon, E. B., 1989, "Acoustic Evaluation of the Helmholtz Resonator Treatment in the NASA Lewis 8- by 6-Foot Supersonic Wind Tunnel," NASA technical memorandum ; 101407.

Holdaway, H.W., 1963, "Design of Velocity Feedback Transducer Systems for Stable Low-Frequency Behavior," IEEE Transactions, **AU-11**, pp. 155-173.

Hsomi, M., Goawao, S., Imagawa, T., and Hokazono, Y., 1993, "Development of exhaust manifold muffler," SAE Special Publications New Engine Design and Engine Component Technology International Congress and Exposition Mar 1-5 n 972 Detroit

Hull, A., and Radcliffe, C., 1991, "An Eigenvalue Acoustic Measurement Technique," Journal of Vibrations and Acoustics, April 1991, Vol. 113, pp. 250-254

IEEE 1975, "IEEE Recommended Practice for Loudspeaker Measurements," IEEE std. 219-1975.

Jameson, R. T., and Hodgins, P. A., 1990, "Improvement of the Torque Characteristics of a Small, High-Speed Engine Through the Design of Helmholtz-Tuned Manifolding," SAE International Congress and Exposition Detroit, Michigan, February.

Khalil, H. K., 1996, "Nonlinear Systems," Prentice-Hall, Inc., New Jersey

Klaassen, J.A., de Koning, S.H., 1968, "Motional Feedback with Loudspeakers," Philips Technical Review, **29**, No. 5, pp. 148-157.

Kong, H. , and Woods, R., 1992, "Tuning of Intake Manifold of an Internal Combustion Engine Using Fluid Transmission Line Dynamics," International Congress & Exposition, SAE, February.

Kraft, R., Janardan, B., Kontos, G., and Gliebe, P., 1994, "Active Control of Fan Noise-Feasibility Study," NASA Contractor Report 195392

Levine, H. and Schewinger, J., 1946, "On the Radiation of Sound from an Unflanged Circular Pipe," Physical Review, Vol. 73, No. 4, pp. 383-406, February 15.

Morel, T., Morel, J., and Blaser D., 1991, "Fluid Dynamic and Acoustic Modeling of Concentric-Tube Resonators/Silencers," SAE Transactions Journal of Engines Section 3

Phillips, C., and Harbor, R., "Feedback Control Systems," Prentice-Hall, New Jersey.

Pierce, Allan D., 1981, "Acoustics : an introduction to its physical principles and applications," New York : McGraw-Hill Book Co.

Radcliffe C. J., and Gogate, S. D., 1996, “Velocity Feedback Compensation of Electromechanical Speakers for Acoustic Applications,” International Federation of Automatic Control, Triennial World Congress, July.

Radcliffe C.J., and Gogate S.D., Hall G., 1994, “Development of an Active Acoustic Sink (AAS) for Noise Control Applications,” Active Control of Vibrations and Noise, ASME.

Radcliffe, C. J., and Gogate, S. D., 1992, “Identification and Modeling Speaker Dynamics for Acoustic Control Applications,” ASME Symposium on Active Control of Noise and Vibration.

SAE Handbook, 1995, "Measurement of Light vehicle exhaust sound level under stationary conditions," SAE J1169 Mar92

Selamet, A., Dickey, N., and Novak,J., 1995, "Theoretical, computational and experimental investigation of Helmholtz resonators with fixed volume: lumped versus distributed analysis," Journal of Sound and Vibration, Vol. 187(2), 358-367.

Seto, W., 1971, "Theory and Problems of Acoustics, McGraw-Hill Book Company, New York.

Speakerman, C., and Radcliffe, C., 1988, "Decomposing One-dimensional Acoustic Response into Propagating and Standing Wave Components," Journal of the Acoustical society of America, Vol. 84, No. 4, pp. 1542-1548

Tang, P. K., and Sirignano, W. A., 1973, “Theory of a Generalized Helmholtz Resonator,” Journal of Sound and Vibration, vol. 26 (2), pp. 247-262.

Tanner, R.L., 1951, "Improving Loudspeaker Response with Motional Feedback," Electronics, **24**, No. 3.

Temkin, 1981, “Elements of Acoustics,” John Wiley & Sons, Inc.